Electron transport and phonons in atomic wires and single molecule junctions

CARLOS ARROYO RODRÍGUEZ

Electron transport and phonons in atomic wires and single molecule junctions

Memoria presentada por:
CARLOS ARROYO RODRÍGUEZ
para optar al grado de Doctor en Ciencias Físicas por el Departamento de Física de la Materia Condensada de la Universidad Autónoma de Madrid

Tesis dirigida por:
PROF. MARISELA VÉLEZ TIRADO
PROF. NICOLÁS AGRAÏT DE LA PUENTE

FACULTAD DE CIENCIAS
UNIVERSIDAD AUTÓNOMA DE MADRID

Thesis committee:

Prof. Sebastián Vieira Díaz (Universidad Autónoma de Madrid)
Prof. Jan M. van Ruitenbeek (Leiden University)
Prof. Nazario Martín León (Universidad Complutense de Madrid)
Prof. Juan Carlos Cuevas Rodríguez (Universidad Autónoma de Madrid)
Assit. Prof. Michel Calme (University of Basel)

This work has been supported by the Spanish MICINN through the Grants No. MAT2008-01735, No. MAT2004-03069 and Consolider-Ingenio 2010 under Grant No. CSD2007-0010 and by CAM through "CITECNOMIK" Grant No. P-ESP-000337-0505.

Contents

Preface

Since the dawn of human kind, we have always been fascinated by the uncontrolled forces of nature, such as lightning and thunder in an electrical storm. The earliest mention of electric phenomena is found in the ancient Egyptian text, written roughly 4750 years ago. It is well know that the ancient Greeks were aware of electrostatic phenomena produced by amber, but they regarded it as a mere curiosity or toy without possessing any theoretical explanation. Several discoveries in the 18th and 19th centuries led to a notable advance in our understanding of the electromagnetic phenomena. The technological revolution of the late 20th century has changed most aspects of our lives, industry and society.

It can be considered that modern electronics development begun in 1947, when Bardeen, Brattain and Shockley invented the transistor. The transistor, a semiconductor device for amplifying an electronic signal, began a revolution within the electronic components industry. Their tiny size, reliability, and durability enabled manufactures to shrink the size of electronics. The semiconductor-based electronics has seen a remarkable miniaturization trend, driven by many scientific and technological innovations. The miniaturization of electronic devices has inherent advantages such as higher speed, lower cost and greater density. But if this trend is to continue, the size of microelectronic circuit components will soon need to reach the scale of atoms or molecules.

Molecular scale electronics is a branch of nanotechnology dealing with the study and application of individual molecules as building blocks for the fabrication of electronic components. The idea of using molecules as electronics components was proposed in the seminal paper of Aviram and Ratner in 1974. This concept presents a possibility for dramatic size reduction, since individual molecules are hundreds of times smaller than the smallest features conceivably attainable by semiconductor technology. Moreover, because single molecules constitute the smallest stable structures imaginable, this miniaturization is the ultimate goal for shrinking electrical circuits.

One of the main aims of molecular electronics is to fundamentally understand and exploit the electronic properties of individual molecules wired between conducting electrodes. A primary challenge towards the realization of such structures is to develop reliable methods to connect two electrodes to a single molecule. Metal-molecule-metal junctions are of interest both for improving our fundamental understanding of electrical transport at the nanoscale and for the development of novel electronic devices.

The invention of the scanning tunneling microscopy (STM) by Binnig and Rohrer in 1982 has led to a revolution in the investigation and manipulation of matter on the atomic scale. A full description of the transport properties of atomic-sized conductors requires a quantum mechanical treatment of both atomic structure and electron transport. Two closely related techniques, STM break junction (STM-BJ) and mechanically controllable break junction (MCBJ) have progressed over the past decade towards measuring the electrical properties of atomic-sized contacts and single molecule junctions. To make reliably metal-molecule-metal junctions, a widely used strategy is to attach the molecule with two appropriate terminal groups, such as thiols (-SH), which bind strongly the molecule between metal electrodes.

The main goal of this thesis has been to investigate the electron transport in atomic gold wires and single molecule junctions. These junctions, formed by means of the STM-BJ technique, are very attractive because being so simple in structure are amenable for performing detailed theoretical calculations. Starting from the study of atomic gold wires (Chap. 3), we have focused on fundamental aspects regarding the formation of molecular junctions under different experimental conditions such us, at ambient conditions in solution (Chap. 4) or at low temperatures in cryogenic vaccum (Chap. 5).

At low temperatures, most of the vibrational modes of a given atomic-sized contact are frozen. The cryogenic environment makes it possible to excite and detect specific vibrational modes in the narrowest part of the junction. Due to the short length of these structures, most of the electrons cross the junction without any energy loss. However, a small fraction of electrons are able to exchange energy with vibrational modes. These inelastic processes are experimentally accesible by means of the inelastic electron tunneling spectroscopy (IETS). The results obtained from IETS measurements give us valuable information to characterize the atomic structure and electrical properties of atomic gold wires and single molecule junctions.

Prefacio

Desde los albores de la humanidad, siempre hemos estado fascinados por las incontroladas fuerzas de la naturaleza, como los relámpagos y los truenos en una tormenta eléctrica. La primera mención sobre los fenómenos eléctricos se encuentra en los antiguos textos egipcios, escritos aproximadamente hace 4750 años. Es bien sabido que los antiguos griegos eran conscientes de los fenómenos electrostáticos producidos por el ambar, pero ellos lo consideraban como una mera curiosidad o juguete sin ninguna explicación teórica. Varios descubrimientos los siglos 18 y 19 condujeron a un notable avance en nuestro conocimiento sobre los fenómenos electromagnéticos. La revolución tenológica a finales del siglo 20 ha cambiado muchos aspectos de nuestras vidas, industria y sociedad.

Se considera que el desarrollo de la electrónica moderna comenzó en 1947, cuando Bardeen, Brattain y Shockley inventaron el transistor. El transistor, un dispositivo semicondutor para amplificar una señal eléctrica, inició una revolución en la industria de componentes electrónicos. Su pequeño tamaño, fiabilidad y durabilidad permite la reducción de tamaño en la fabricación electrónica. La industria basada en semiconductores ha visto una remarcable tendencia hacia la miniaturizacion, impulsada por muchas inovaciones científicas y tecnológicas. La miniaturización de dispositivos electrónicos tiene inherentes ventajas como mayor velocidad, menor coste y mayor densidad. Pero si ésta tendencia continúa, el tamaño de los componentes en circuitos microelectrónicos alcanzará el tamaño de átomos o moléculas.

La electrónica a escala molecular es una rama en nanotecnología dedicada al estudio y aplicación de moléculas individuales como bloques de construcción para la fabricación de componentes electrónicos. La idea de utilizar moléculas como componentes electrónicos fue propuesta en un artículo seminal de Aviram y Ratner en 1974. Este concepto presenta la posibilidad de una dramática reducción en tamaño, ya que el tamaño de una molécula es cientos de veces más pequeño que la menor estructura concebible con la tecnología semiconductora. Además, dado que las moléculas constituyen las estructuras estables más pequeñas imaginables, esta miniaturización constituye el objetivo final en la reducción de circuitos eléctricos.

Uno de los objetivos en electrónica molecular es entender fundamentalmente y explotar las propiedades eléctricas de moleculas individuales conectadas entre electrodos conductores. El primer reto hacia la realización de tales estructuras es desarrollar métodos fiables para conectar dos electrodos a una sola molécula. Los contactos metal-molécula-metal son de interés para mejorar nuestro

conocimiento del tranporte eléctrico en la nano escala y para el desarrollo de nuevos dispositivos electrónicos.

La invención del microscópio de efecto túnel (STM) por Binnig y Rohrer en 1982 ha dado lugar a una revolución en la investigación y manipulación de la materia a escala atómica. Una descripción completa de las propiedades de transporte en conductores de tamaño atómico requiere un tratamiento mecanocuántico de la estructura átomica y del transporte electrónico. Dos técnicas estrechamente relacionadas, STM uniones de rotura (STM-BJ) y las uniones de rotura mecánicamente controlada (MCBJ) han progresado en la pasada decada hacia la medición de las propiedades eléctricas de contactos de tamaño atómico y los contactos de una sola molécula. Para realizar contactos metal-molécula-metal, una estrategia ampliamente utilizada es sujetar la molécula con dos apropiados grupos terminales, como los tioles (-SH), que unen fuertemente la molécula entre electrodos de metal.

El objetivo principal de ésta tesis ha sido investigar el transporte de electrones en cadenas atómicas de oro y contactos de una sola molécula. Estos contactos, formados por medio de la técnica STM-BJ, son muy atractivos porque al ser tan sencillos en estructura posibilitan la realización de detallados cáculos teóricos. Comenzando por el estudio de cadenas atómicas de oro (Cap. 3), nos hemos centrado en aspectos fundamentales relacionados con la formación de contactos moleculares en distintas condiciones experimetales, a condiciones ambiente en disolución (Cap. 4) o a bajas temperas en vacío criogénico (Cap. 5).

A bajas temperaturas, la mayoría de los modos vibracionales en un contacto de tamaño atómico están congelados. El entorno criogénico hace posible excitar y detectar modos vibracionales específicos en la parte más estrecha del contacto. Debido a la pequeña longitud de estas estructuras, la mayoría de los electrones atraviesan el contacto sin perder energía. Sin embargo, una pequeña fracción de electrones son capaces de intercambiar energía con modos vibracionales. Estos fenómenos inelásticos son accesibles experimentalmente mediante la espectroscopía túnel de electrones inelásticos (IETS). Los resultados obtenidos en las medidas de IETS nos dan una valiosa información para caracterizar la estructura atómica y las propiedades eléctricas de cadenas atómicas de oro y contactos de una sola molécula.

I

Theory of quantum electron transport

The electronic properties of conducting materials change drastically when their dimensions are reduced down to the atomic scale. By using relatively simple techniques (described in detail in Chap. 2), it is possible to investigate the transport properties of atomic-sized contacts. At this scale, semiclassical descriptions cease to be valid and a quantum mechanical treatment becomes necessary.

In this chapter, we introduce the main concepts and models utilized to describe the electron transport in atomic-sized contacts, including the case of atomic wires and molecular junctions. The interested reader can find much more information in the specialized books and reviews [1-4].

1.1 Length scales for the conductance

Classically, the conductance of a macroscopic solid, $G=I/V$, which is the inverse of its resistance, is determined by the Ohm's law. In the case of a cylindrical sample of cross section A and length d, the conductance has the simple expression

$$G = \sigma \frac{A}{d} \tag{1}$$

where σ, the conductivity, is a material-dependent parameter that contains all the microscopic information. However, for samples of atomic dimensions the Ohm's law ceases to be valid. As the sample is reduced in size from macroscopic to atomic dimensions, the electronic transport mechanisms go through different conductance regimes. One can consider three length scales that characterize the different regimes of the conductance [2]. These lengths vary widely from one material to another and are also strongly affected by temperature, magnetic field, etc.

The phase relaxation length, L_φ, is the distance over which the quantum coherence is preserved. If the scale of the sample L, is such that $L< L_\varphi$, the sample is in the so-called mesoscopic regime. The phase coherence gives rise to phenomena in which it is manifested the wavelike nature of electrons. For metallic thin films at liquid-helium temperatures, L_φ is of the order of few micrometers. The theory of electron transport in the mesoscopic regime, was developed by Landauer [5] and extended by Büttiker [6].

Another important length scale is the mean free path, l. This length denotes the average distance between two successive collisions of electrons, without changes in the phase of the wavefunction. The value of l is used to distinguish between the diffusive regime, for $L>>l$, and the ballistic regime when $L<l$. The ballistic electrons pass through the sample as cannon balls without having any scattering event. In polycrystalline metal films at room temperature, l is in the range from 10 to 100 nm. By using a semiclassical approximation Sharvin [7] found an expression for the conductance in ballistic regime

$$G = \frac{3\pi\sigma a^2}{4l} = \frac{2e^2}{h}\left(\frac{k_F a}{2}\right)^2 \qquad (2)$$

where a is the contact radius, l is the mean free path, h is the Plack's constant and k_F is the Fermi wave vector.

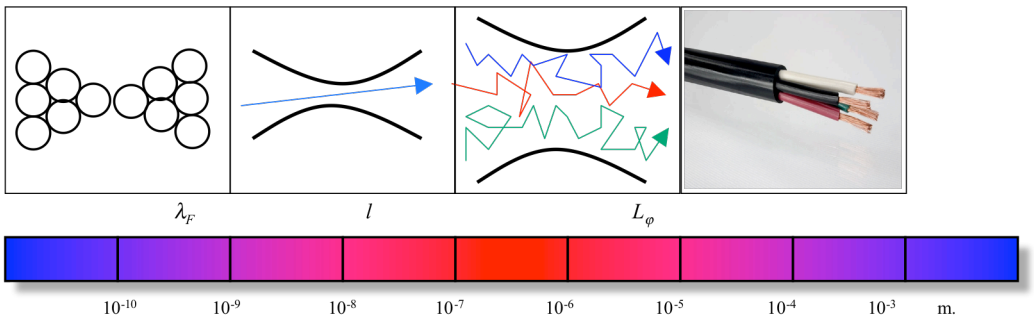

Figure 1.1: Scheme of different transport regimes found by reducing the size of a metallic contact at low temperatures. From right to left: Ohmic, diffusive, ballistic and atomic transport.

Atomic-sized conductors are even smaller systems. The Fermi wavelength, λ_F, related with the velocity of electrons at the Fermi level(1) is the third length scale. For $L<\lambda_F$, the sample is in the full quantum regime which cannot be described by semiclassical arguments. In this regime, the atomic arrangements and the quantum nature of atoms play a fundamental role in the conductance. For metals, λ_F is typically of the order of few angstroms. In order to understand the complex phenomena observed at this regime, first-principles calculations are neccesary to mimic the experimental situation as closely as possible.

(1) The Fermi level is the highest energy state occupied in a system of electrons at absolute zero temperature.

1.2 Free electron model

As a first simplified model of a contact or constriction, we may consider a thin wire of rectangular cross-section, with free and independent electrons connected to two macroscopic electrodes. By solving Schrödinger's equation(2),

$$-\frac{\hbar^2}{2m^*}\nabla^2\psi(x,y,z) = E\psi(x,y,z) \tag{3}$$

with periodic boundary conditions in z, $x\in[0,L_x]$ and $y\in[0,L_y]$. We easily obtain the eigenstates ψ_{nmk} and eigenvalues $E_{nm}(k)$,

$$\psi_{nmk}(x,y,z) = \frac{2}{\sqrt{L_x L_y L_z}}\sin\left(\frac{n\pi}{L_x}x\right)\sin\left(\frac{m\pi}{L_y}y\right)e^{ikz} \tag{4}$$

$$E_{nm}(k) = \frac{\hbar^2}{2m^*}\left(k^2 + \left(\frac{n\pi}{L_x}\right)^2 + \left(\frac{m\pi}{L_y}\right)^2\right) = \frac{\hbar^2 k^2}{2m^*} + E^c_{nm} \tag{5}$$

where n=1,2,3,… and m=1,2,3,…

From (5), we observe that the electron states are split into a set of parabolic one-dimensional subbands. The bottom of each subband is located at an energy E^c_{nm}.

Each eigenstate can carry in the z direction an amount of current I_{nmk} given by, the integral over the cross-section of the wire, of the probability current density, times the electron charge

$$I_{nmk} = e\frac{i\hbar}{2m^*}\int_0^{L_y}\int_0^{L_x}\left(\psi_{nmk}\frac{\partial\psi^*_{nmk}}{\partial z} - \psi^*_{nmk}\frac{\partial\psi_{nmk}}{\partial z}\right)dx\,dy = \frac{e}{L_z}\frac{\hbar k}{m^*} \tag{6}$$

In the equilibrium, i.e., when the chemical potentials of the electrodes are equal, for each right-moving state $+k$ there is a degenerate left-moving state $-k$, that carries the same current in the opposite direction. The occupation of $+k$ states is fixed by the Fermi-Dirac distribution function on the left electrode, whereas the occupation of $-k$ states is fixed by the Fermi-Dirac distribution function on the right electrode [2], being respectively

$$f_{L,R}(E) = \frac{1}{1+\exp(E-\mu_{L,R}/k_BT)} \tag{7}$$

To have a net current flowing through the wire there must be an imbalance between the population of $+k$ and $-k$ states. Such an imbalance is provided by

(2) The effective mass, m^*, is the equivalent mass of an electron moving in a periodic potential. Effective masses can be derived from band structure computations.

the voltage bias V applied between the electrodes. The difference between the chemical potentials of the electrodes is proportional to the bias voltage $eV=\mu_L-\mu_R$. Therefore, each subband contributes to the current with

$$I_{nm} = 2\sum_k I_{nmk}\left(f_L(E) - f_R(E)\right) = 2e\sum_k \frac{\hbar k}{m^* L_z}\left(f_L(E) - f_R(E)\right) \tag{8}$$

where the factor 2 is included to consider spin degeneracy 2 of each eigenstate.

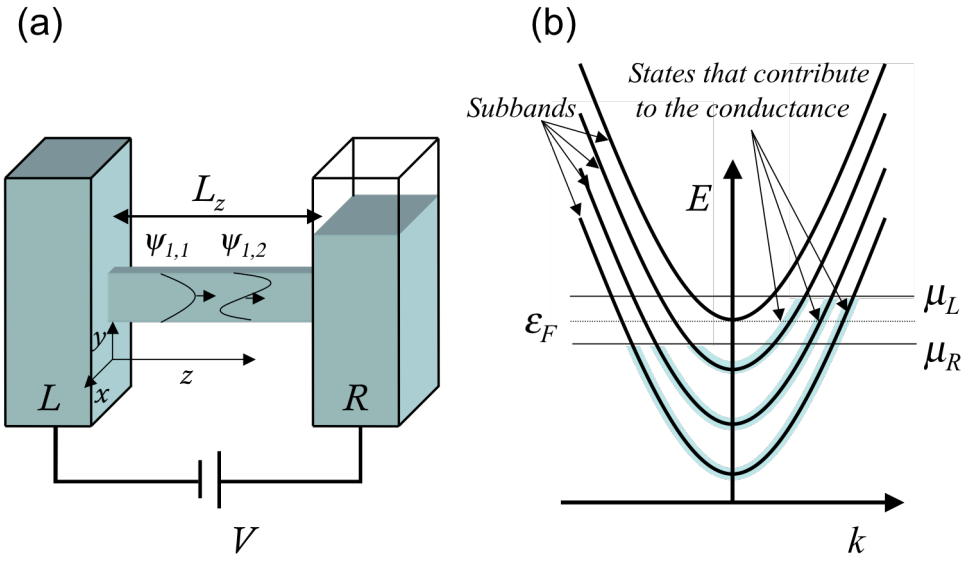

Figure 1.2: (a) *Narrow conductor connected between two macroscopic electrodes L and R. The electrodes are connected to a voltage difference,* $V=\mu_L-\mu_R/e$, *which produce an imbalance in the occupation of electronic states in the constriction.* (b) *Occupation of electronic states on the subbands.*

The sum in (8) can be rewritten as an integral,

$$\sum_k \rightarrow \frac{L_z}{2\pi}\int_{-\infty}^{+\infty} dk \tag{9}$$

by using a change of variables given by $dE = \frac{\hbar^2 k}{m^*}dk$, (8) simplifies to

$$I_{sub} = \frac{2e}{h}\int_0^{+\infty} dE(f_L(E) - f_R(E)) \tag{10}$$

Free electron model

At zero temperature, $f_L(E)$ and $f_R(E)$ are step functions, equal to 1 below their respective chemical potentials $\mu_L=\varepsilon_F+eV/2$ and $\mu_R=\varepsilon_F-eV/2$, and 0 above. Thus, the current carried by each subband is given by

$$I_{sub} = \frac{2e}{h}(\mu_L - \mu_R) = \frac{2e^2}{h}V = G_0 V \tag{11}$$

When the scattering from the connections to the electrodes is negligible, as in the case of adiabatic constrictions, the conductance of the wire is simply given by the number of subbands below the Fermi level, with each subband cotributing in $G_0=2e^2/h=(12.9\ \mathrm{K\Omega})^{-1}$ to the conductance. Equivalently, the conductance of the wire is quantized in units of G_0, called the conductance quantum. The total number of occupied subbands or propagating modes N_c can be calculated for different constriction geometries [8], for a wire of rectangular cross-section N_c is given approximately(3) by

$$N_c \approx \frac{\pi k_F^2}{4}\left(\frac{L_x L_y}{\pi^2}\right) = \pi\frac{A}{\lambda_F^2} \tag{12}$$

where $A=L_xL_y$ is the wire cross-section.

We have shown that the conductance of a perfect wire can be described by the so-called Sharvin conductance (2)

$$G \approx \frac{2e^2}{h}\pi\frac{A}{\lambda_F^2} \tag{13}$$

Note that in contrast to the classical description (1), the conductance is totally independent of the length of the wire, and depends on the material through λ_F.

A quantum point contact (QPC) is a narrow constriction in a 2-dimensional electron gas (2DEG) formed at the interface of a GaAs-AlGaAs heterostructure. The length of the QPC is much less than the mean free path and the width can be tuned to become comparable to the Fermi wavelength by the gate voltage. Under these conditions it is possible to investigate in detail the ballistic transport of electrons. Experimentally, as the width of the QPC is increased continuously, the conductance increases by steps of G_0. This phenomenon of conductance quantization was observed for the first time by two different groups [9, 10] in 1988.

(3) The number of modes below the Fermi level is given by the so-called Weyl expansion $N=A\pi/\lambda_F^2-(L_x+L_y)/\lambda_F+1/4$

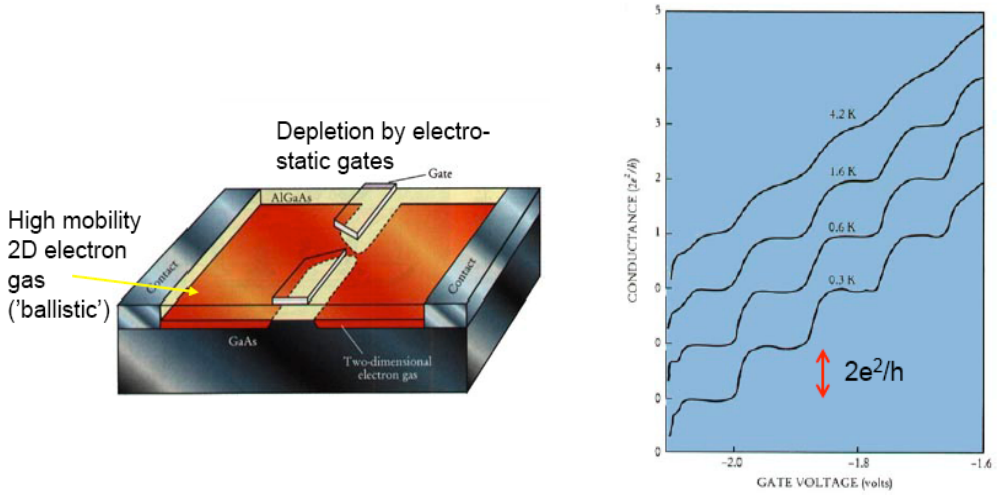

Figure 1.3: Schematic cross-sectional view of a 2DEG taken from [9]. Conductance quantization as a function of the gate voltage which define the constriction of the 2DEG.

1.3 Landauer-Büttiker formalism

The scattering approach, also called Landauer-Büttiker formalism, provides a simple way to calculate the conductance of systems in the mesoscopic regime. In this framework, the conductance through a sample is treated as a scattering problem. All the scattering processes are supposed to occur in a region **S**. The scattering region, **S**, is connected by perfect conductors to macroscopic electrodes. The temperature and chemical potential of the electrodes are well defined and in practice, electrodes act as ideal electron reservoirs. Due to the lateral confinement, as we have discussed in the previous section, the perfect conductors carry a limited number of states or modes, which usually are denoted by N_L and N_R.

Landauer-Büttiker formalism

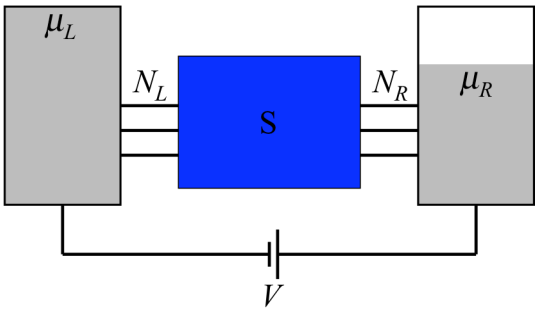

Figure 1.4: Conductor model in the Landauer-Büttiker formalism. The region where the scattering processes occur (blue area) is connected by perfect conductors to macroscopic electrodes. A difference of voltage $V=(\mu_L-\mu_R)/e$ is applied between the electrodes.

The basic idea is to relate the conductance with the transmission and reflection probability for electrons incident on the sample. An incoming right-moving state

$$|m\rangle e^{ikz} \tag{14}$$

can transmit to an outgoing right-moving state,

$$|l\rangle e^{ikz} \tag{15}$$

with transmission probability t_{ml}, and reflect to an outgoing left-moving state

$$|n\rangle e^{-ikz} \tag{16}$$

with reflection probability r_{mn}.

For a two-terminal configuration as showed in Fig. 1.4, the outgoing states from the left O_L and right O_R, are related to the incoming states from the left I_L and right I_R by the scattering matrix

$$\begin{pmatrix} O_L \\ O_R \end{pmatrix} = \begin{pmatrix} \hat{r} & \hat{t}' \\ \hat{t} & \hat{r}' \end{pmatrix} \begin{pmatrix} I_L \\ I_R \end{pmatrix} \tag{17}$$

Here, the matrix components of $\hat{r}$ and $\hat{t}$ denote the reflexion and transmission probabilities for right-moving states incoming from the left, and the components of $\hat{r}'$ and $\hat{t}'$ the probabilities for left-moving states incoming from the right. The current conservation implies that $\hat{r}^\dagger\hat{r} + \hat{t}^\dagger\hat{t} = I$.

The eigenvectors of the matrices $\hat{t}^\dagger\hat{t}$ and $\hat{r}^\dagger\hat{r}$ are called eigenchannels. Both matrices are positive definite and their eigenvalues denoted by τ_i, are real numbers between 0 and 1. In the base of eigenchannels the transport problems are solved as a superposition of problems of independent conductors. The conductance for two terminals configuration is given by

$$G = G_0 \cdot Tr\left[\hat{t}^{\dagger}\hat{t}\right] = G_0 \sum_{i=1}^{N_L} \tau_i \tag{18}$$

The last expression is the simplest form of the so-called Landauer formula. This formula is valid for ballistic systems at very low temperatures and low bias voltage.

1.5 Green's functions and tight-binding models

The calculation of the conductance in the equilibrium case requires obtain all the eigenchannels of the constriction to be filled up according to the Fermi-Dirac distribution function (7). The Green's functions formalism provides a powerful, consistent and systematic framework for modelling atomic-sized contacts.

Considers the Hamiltonian divided in three parts: H_C describes the constriction plus the leads, and H_L and H_R describe the left and right electrode respectively [11].

$$H = \begin{pmatrix} H_L & V_{LC} & 0 \\ V_{CL} & H_C & V_{CR} \\ 0 & V_{RC} & H_R \end{pmatrix} \tag{19}$$

Here, V_{LC}, V_{CL}, V_{RC} and V_{CR} describe the coupling between the central part and the electrodes.

The retarded, g^+, and advanced, g^-, Green's functions of the separated parts L, R and C are defined as

$$g^{\pm}_{L,R,C} = \lim_{\varepsilon \to 0^+} (E \pm i\varepsilon - H_{L,R,C})^{-1} \tag{20}$$

The Green's functions are directly related to the local densities of states (*LDOS*) by

$$LDOS = \pm \frac{1}{\pi} \mathrm{Im}[g^{\pm}] \tag{21}$$

The Green's function of the complete system, $G(E)$, obtained by coupling the electrodes to the central part is defined as

$$(E - H)G(E) = I \tag{22}$$

In matricial notation (22) can be rewritten as

$$\begin{pmatrix} E \pm i\varepsilon - H_L & -V_{LC} & 0 \\ -V_{CL} & E \pm i\varepsilon - H_C & -V_{CR} \\ 0 & -V_{RC} & E \pm i\varepsilon - H_R \end{pmatrix} \begin{pmatrix} G^{\pm}_L & G^{\pm}_{LC} & G^{\pm}_{LR} \\ G^{\pm}_{CL} & G^{\pm}_C & G^{\pm}_{CR} \\ G^{\pm}_{RL} & G^{\pm}_{RC} & G^{\pm}_R \end{pmatrix} = \begin{pmatrix} I & 0 & 0 \\ 0 & I & 0 \\ 0 & 0 & I \end{pmatrix} \tag{23}$$

Selecting the three equations from the second column and using the definitions of the Green's functions (20) we obtain

$$-V_{CL}g_L^{\pm}V_{LC}G_C^{\pm}+(E-H_C)G_C^{\pm}-V_{CR}g_R^{\pm}V_{RC}G_C^{\pm}=I \tag{24}$$

At this point it is convenient to define the Self-energies, Σ, and the Scattering rates or Broadening, Γ, as:

$$\Sigma_{L,R}^{\pm}=V_{CL,CR}g_{L,R}^{\pm}V_{LC,RC} \qquad \Gamma_{L,R}^{\pm}=-2\,\mathrm{Im}(\Sigma_{L,R}^{\pm}) \tag{25}$$

by using (24) and (25) we obtain an expression for the Green's function of the coupled central part

$$G_C^{\pm}=\left(E-H_C-\Sigma_L^{\pm}-\Sigma_R^{\pm}\right)^{-1} \tag{26}$$

The conductance at zero temperature and low bias voltage can be expressed in terms of Green's functions as [2, 12]

$$G=G_0Tr\left[\Gamma_L^-G_C^-\Gamma_R^-G_C^+\right]=4G_0Tr\left[\mathrm{Im}\left(\Sigma_L^-\right)G_C^-\,\mathrm{Im}\left(\Sigma_R^-\right)G_C^+\right] \tag{27}$$

This expression is exactly the Landauer formula (18), by using the cyclic property of the trace (27) can be rewriten as

$$G=G_0Tr\left[\left(\Gamma_R^-\right)^{1/2}G_C^-\left(\Gamma_L^-\right)^{1/2}\left(\Gamma_L^-\right)^{1/2}G_C^+\left(\Gamma_R^-\right)^{1/2}\right]=G_0Tr\left[\hat{t}^{\dagger}\hat{t}\right] \tag{28}$$

where $\hat{t}$ has been defined as

$$\hat{t}=\left(\Gamma_L^-\right)^{1/2}G_C^+\left(\Gamma_R^-\right)^{1/2} \tag{29}$$

Tight-binding models provide a simple description of electron states in solids that can be considered as complementary to the free electron model. Contrary to the free electron picture, the tight-binding model describes the electronic states starting from the limit of insolated-atom orbitals. This model permits to take into account the atomic structure of the constriction. In the Appx. A, we have illustrated the application of Green's functions formalism within a tight-binding model that represents a chain of gold atoms between two electrodes.

1.6 Ab-initio calculations and NEGF formalism

An accurate description of the electron transport through atomic-sized conductors requires a first-principles calculation. First-principles or ab-initio calculations are based on assumptions and approximations, without using quantities derived from experiments. The Density Functional Theory (DFT) is a widely used method to investigate the electronic structure in systems composed up to several hundreds of atoms. DFT was given a formal footing by two theorems introduced by Hohenberg and Kohn [13] in 1965. Two years after,

Kohn and Sham [14] formulated the equations required for the application of DFT to interesting problems of solid state physics and quantum chemistry.

Since electrons are much lighter than nuclei, they move much faster, and we can decouple the electron dynamics from the dynamics of the nuclei, using the Born-Oppenheimer approximation. The main idea is to describe the ground-state of an interacting system of electrons via its electron density and not via its many-body wavefunction. The DFT formulation establishes that the energy of a many-electron system, is a functional of its electron density, and the correct ground-state density minimizes this functional.

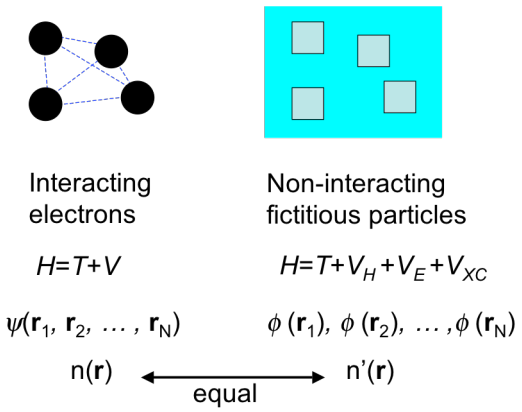

Figure 1.5: Scheme showin the differences between the many-body problem and the DFT formulation. Interacting electrons are described as non-interacting particles in an effective potential given by the Coulomb interaction between electrons (V_H), a static external potential (V_E) and the exchange and correlation interactions (V_{XC}). The electron density is the same in both cases.

While DFT in principle gives a good description of ground-state properties[(4)], the exact expression of this functional is unknown and practical applications of DFT are based on approximations for the so-called exchange-correlation energy functional. The exchange-correlation potential describes the effects of the Pauli principle and the Coulomb potential beyond a pure electrostatic interaction of the electrons. The most common density functionals are local density (LDA) and generalized gradient approximations (GGA). By using these approximations the Kohn-Sham equations can be solved by self-consistence. It involves iterations with alternate solving of the Poisson and Schrödinger equations.

(4) Every measurable physical quantity or observable is related with the energy and derivates of the energy.

The Non-equilibrium Green's functions (NEGF), also named as Keldysh formalism, is the current theoretical framework used to investigate the electron transport of atomic-sized contacts and molecular junctions. This formalism permits to calculate time-dependent expectation values such as currents and densities in systems under strong electric fields. A detailed description of this technique can be found in [4].

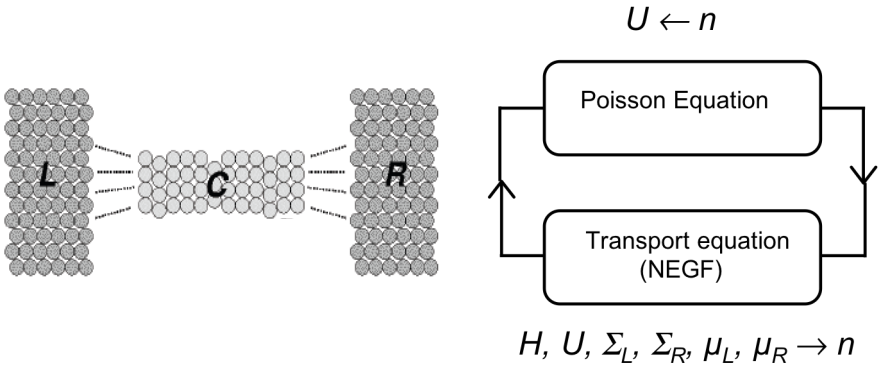

Figure 1.6: Scheme showing the electron transport problem descomposed in NEGF formalism (Left). Self-consistence diagram in NEGF formalism

1.7 Atomic-sized contacts and single molecule junctions

Atomic-sized constrictions connecting two macroscopic metallic electrodes can be realized using scanning tunneling microscopy or mechanically controllable break junction techniques (see Chap. 2). The electronic transport through such structures is suitably described by the Landauer-Büttiker formalism. Since the minimum cross section of the constriction is comparable to the Fermi wavelength (typically $\lambda_F \leq 0.5$ nm in metals), the contact has only a small number N_c of conduction channels. Each of the N_c channels has associated a transmission coefficient T_n between 0 and 1. The total conductance of the contact is given by the Landauer formula,

$$G = G_0 \sum_{n=1}^{N_c} T_n \tag{30}$$

The number of channels contributing to the conductance and their transmission coefficients, T_n, fully determines the transport properties of the contact and is known as the PIN code of the junction. For a given contact realization the PIN

code depends on the material forming the contact [15, 16], detailed atomic arrangement and applied stress [17]. Although the atomic structure of contacts can be quite complicated, as soon as the weakest point is reduced to just a single atom the complexity is removed. In most of the metals the last conductance value just before the rupture appears between 1 and 3 G_0. Scheer *et al.* [16] showed that this value correspons to a single-atom contact and, the number of channels that can be transmitted through the constriction is associated with the number valence orbitals. The experimental determination of the number of channels exploits the non-linearities of the current-voltage characteristic for contacts in the superconducting state. An almost completely open channel is found for monovalent metals (like Au, Ag) and, three and five partially open channels for sp-metals (like Al, Pb) and sd-metals (like Nb) respectively.

In contrast to atomic-sized contacts, the conductance of single molecule junctions is typically orders of magnitude smaller than G_0. A molecule attached to metallic electrodes acts as a potential well with localizated electronic states or molecular orbitals. In most of the molecular junctions studied, as the alkane chains investigated in this thesis, the Fermi level of the metal electrodes lies within a large HOMO-LUMO gap of several electron volts. In the low-bias(5) regime, the conductance of single molecule junctions can be described by the Landauer-Büttiker formalism with a single conductance channel,

$$G = G_0 T \tag{31}$$

where T is a function that reflects the efficiency of electron transmission from one electrode to the other. This transmission function can be roughly divided into components as follows,

$$T = T_{LC} T_{mol} T_{CR} \tag{32}$$

where T_{LC} and T_{CR} give the efficiency of charge transport across the left and right contacts and T_{mol} reflects the charge transport through the molecule. One can approximates the coherent, non-resonant electron transport through molecules as electron tunneling through a rectangular barrier, in which case (see Sect. 2.2)

$$T_{mol} = \mathrm{e}^{-\beta l} \tag{33}$$

where l is the width of the barrier, i.e. the length of the molecule, and β is the tunneling decay factor with units of $(\text{length})^{-1}$.

In atomic-sized contacts, calculations based on DFT and NEGF formalism reproduce with reasonable accuracy the experimental results [18, 19]. However,

(5) Voltages low enough to consider negligible the energy dependence of the density of states (DOS) of the electrodes. This is the so-called zero bias regimen in which the conductance does not depend of the bias voltage.

the calculated conductance of single molecule junctions differs up to several orders of magnitude with respect to the experimental results. Mainly there are two problems. Firstly, atomic-scale changes in the geometry or configuration of a given molecular junction seems to induce significant changes at the conductance. And secondly, DFT-based transport calculations are computationally very expensive and hence, this methodology is not useful to perform statistical studies where one wants to probe many different configurations. Current theoretical research focuses on the electronic structure at the interface between an organic molecule and a metal electrode and the proper geometry for a given molecular junction.

References

[1] N. Agraït, A.L. Yeyati and J.M. van Ruitenbeek, *"Quantum properties of atomic-sized conductors"*, Phys. Rep. 377 (2003) 81–279.
[2] S. Datta, Electronic transport in mesoscopic systems, Cambridge Univ Pr, 1997.
[3] I.O. Kulik and R. Ellialt o lu, Quantum mesoscopic phenomena and mesoscopic devices in microelectronics, Springer Netherlands, 2000.
[4] S. Datta, *"Nanoscale device modeling: the Green's function method"*, Superlattices and Microstructures. 28 (2000) 253-278.
[5] R. Landauer, *"Electrical resistance of disordered one-dimensional lattices"*, Philosophical magazine. 21 (1970) 863-867.
[6] M. Büttiker, *"Role of quantum coherence in series resistors"*, Phys. Rev. B. 33 (1986) 3020-3026.
[7] Y.V. Sharvin, *"Fiz., Zh. Eksp. Teor.(1965)"*, Sov. Phys. JETP. 21 984.
[8] J.A. Torres, J.I. Pascual and J.J. Sáenz, *"Theory of conduction through narrow constrictions in a three-dimensional electron gas"*, Phys. Rev. B. 49 (1994) 16581-16584.
[9] B.J. Van Wees, H. Van Houten, C.W.J. Beenakker, J.G. Williamson, L.P. Kouwenhoven, D. Van der Marel and C.T. Foxon, *"Quantized conductance of point contacts in a two-dimensional electron gas"*, Phys. Rev. Lett. 60 (1988) 848-850.
[10] D.A. Wharam, T.J. Thornton, R. Newbury, M. Pepper, H. Ahmed, J.E.F. Frost, D.G. Hasko, D.C. Peacock, D.A. Ritchie and G.A.C. Jones, *"One-dimensional transport and the quantisation of the ballistic resistance"*, Journal of Physics C: solid state physics. 21 (1988) L209.
[11] M. Paulsson, *"Non Equilibrium Green's Functions for Dummies: Introduction to the One Particle NEGF equations"*, Arxiv preprint cond-mat/0210519. (2002).

[12] T.N. Todorov, G.A.D. Briggs and A.P. Sutton, *"Elastic quantum transport through small structures"*, JOURNAL OF PHYSICS CONDENSED MATTER. 5 (1993) 2389-2389.
[13] P. Hohenberg and W. Kohn, *"Inhomogeneous electron gas"*, Phys. Rev. 136 (1964) B864-B871.
[14] W. Kohn and L.J. Sham, *"Self-consistent equations including exchange and correlation effects"*, Phys. Rev. 140 (1965) A1133-A1138.
[15] C. Sirvent, J.G. Rodrigo, S. Vieira, L. Jurczyszyn, N. Mingo and F. Flores, *"Conductance step for a single-atom contact in the scanning tunneling microscope: Noble and transition metals"*, Phys. Rev. B. 53 (1996) 16086-16090.
[16] E. Scheer, N. Agraït, J.C. Cuevas, A.L. Yeyati, B. Ludoph, A. Martín-Rodero, G.R. Bollinger, J.M. van Ruitenbeek and C. Urbina, *"The signature of chemical valence in the electrical conduction through a single-atom contact"*, Nature. 394 (1998) 154-157.
[17] J.C. Cuevas, A. Levy Yeyati, A. Martín-Rodero, G. Rubio Bollinger, C. Untiedt and N. Agraït, *"Evolution of conducting channels in metallic atomic contacts under elastic deformation"*, Phys. Rev. Lett. 81 (1998) 2990-2993.
[18] G. Rubio-Bollinger, S.R. Bahn, N. Agrait, K.W. Jacobsen and S. Vieira, *"Mechanical properties and formation mechanisms of a wire of single gold atoms"*, Phys. Rev. Lett. 87 (2001) 26101.
[19] T. Frederiksen, M. Brandbyge, N. Lorente and A.P. Jauho, *"Inelastic scattering and local heating in atomic gold wires"*, Phys. Rev. Lett. 93 (2004) 256601.

II

Experimental tools

The scanning tunneling microscope (STM) is a powerful tool for unraveling the topography, chemical composition and electronic properties of conductive surfaces at the atomic scale. In this thesis, we have used the STM-based break-junction technique (STM-BJ) to investigate the electronic transport properties of atomic-sized conductors. These include atomic wires and single molecule junctions.

In this chapter, we describe the experimental setup and techniques used throughout this thesis.

2.1 Scanning tunneling microscope (STM)

Since its invention by Binnig and Rohrer [1] in 1981, and subsequent Novel Price in Physics in 1986, the scanning tunneling microscope (STM) has revolutionized our ability to explore, and manipulate, matter at the atomic scale. The STM allows one to visualize regions of different electron density, and hence infer the position of individual atoms and molecules deposited on the surface of conductive materials. At first, the STM was used exclusively for imaging metal [2] and semiconductor [3] surfaces with atomic resolution. Nowadays, it has become a powerful tool able to manipulate and modify structures at atomic and molecular scale [4-6].

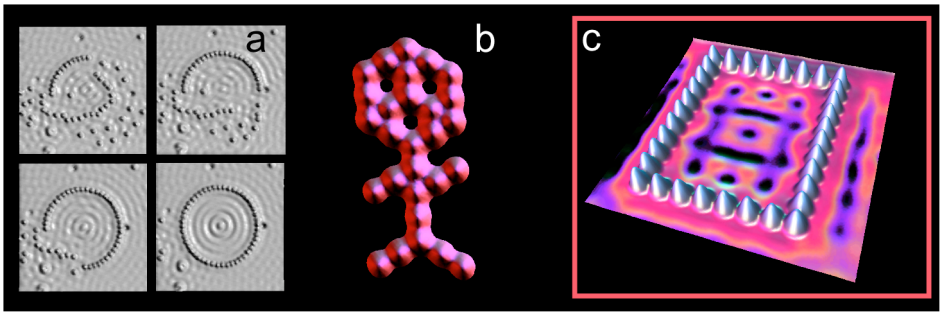

Figure 2.1: STM image gallery of IBM: (a) *The making of the circular corral (Iron on Coper (111)).* (b) *Carbon moxide man (Carbon monoxide on Platinum (111))* (c) *Rectangular corral (Iron on Coper (111)).*

In the STM configuration, a bias voltage is applied between a sharp metal tip and a conductive sample to be investigated. The tip can be moved accurately in three perpendicular directions (*x*, *y* and *z*), by a positioning system based on piezoelectric transducers (PZT) that expands or contracts in response to a change in applied voltage. When the tip is approached within 1-2 nm from the sample surface, a tunneling current will be established (see Sect. 2.2). The tunneling current depends exponentially on the precise distance between the last atom of the tip and the nearest atoms of the surface. By monitoring the tunneling current, we have very good control of the tip-sample distance.

There are two different operational modes of STM, the so-called constant current mode and the constant height mode as illustrated in Fig. 2.2. In both cases, the tip is moved across the sample surface in a raster pattern in the *x-y* plane (see Fig. 2.2 (a)). In constant current mode, a feedback loop system constantly monitors the tunneling current and adjusts the tip-sample distance to maintain a constant tunneling current (see Fig. 2.2 (b)). The tip adjustments as a function of scan position results in a topographic map of the surface. In the constant height mode, the tip scans in a horizontal plane above the sample surface and the tunneling current changes depending on topograpy and local surface electronic properties of the sample. In this mode, ajustment of the tip-sample distance is not required and therefore a high scan speed can be obtained. However, in order to prevent a tip crash, constant height mode is only applicable if the sample surface is very flat, which limits its applications somewhat.

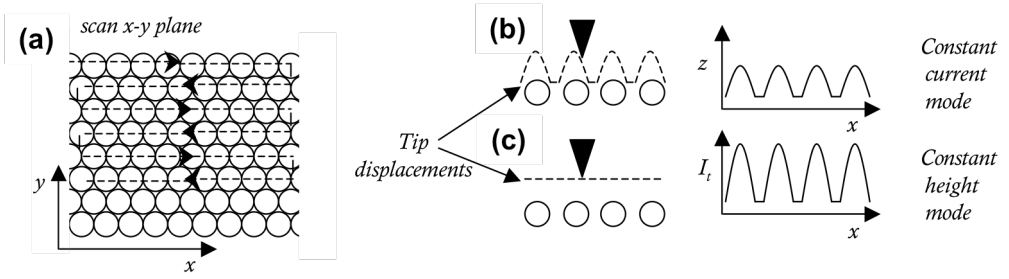

Figure 2.2: Basic operation modes of the STM: (a) *The tip is moved across the sample surface in a raster pattern in the x-y plane.* (b) *In the constant current mode, the z position is adjusted to maintain a constant* I_t. (c) *In the constant height mode, the tip travels in a horizontal plane above the sample and the tunneling current is recorded.*

The resolution of the STM depends on the geometry of the tip and sample and on their respective electronic structure. Typically, a good resolution is considered to be 0.1 nm lateral resolution and 0.01 nm vertical resolution.

Quantum tunneling

In Fig. 2.3 the basic components of the STM setup are shown. A bias voltage is applied between the tip and the sample. After approaching tip and sample, the tunneling current is measured by means of a current amplifier with a gain of 10^6-10^9 V/A. The computer operating the STM controls the PZT voltages with millivolt accuracy. The feedback loop system is used to adjust the tip-sample distance during the scanning. The tunneling current and the adjustments in z position are recorded simultaneously using a data acquisition board installed in the computer.

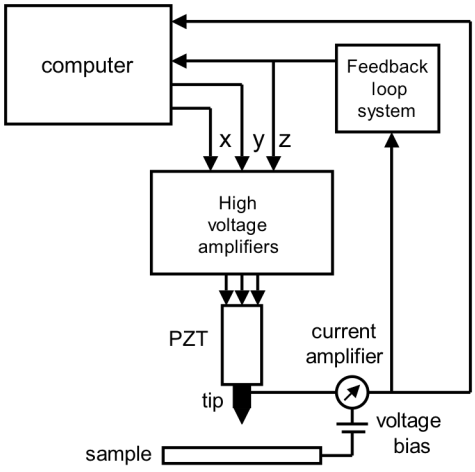

Figure 2.3: Scheme showing the basic components of the STM setup. A bias voltage is applied between the tip and sample and the tunneling current is measured by using a current amplifier. The tip positioning is controlled and recorded by a standard personal computer. The feedback loop system adjusts the tip-sample distance during scanning.

2.2 Quantum tunneling

The STM is based on the quantum tunneling of charge carriers. A simple model to understand the flow of charge carriers is to consider a particle of energy E and mass m, interacting with a 1D rectangular potential barrier of height V_0 and width d. The time-independent Schrödinger equation for this problem is

$$-\frac{\hbar^2}{2m}\frac{d^2\psi(x)}{dx^2}+V(x)\psi(x)=E\psi(x) \quad \text{with} \quad V(x)=\begin{cases} V_0 & 0\le x\le d \\ 0 & otherwise \end{cases} \qquad (1)$$

where $\hbar$ is the reduced Planck's constant ($\hbar = 1.054\cdot10^{-34}$ J s).

In the case of $E<V_0$, the wavefunction associated with the particle will show an exponential decay inside the barrier

$$\psi(x) = Ae^{-\alpha x} \tag{2}$$

where $\alpha = \sqrt{2m\phi/\hbar^2}$ is the decay rate and $\phi = V_0 - E$ is the effective barrier height.

We are interested in the transmission coefficient of the barrier T, defined as the ratio of transmitted to incident probability current densities. In the limit of a strongly attenuating barrier ($\alpha d \gg 1$), the transmission coefficient is given by

$$T \propto \exp\left(-2d\sqrt{2m\phi/\hbar^2}\right) \tag{3}$$

In classical physics, a particle cannot penetrate into or across a potential barrier if its energy is smaller than the potential height ($E<V_0$). However, a quantum mechanics treatment predicts a transmission coefficient non-zero and it depends exponentially on the barrier width d and the square root of the effective barrier height ϕ.

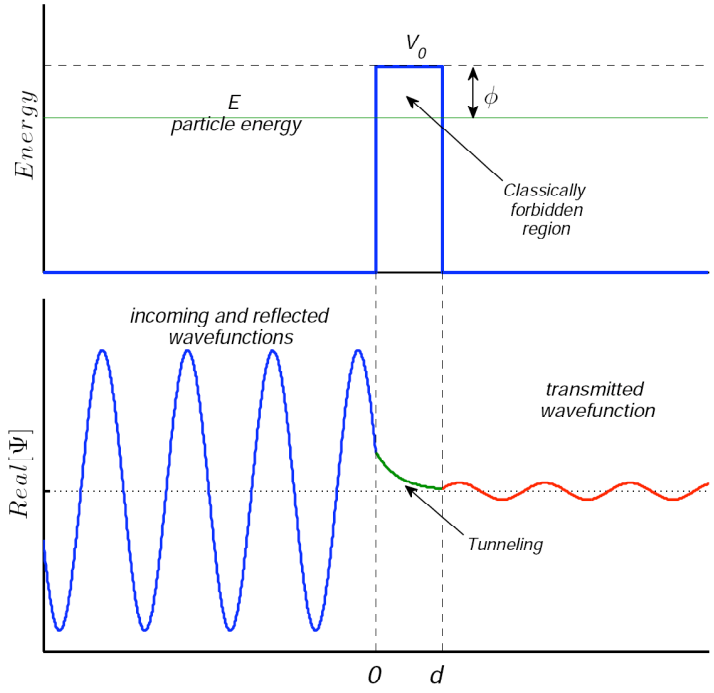

Figure 2.4: Quantum tunneling for a particle of mass m and energy E, interacting in a rectangular potencial barrier. The incident wavefunction of the particle has non-zero probability to be transmitted through the barrier.

Quantum tunneling

Think about two conducting electrodes separated by a vacuum gap. The conduction electrons can move freely in the electrode, but the potential in the vacuum region acts as a barrier to electrons between the two electrodes. However, if the barrier is thin enough (1-2 nm), an incident electron can tunnel through the potential and pass to the other electrode. If a bias voltage is applied between the electrodes, V, the electron transfer by quantum tunneling will become asymmetric, which induces a tunneling current, I_t, flowing through the barrier. In first approximation, the tunneling current is proportional to the transmission coefficient of the barrier (3)

$$I_t \propto \exp\left(-1.025 d\sqrt{\phi}\right) \tag{4}$$

where we have used the electron mass (m_e=9.109·10^{-31} kg), d is given in angstroms (1 Å=0.1 nm) and ϕ in electronvolts (1 eV=1.602·10^{-19} J).

In general, the effective barrier height ϕ depends on the material, its cristallographic orientation and the experimental conditions. For clean metal surfaces measured in vacuum, ϕ is given approximately by the surface work function(1). From equation (4) it can be observed that for a barrier height of ϕ=5 eV, that correspond to the work function of gold, the tunneling current decays one order of magnitude, when the tip-sample distance is increased by 1 Å. The extreme sensitivity of the tunneling current to the precise distance between the electrodes, led to Binnig and Rohrer to the idea that, a microscope based on the quantum tunneling should provide extremely high spatial resolution. In Fig. 2.5 we show three STM images of Au(111) surfaces measured in ambient conditions. The images correspond to different areas in different positions of the sample. In two of them we can observe steps that correspond to one atom in height.

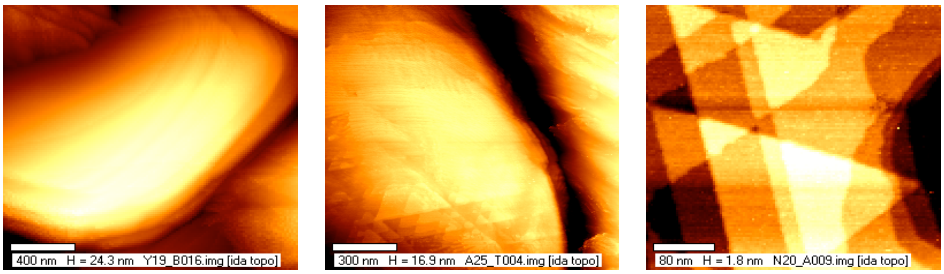

Figure 2.5: STM images of Au(111) surfaces with monoatomic steps measured with our STM under ambient conditions. The bias voltage was 200 mV and the tip was a freshly cut gold wire.

(1) The work function is the energy needed to move an electron from the Fermi level into the vacuum.

2.3 STM break junction technique (STM-BJ)

In addition to imaging conductive surfaces with atomic resolution, the STM give us the opportunity to measure the physical properties of materials down to the atomic scale. Soon after the invention of the STM, in 1986, Gimzewski and Möller [7] measured the electrical resistance while the tip was approached towards the substrate. They investigated the evolution of the resistance from tunneling to contact regimes. Using a gold tip and a gold sample, it is possible to form a metallic contact by gently touching the sample with the tip. After this indentation, the tip is retracted and the contact reduces its cross sectional area until it finally breaks. Pascual *et al.* [8] and Agrait *et al.* [9] observed that the conductance $G=I/V_b$, of a contact consisting few atoms in cross-section (see Fig. 2.6) shows preferentially values near to integer multiples of $G_0=2e^2/h$, where e is the electron charge and h is the Planck's constant. In the graph of Fig. 2.6 it is shown the conductance G, as a function of the tip displacement z, during the retraction of the tip (blue) and the subsequent tip indentation into the sample (red).

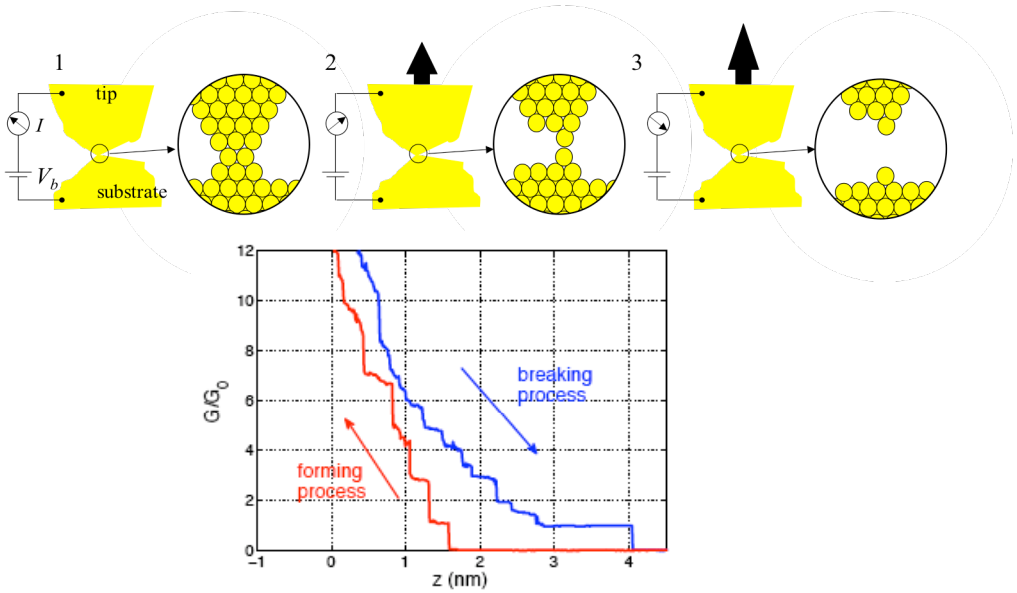

Figure 2.6: Cartoon showing the rupture of an atomic-sized gold contact by using the STM-BJ technique: (1) Retraction of the tip results in a controlled thinning of the contact. (2) Just before rupture a single atom contact is formed. (3) Finally the contact breaks. Graph: Conductance evolution as a function of the tip displacement, during the rupture (blue curve) and formation (red curve) of a gold contact at 4.2 K.

STM head

A technique closely related to the STM-BJ, is the mechanically controllable break junction (MCBJ). The break junction concept has its origin in the work done by Moreland and Ekin [10] in 1985. This idea was extended to atomic-sized contacts by Muller *et al.* [11]. In the simplest MCBJ setup, a notched wire of a material, that one wants to investigate, is fixed at two closely spaced spots on top of a flexible substrate. By bending the substrate, the narrowest part of the wire is pulled apart until finally lead to the rupture. If the bending force applied to the substrate is relaxed, these fracture surfaces can be brought again into contact. The conductance through the junction is measured continuously in successive cycles breaking and forming contacts. The three-point bending configuration depicted in Fig. 2.7, provides a greater mechanical stability than the STM. In the last years, more sophisticated design of MCBJ has been developed by using electron beam lithography, electrochemical deposition or electromigration. These instruments have been widely used to investigate the electronic transport properties of single molecule junctions.

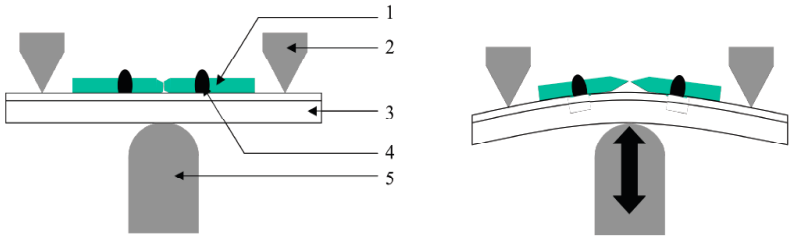

Figure 2.7: Schematic view of a MCBJ: (1) *notched wire,* (2) *two fixed counter supports,* (3) *flexible substrate or bending beam,* (4) *drops of epoxy adhesive and* (5) *the stacked piezo element*.

In this thesis, we have used the STM-BJ technique to investigate the electronic properties of atomic wires of gold (Chap. 3) and molecular junctions between gold electrodes (Chap. 4 and 5). The experimental arrangement and the measurements performed are described and discussed in the corresponding chapters.

2.4 STM head

Most of the results shown throughout this thesis have been obtained by using the STM head shown in Fig. 2.8. This home-built STM is inspired by the design of Pan *et al.* [12] and it is mostly oriented to work at low temperatures. However, we have used it both in molecular solution under ambient conditions (Chap. 4) as well as in cryogenic vacuum at low temperatures (Chap. 3 and 5).

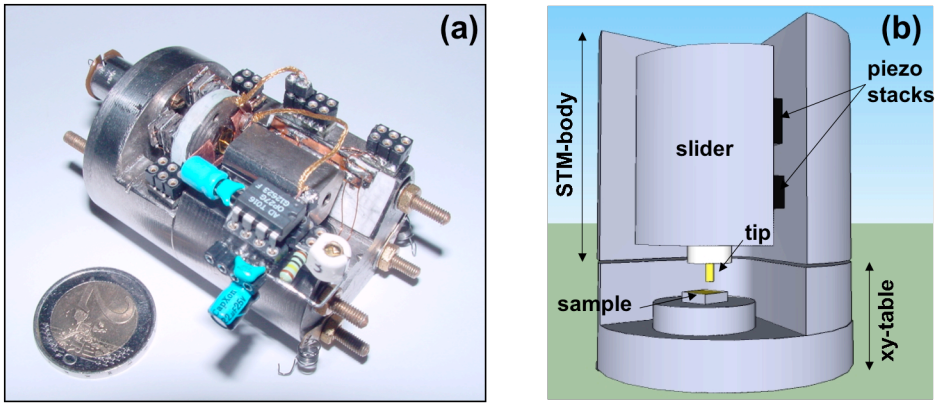

Figure 2.8: Picture of the STM used for performing the measurements in molecular solution at room temperature as well as in cryogenic vacuum at low temperature (a). *Scheme showing the most characteristic pieces of the STM* (b).

As we have mentioned in previous sections the positioning system of the STM is based on PZT. The PZT are ceramic materials that show a marked piezoelectric effect (see Fig. 2.9). An applied voltage across a PZT produces a macroscopic deformation (up to 0.2%) of the material. In good approximation, for a certain range of voltages, the deformation scales linearly with the applied voltage. The sensitivity of the PZT material used in our STM head is on the order of a few Å /V.

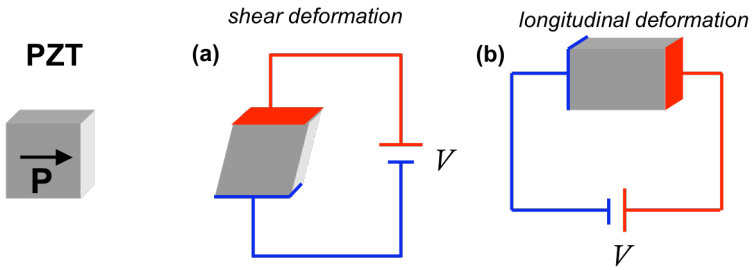

Figure 2.9: Longitudinal and shear deformations in a PZT can be controlled through the applied voltage.

The STM head is composed of two parts:
- The STM body and the slider used for fixing the STM-tip.
- The x-y table where the sample is placed.

STM body and the slider

2.4.1 STM body and the slider

The STM body, the slider and the x-y table are made of titanium, which is a material with a high strength-to-weight ratio and a small coefficient of thermal expansion. In Fig. 2.10 the pieces of the STM body are shown separately. A mobile slider with alumina laminae on both sides is held against four piezo stacks with an adjustable spring. The tip holder consists of a piece of hypodermic needle glued to a screw, which is fixed to the slider. The tip is attached inside the needle.

Each piezo stack is built by using four piezoelectric plates(2) assembled by means of 0.125 mm thick cooper sheets, which are glued with silver epoxy(3). The piezoelectric plates are connected in such a way, that their individual piezoelectric deformations are added (see Fig. 2.11). On top of each piezo stack, an alumina lamina has been glued by using Stycast epoxy(4) which is an excellent low temperature adhesive.

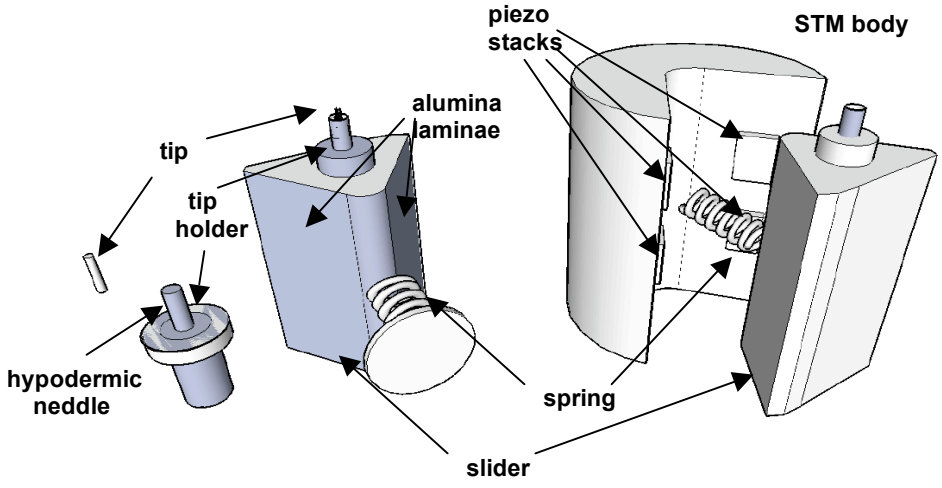

Figure 2.10: Pieces of the STM body used in this thesis: A piece of hypodermic neddle glued to a screw is used as tip holder and is fixed to the slider. The slider has alumina laminae on both sides and it is hold againts four piezo stacks with an adjustable spring.

(2) PZ26 of Ferroperm Piezoceramics. Website: www.ferroperm-piezo.com
(3) RS Catalog No. 496-265. RS Components Spain.
(4) 2850 FT mixer with a 7% weight of catalyst 24 LV. Emerson & Cumings.

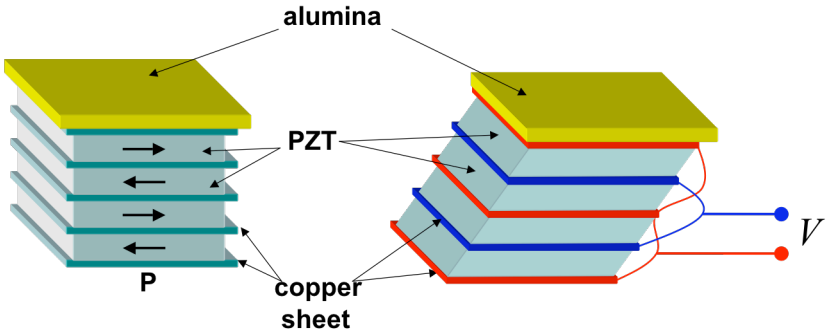

Figure 2.11: Scheme of a shear piezo stack as used in the STM. Four piezoelectric plates are assembled by means of cooper sheets glued with silver epoxy. The black arrow indicate the polarization of the piezoelectric plates. On top of each piezo stack an alumina lamina is glued. A voltage applied, V, produces a shear deformation of the piezo stack.

An important consideration in the STM design is the implementation of the coarse positioning system. The coarse positioning system serves to approach the tip sufficiently close to the sample surface to observe the tunneling current. At short distances, the linear deformations of the piezo stacks provide vertical displacements of the STM-tip in the range from 0.05 to 100 nm, at room temperature. The calibration method is described in the Appx. B.

The coarse positioning system of our STM is operated using the stick-slip motion induced by four shear piezo stacks, as an inertial piezoelectric motor. In Fig. 2.12 we show and scheme of the coarse motion mechanism. A voltage sawtooth wave is applied simultaneously to the four piezo stacks. The slider moves together with the piezo stacks in the ramp of the wave, however, the inertia of the slider produces the slip[(5)] between alumina laminae in the jump of the signal. By the stick-slip mechanism, the slider can be moved in the desired direction distances on the order of millimetres in successive cycles controlled by a voltage sawtooth wave.

(5) In order to facilitate the slip, alumina laminae of the slider and piezo stacks are carefully cleaned with ethanol for removing organic residues and covered with graphite as solid lubricant.

STM body and the slider

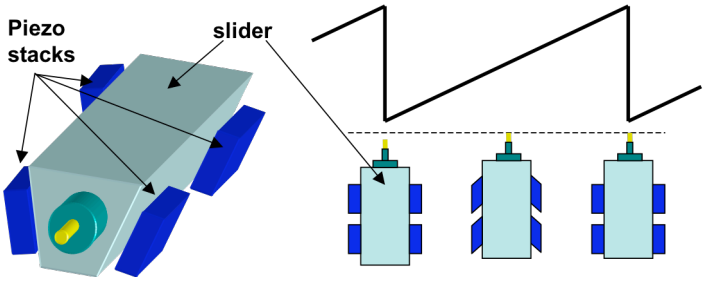

Figure 2.12: Scheme showing the coarse motion of the STM-tip. The slider moves together with the piezo stacks in the ramp of the wave and slip in the jump of the signal.

In some experiments we have used a slider with an extra piezo tube. The piezo tube is a piezo actuator radially polarized. The outer part is segmented into four quadrants ($\pm x$ and $\pm y$), each connected to a separate electrode and another electrode covers the inner part of the tube ($+z$). An applied voltage difference between opposite quadrants causes the deflection of the piezo tube (see Fig. 2.13). The voltage applied to the inner electrode controls the expansion or contraction of the entire tube. By fixing the STM-tip at the end of the piezo tube, it can be moved in three perpendicular directions x, y and z.

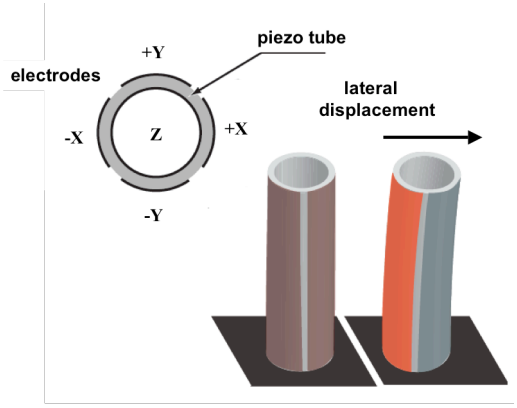

Figure 2.13: Piezotube. The outer part is outer part is segmented into four quadrants (±x and ±y), each connected to a separate electrode and another electrode covers the inner part of the tube (+z).

2.4.2 The x-y table

A great advantage of the STM compared with MCBJ is the possibility of changing the position of the tip over the sample surface. Sometimes, the spot where the contacts are made is contaminated and it is necessary to change the

contact area. For this reason, the possibility of changing the STM-tip position over the sample surface during the experiment is very useful.

In Fig. 2.14 the separated parts of the x-y table are shown. A mobile disk with an alumina lamina glued in its base is used as sample holder. The disk is held against three piezo stacks with an adjustable spring. Each stack is composed by a pair of piezo stacks oriented in *x* and *y* directions (see Fig. 2.15). The coarse and fine motions operate as we have described for the case of the body, but the table can be moved in two perpendicular directions.

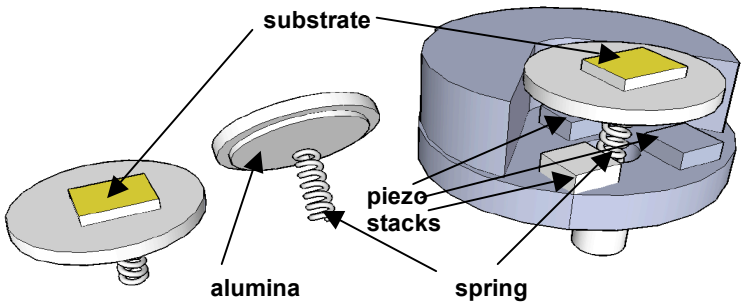

Figure 2.14: Pieces of the x-y table of the STM: A mobile disk with an alumina lamina glued in its base is used as a sample holder. This disk is hold against three piezo stacks with an adjustable spring.

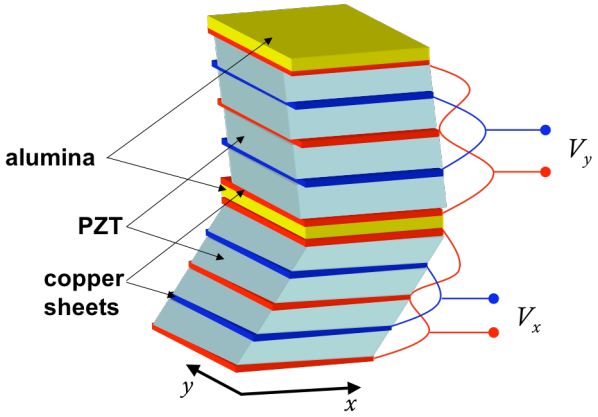

Figure 2.15: Scheme of a piezo stack as used in the x-y table of the STM. The voltages Vx and Vy are used to move the sample in the x-y plane.

The control unit

To perform different experiments we have used three different configurations of the STM head. The most stable configuration has only one mobile piece, the slider. This allows the movement of the STM-tip normal to the sample (Fig. 2.16 (a)). The contact area can be changed moving x-y table manually. The second configuration uses the piezo stacks of the STM body and the x-y table. It permits to move the STM-tip over the sample and imaging the sample surface (Fig. 2.16 (b)). The most versatile configuration adds a slider with a piezo tube. The STM-tip on the end of the piezo tube can be moved in *x*, *y* and *z* (Fig. 2.16 (c)).

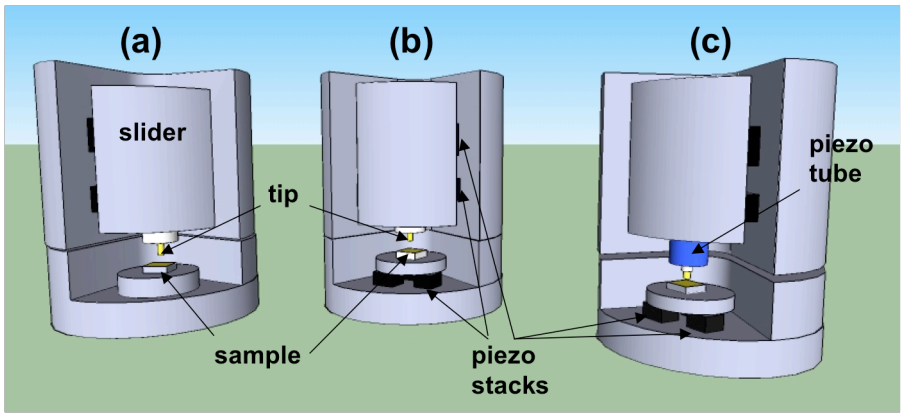

Figure 2.16: Scheme of the different configurations of the STM head. (a) The most stable configuration allows STM-tip movements normal to the sample. (b) By using the x-y table, the sample can be moved in x and y. (c) A slider with a piezo tube permits movements of the STM-tip in x, y and z.

2.5 The control unit

The STM's control box consists of two units: one used for low voltages (up to ±15V) and other for high voltages (up to ±140V). The low voltages unit includes some analog devices like filters, adders, current-to-voltage converters, divisors, proportional-integral controllers, etc, for conditioning the electrical signals of the STM. The high voltages unit contains high-voltage amplifiers used to produce the movements of the STM. This STM control box has been designed in the laboratory and built in the workshop of the Universidad Autónoma de Madrid (SEGAINVEX).

To record the signals, the electronic devices are connected to a data acquisition board (DT2823 Data Translation) installed in a standard personal computer. To control the movements of the STM a Digital-to-Analog board (PIO96) is also

installed in the computer. The software used, written in Delphi, has been completely developed in the Laboratorio de Bajas Temperaturas of Universidad Autónoma de Madrid (LBT-UAM).

Especially important has been the development of a current-to-voltage amplifier for the measurements of molecular junctions at room temperature. For our purposes it is required to measure the conductance continuously in a wide range. For this reason, we have built a current amplifier whose electronic scheme is showed in Fig. 2.17.

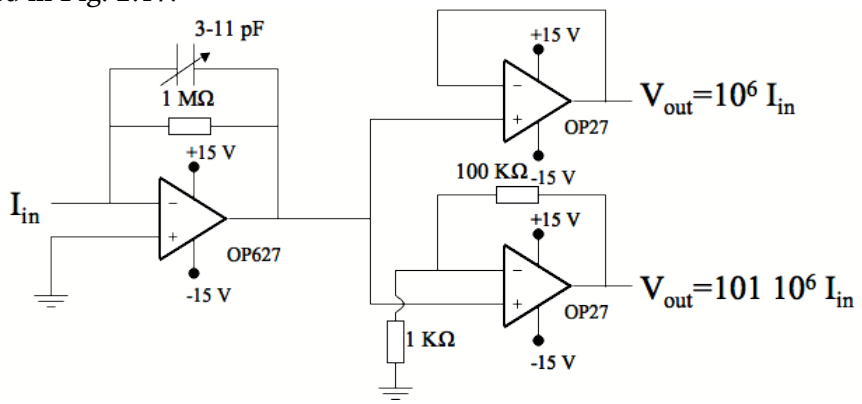

Figure 2.17: Electronic scheme of the current amplifier used for the measurements at room temperature. This configuration allows to measuring the conductance over more than four orders of magnitude.

The current is measured by using a current to voltage converter (10^6 V/A). After this stage the signal is divided in two: one is again aplified (1.01 10^8 V/A) and the other goes through a buffer. These signals are registered by using a two channel of the acquisition data board. This configuration allows to measuring the conductance continuously over more than four orders of magnitude.

For the data analysis it is very important to calibrate correctly the gain of the stage amplifiers as well as subtract the offset in current. The offset in current changes slowly in time, due to changes in the temperature of electronic devices, and it has been corrected in groups of curves during the data analysis. The gain calibration was performed using two resistances with low tolerance (<5%). The first stage 10^6 V/A, was calibrated with a resistance of 100 KΩ and the second stage 1.01 10^8 V/A with a 1 MΩ resistance. The resistance is placed as a contact, using the same configuration than for the measurements. By applying a known bias voltage and measuring the current through the resistance, the gain is adjust for the current expected by the Ohm's law.

2.6 The Lock-in amplifier

The lock-in amplifier is an electronic device that can extract selectively the amplitude and the phase of the first harmonics (typically ω or 2ω) of a signal from a noisy environment. The measurement of the dI/dV it is a widely used method to characterize the electron transport in mesoscopic systems. The measurement of the dI/dV using a lock-in amplifier, requires to add a high-frequency (~kHz) modulation voltage to the bias voltage. The current as a function of voltage can be expressed as

$$I(V) = I(V_b + V_{\text{mod}} \cos(\omega t)) \tag{5}$$

where V_b is the bias voltage, and V_{mod} and ω are the amplitude and frequency of the introduced modulation. Typically the amplitude of the modulation is small (~mV) and the expression (10) can be rewritten as a Taylor series expansion

$$I(V) = I(V_b) + \left(\frac{dI}{dV}\right)_{V_b} V_{\text{mod}} \cos(\omega t) + \frac{1}{2}\left(\frac{d^2 I}{dV^2}\right)_{V_b} V_{\text{mod}}^2 \cos^2(\omega t) + O(V_{\text{mod}}^3) \tag{6}$$

Finally, by using a trigonometric double angle formula

$$I(V) = I(V_b) + \left(\frac{dI}{dV}\right)_{V_b} V_{\text{mod}} \cos(\omega t) + \frac{1}{4}\left(\frac{d^2 I}{dV^2}\right)_{V_b} V_{\text{mod}}^2 + \frac{1}{4}\left(\frac{d^2 I}{dV^2}\right)_{V_b} V_{\text{mod}}^2 \cos(2\omega t) + O(V_{\text{mod}}^3) \tag{7}$$

From the last expression, it can be observed that measuring the current at the frequency ω provides a signal directly proportional to dI/dV. By measuring the current at the frequencies 2ω, 3ω, 4ω, etc, we obtain signals related to higher derivates.

2.7 Scanning tunneling spectroscopy (STS)

The probability of finding a conduction electron outside of a metal is governed by the quantum tunneling. This basic consequence of quantum mechanics makes possible measurable electrical currents between two conductors separated by a sufficiently thin layer. Scanning tunneling spectroscopy (STS) is an experimental technique which uses a STM to probe the local density of states (*LDOS*). The *LDOS* of a sample describes the amount of electronic states that are occupied and unoccupied at each energy level. Generally, STS measurements involve the observation of changes in the differential conductance dI/dV (or its derivative d^2I/dV^2) as a function of the bias voltage in constant height mode [13] .

The information obtained by the STS technique can be understood on base to the Bardeen's formalism. In this framework the tunneling current as a function of the bias voltage is given by

$$I(V)=\frac{4\pi e}{\hbar}\int_{-\infty}^{\infty}d\varepsilon\left[f(E_F-eV+\varepsilon)-f(E_F+\varepsilon)\right]\rho_s(E_F-eV+\varepsilon)\rho_t(E_F+\varepsilon)\left|M\right|^2 \qquad (8)$$

where $f(E)$, is the Fermi-Dirac distribution function

$$f(E)=\frac{1}{1+\exp(E/k_BT)} \qquad (9)$$

and $\rho_s(E)$, $\rho_t(E)$ are respectively the density of states of sample and tip. The tunneling matrix element M is given by

$$M=\frac{\hbar}{2m}\int_{\Sigma}\left(\psi_s^*\frac{d\psi_t}{dz}-\psi_s\frac{d\psi_t^*}{dz}\right)dS \qquad (10)$$

where ψ_s, ψ_t are respectively the wave functions of the sample and the tip, and Σ is any surface lying entirely within the barrier region. Tersoff and Hamann [14] calculated M for a simplified geometry of the STM-tip. By assuming zero temperature and bias voltage negligible compared with the work function of the electrodes ($V \ll \phi/e$), the expression (5) simplifies to

$$I(V)\propto\int_0^{eV}\rho_s(E_F-eV+\varepsilon)\rho_t(E_F+\varepsilon)\,d\varepsilon \qquad (11)$$

Assuming a constant density of states of the tip, the differential conductance is essentially determined by the local density of states (*LDOS*) of the sample.

$$\frac{dI(V)}{dV}\propto\rho_s(E_F-eV) \qquad (12)$$

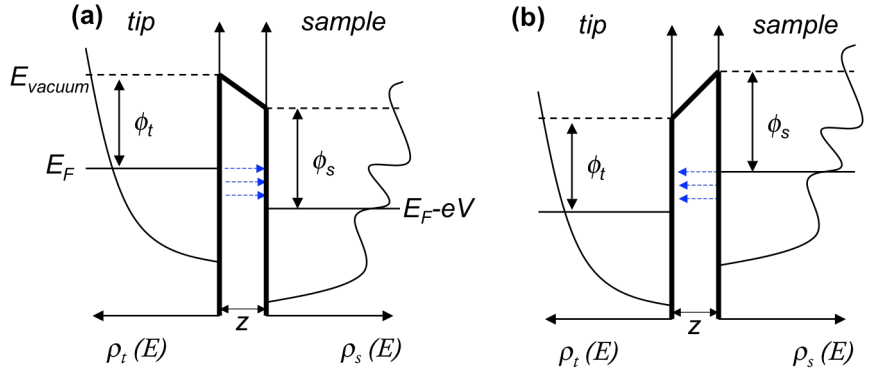

Figure 2.18: Energy band diagrams for a STM tunnel junction. (a) Positive sample bias, the electrons tunnel from occupied states of the tip into unoccupied states of the sample, whereas (b) at negative sample bias, the electrons tunnel from occupied states of the sample into unoccupied states of tip.

In Fig. 2.18 we show schematically the electron tunneling processes with a positive (a) and negative (b) bias voltage applied to the sample. As we can observe the STS signals can be used to explore the occupied and unoccupied electronic states of the sample.

2.8 Inelastic electron spectroscopy (IETS and PCS)

The previous discussion corresponds to elastic electron tunneling processes, for which the electron energy is equal in the initial and final states. However when absorvates are present in the barrier, some of the tunelling electrons suffer inelastic scattering processes, in which they lose energy by exciting vibrational modes. Inelastic electron tunneling spectroscopy (IETS) was discovered in 1966 by Jaklevic and Lambe [15] when they studied metal-oxide-metal junctions. Intead of finding band structure effects due to metal electrodes, they observed that the differential conductance dI/dV increased at certain bias voltages. These voltages were identified with vibrational frequencies of molecues contained in the barrier. A simple picture of elastic and inelastic transport processes for a symmetric tunnel junction is shown in Fig. 2.19. At low bias voltage (Fig. 2.19 (a)), an electron from an occupied state on the left side tunnels into an empty state on the right side, and the current increases linearly with the applied bias voltage (Fig. 2.19 (c)). However, if there is a vibrational mode of frequency ω inside the barrier, when the applied bias voltage is large enough $eV>\hbar\omega$, the electron can lose a quantum of energy, $\hbar\omega$, to excite the vibrational mode. This electron in a lower energy state will tunnel into another empty state on the right side. This phenomenon leads to the opening of an additional channel for tunneling and therefore an increase in the current. The minimum of energy required to excite the vibration is the onset of this inelastic processs (see Fig 2.19 (a) and (b)) and corresponds with a minimum bias voltage threshold. The characteristic features due to the onset of the vibrational excitation are positive increments in the dI/dV symmetrically observed at $V=\pm\hbar\omega/e$. Such effects are conveniently observed in the d^2I/dV^2 in which one then observes anti-symmetric peaks about $V=0$ (See Fig. 2.19 (c)).

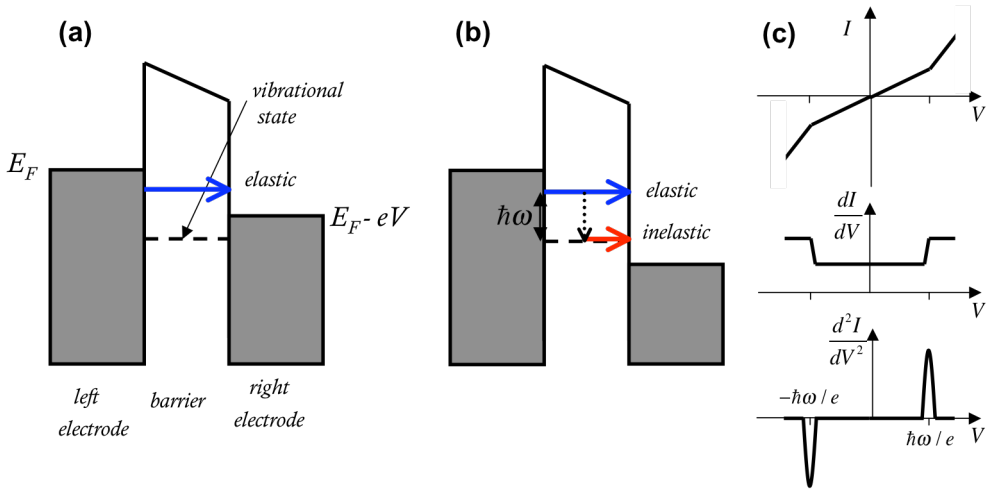

Figure 2.19: Schematic representation of elastic and inelastic electron transport of a symmetric tunnel junction. (a) In an elastic process the electron energy is equal in the initial and final states. (b) However, since the energy of electrons is $eV > \hbar\omega$ inelastic scattering processes are allowed and the electron energy changes due to the excitation of vibrational modes in the junction. (c) In such processes, an additional path contributes to the tunneling current. It is observed as symmetric jumps in the dI/dV and antisymmetric peaks in the d^2I/dV^2.

In 1974, Yanson [16] invented the point contact spectroscopy (PCS) by directly measuring the d^2I/dV^2 in metallic constictions of dimensions comparable or smaller than the mean free path of the electrons in the metal (up to ~100 nm at low temperatures). For PCS, in contrast to IETS, the differential conductance decreases at the threshold voltage corresponding to the vibrational mode energy $V=\pm\hbar\omega/e$. In this case, the transmission of the junction is quite high and the electrons are completely delocalized over the two electrodes. Therefore, it is necessary to consider the electronic states in the momentum space. As we show in Fig. 2.20 (a), the right-moving electronic states are occupied to a level eV higher than the left-moving states. When an electron suffers an inelastic scattering event, due to the Pauli exclusion principle, the electron should be back-scattered into an unoccupied left-moving state. It results, in a sudden decrease of the differential conductance at $V=\pm\hbar\omega/e$ (see Fig. 2.20 (b)).

Inelastic electron spectroscopy (IETS-PCS)

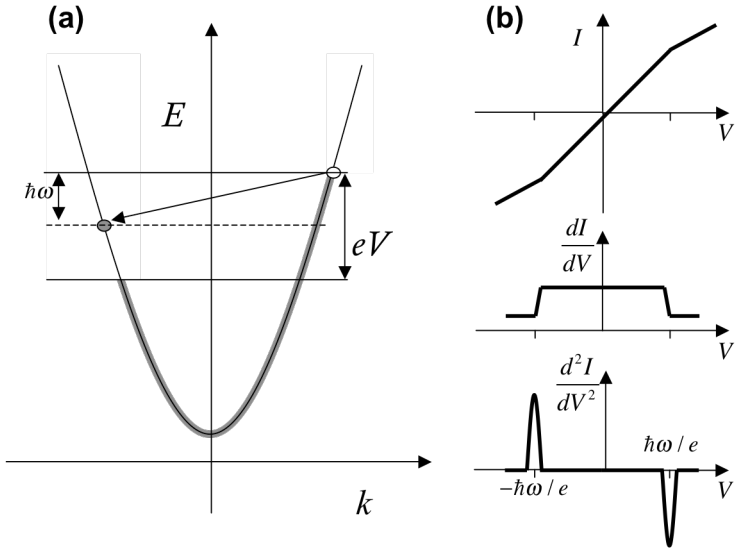

Figure 2.20: Schematic representation of inelastic scattering event of a constriction between metals. (a) In an inelastic scattering process an electron is scattered backwards into an unoccupied left-moving state. (b) Such processes, are observed as sudden decrease in the differential conductance dI/dV at the threehold voltage $V=\pm\hbar\omega/e$.

The IETS and PCS are closely related techniques. By using a lock-in amplifier (Sect. 2.6), we have measured the PC spectra of atomic wires of gold atoms (Chap. 3) and the IET spectra of metal-molecule-metal junctions (Chap. 5). In these chapters, we will discuss the application of these techniques for the study of such structures.

An important issue of these spectroscopic techniques is the width of the peak. In general, the width of the peak at a half maximum is given by,

$$W = \sqrt{\left(5.4\frac{k_B T}{e}\right)^2 + \left(1.7V_{\text{mod}}\right)^2 + \left(\Delta E\right)^2} \qquad (13)$$

where, k_B is the Boltzmann's constant, T is the temperature, e the electron charge, V_{mod} is the rms value of the modulation voltage applied (Sect. 2.6) and ΔE the intrinsic width of the peak. Features in a dI/dV can appear smoother or broader if the temperature or the modulation amplitude are higher than the characteristic energies of the phenomena to be studied.

2.9 Cryogenics

It can be considered that low temperature studies were born with the liquefying of helium by Kamerlingh Onnes in 1908. The low temperature environment allowed him the discovery of the superconductivity. For that, he was awarded the Nobel Prize in Physics in 1913. Many applications have emerged from low temperature studies like the use of superconductivity, high field magnets or low-noise and high-sensitivity instrumentation.

As we have mentioned, our STM head can operate in a wide range of temperatures. However, the control over the tip position is magnified at low temperatures. At low temperatures the thermal drift is negligible, the atomic mobility is very low and the creep effect in the piezoelectric ceramics is also reduced to a very low level [17]. One of the main aims of this thesis is to study the inelastic interactions between electrons and phonons in atomic-sized contacts and molecular junctions. For spectroscopic studies the temperature is an essential factor that limits the energy resolution of the measurements.

For the low temperature measurements carried out throughout this thesis, we have used a commercial ^{3}He cryostat(6). This instrument allows in a relatively easy way to maintain the STM at temperatures in the range from 80 K down to 250 mK. In Fig. 2.21 we show a scheme of the *dewar* and *insert* used for the measurements. The dewar is a vessel thermally insulated by a compartment at high vacuum filled with super insulation materials. The absence of liquid nitrogen as reservoir minimizes the mechanical vibrations.

The STM is attached to the base of the ^{3}He pot (see Fig. 2.20) by two ropes of copper wire 5 cm long. These ropes provide a good thermal contact with the ^{3}He pot and help to soften the mechanical vibrations. A receptacle hermetically closed, the pot, separates the STM from the thermal bath of ^{4}He. Before to start the cooling process, the gas in the pot is pumped out (vacuum ~10^{-6} mbar) and purged two or three times with helium gas. Finally a small quantity of high purity helium exchange gas (1 mbar of pressure at 300K) is introduced in the pot. The insert is now ready to be cooled down to 4.2 K.

(6) Heliox 2$^{AST\ VL}$ Oxford Instruments.

Cryogenics

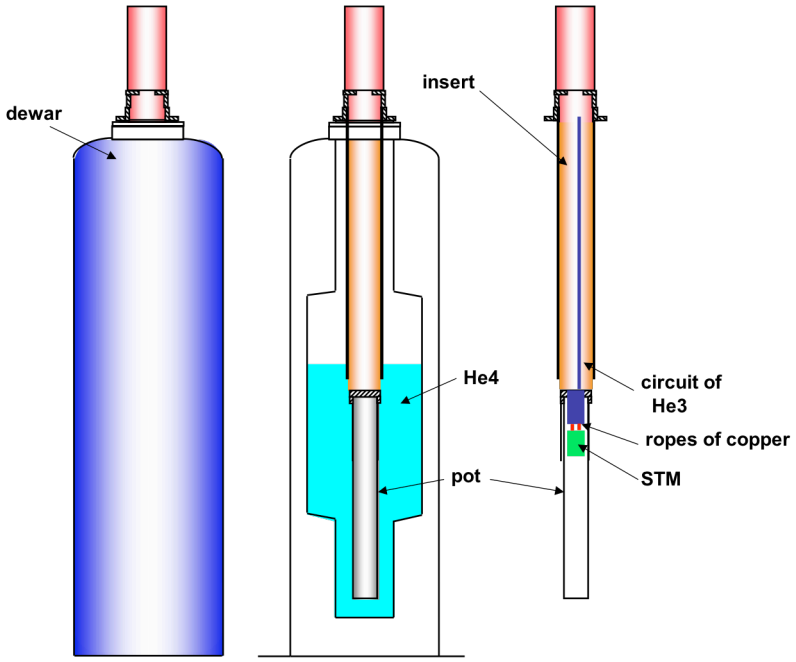

Figure 2.20: Scheme showing the dewar and insert used for measurements at low temperatures.

To perform measurements at 250 mK, it is necesary to disconnect thermally the STM from the ^{4}He bath at 4.2 K. For that, there are some cryopumps, the exchange gas sorb, which absorb the helium exchange gas inside the pot. The mechanism for cooling down to 250 mK is described in Fig. 2.21. Here, the ^{3}He is permanently contained in a close circuit. The 1 K plate is cooled down by circulating ^{4}He liquid through the 1 K pumping line and, the sorb is kept at 30 K. By this time, the ^{3}He is liquifying in the ^{3}He pot. Once the ^{3}He is condensed, the sorb is cooled thereby the ^{3}He is pumped through the circuit and the ^{3}He pot reaches a base temperature of 250 mK.

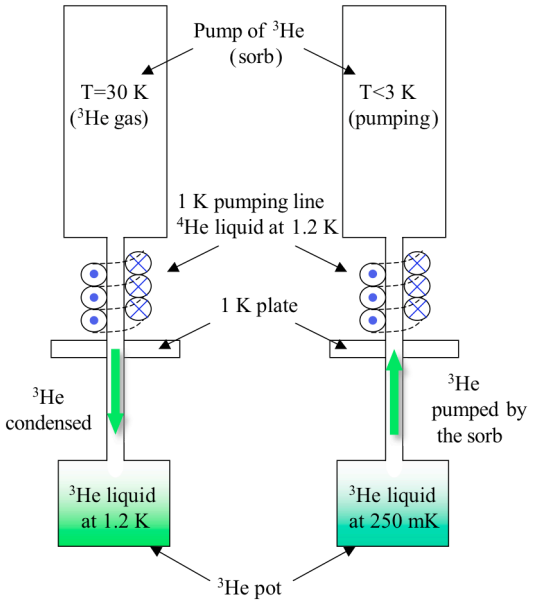

Figure 2.21: Mechanism for cooling at 250 mK. First, a gradient of temperature liquefy the He3 in the cold point (Left). Then, the He3 is pumped in a close circuit and the temperature decrease to 250 mK (Rigth).

In order to minimize the thermal contact between the STM and the outside environment, the experimental wiring on the insert is performed with steel wires with small thermal conductivity.

For attenuating the mechanical vibrations of the building, the insert and the dewar are suspended by elastic ropes of 7 m fixed to a metallic support placed on a pillar of the laboratory.

References

[1] G. Binnig, H. Rohrer, C. Gerber and E. Weibel, *"Surface studies by scanning tunneling microscopy"*, Phys. Rev. Lett. **49** (1982) 57-61.

[2] W.J. Kaiser and R.C. Jaklevic, *"Scanning tunneling microscopy study of metals: spectroscopy and topography"*, Surface Science. **181** (1987) 55-68.

[3] W.J. Kaiser and L.D. Bell, *"Direct investigation of subsurface interface electronic structure by ballistic-electron-emission microscopy"*, Phys. Rev. Lett. **60** (1988) 1406-1409.
[4] M.F. Crommie, C.P. Lutz and D.M. Eigler, *"Confinement of electrons to quantum corrals on a metal surface"*, Science. **262** (1993) 218-220.
[5] P. Zeppenfeld, C.P. Lutz and D.M. Eigler, *"Manipulating atoms and molecules with a scanning tunneling microscope"*, Ultramicroscopy(The Netherlands). **42** (1991) 128-133.
[6] B.C. Stipe, M.A. Rezaei and W. Ho, *"Single-molecule vibrational spectroscopy and microscopy"*, Science. **280** (1998) 1732.
[7] J.K. Gimzewski and R. Möller, *"Transition from the tunneling regime to point contact studied using scanning tunneling microscopy"*, Physical review. B, Condensed matter. **36** (1987) 1284.
[8] J.I. Pascual, J. Mendez, J. Gomez-Herrero, A.M. Baro, N. Garcia and V.T. Binh, *"Quantum contact in gold nanostructures by scanning tunneling microscopy"*, Phys. Rev. Lett. **71** (1993) 1852-1855.
[9] N. Agrait, J.G. Rodrigo and S. Vieira, *"Conductance steps and quantization in atomic-size contacts"*, Phys. Rev. B. **47** (1993) 12345-12348.
[10] J. Moreland and J.W. Ekin, *"Electron tunneling experiments using Nb Sn "break"junctions"*, Journal of Applied Physics. **58** (1985) 3888.
[11] C.J. Muller, J.M. Van Ruitenbeek and L.J. De Jongh, *"Experimental observation of the transition from weak link to tunnel junction"*, Physica C. **191** (1992).
[12] S.H. Pan, E.W. Hudson and J.C. Davis, *"He refrigerator based very low temperature scanning tunneling microscope"*, Review of Scientific Instruments. **70** (1999) 1459.
[13] R. Wiesendanger, 2*Scanning probe microscopy and spectroscopy: methods and applications"*, Cambridge Univ Pr, 1994.
[14] J. Tersoff and D.R. Hamann, *"Theory of the scanning tunneling microscope"*, Phys. Rev. B. **31** (1985) 805-813.
[15] R.C. Jaklevic and J. Lambe, *"Molecular vibration spectra by electron tunneling"*, Phys. Rev. Lett. **17** (1966) 1139-1140.
[16] I.K. Yanson, *"Non-Linear Effects in the Electrical Conductivity of Point Contacts and Electron-Phonon Interaction in Normal Metals"*, Zhur. Eksper. Teoret. Fiziki. **66** (1974) 1035-1050.
[17] S. Vieira, IBM J. Res. Dev. **30** (1986) 553.

III

Elastic and vibrational properties of atomic gold wires

An atomic wire of single gold atoms freely suspended between two gold electrodes is an ideal system to study quantum transport in detail. This system is very attractive because being so simple in structure it is amenable to detailed theoretical calculations using the state-of-the-art of ab-initio calculations of atomic structure and quantum transport.

In this chapter, we show a detailed study about elastic and vibrational properties of atomic gold wires. By combining results of point contact spectroscopy (PCS) and force measurements, it is possible to investigate the interatomic interaction between contiguous atoms [(1)].

3.1 Atomic-sized gold contacts

With the scaling down of the smallest line width that can be patterned as a part of an integrated circuit, we increase the number of electronic components per area on a chip. The progressive miniaturization of electronic devices based on semiconductors has stimulated a rapid development of electron beam lithography techniques. Nowadays, the minimum feature size patternable by conventional lithography is ~30 nm[(2)], which correspond to ~100 atoms in a row.

Atomic-sized contacts are structures where the number of atoms in the minimum cross-section ranges from tens of atoms to a single atom. Although there are several ways of preparing such structures [1], the experiments at low temperatures usually involve the use of techniques such as STM or MCBJ (Chap. 2). By using these techniques atomic-sized contacts are formed during the last stages of the breaking process of a contact formed between two clean metal surfaces. This method has been widely used in order to investigate the structure and electronic properties of metallic contacts of atomic size. The understanding of conductance at the atomic scale has advanced greatly over the last decade due to effort from both experiment and theory.

(1) Part of the work described here will be published in the paper: "Mechanical properties and vibrations of atomic chains: measuring the interatomic interaction". C.R. Arroyo, J.J. Riquelme, J.G. Rodrigo, G. Rubio-Bollinger and N. Agrait. In preparation.

(2) The Intel Core i7 processors are based on the 32 nm technology node.

The measurements shown in this chapter were performed using a home-built STM (Chap. 2) with a gold tip and a gold substrate, working at low temperatures (down to 250 mK). It is important to note the great difference between low and room temperature experiments. At low temperatures, there is no atomic diffusion on the surface of the metal and the thermal drift of the STM is negligible. In addition, as we have mentioned above, the fabrication of atomic-sized contacts requires clean metal surfaces. For many metals it suffices to clean the contacting surfaces in situ by indenting the tip into the substrate repeatedly. This cleaning procedure works particularly well at low temperatures and under cryogenic vacuum conditions where the contacting surfaces can stay clean for long periods of time.

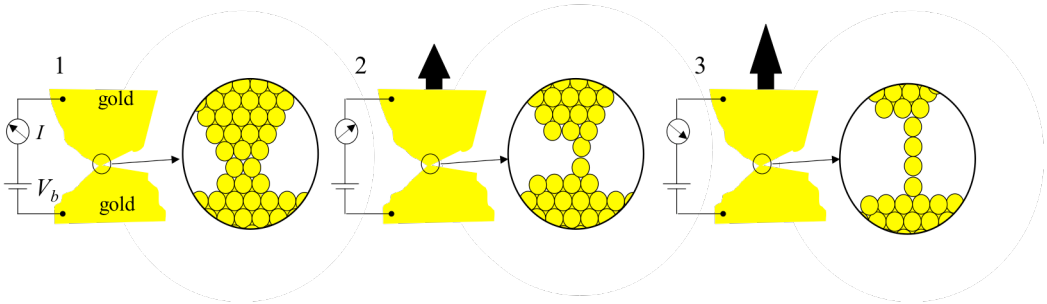

Figure 3.1: Cartoon showing the formation of a wire of single gold atoms freely suspended between two macroscopic electrodes. The break-junction technique consists of measuring the conductance, $G=I/V_b$, as a function of the electrodes separation, z.

After some indentations of the tip into the substrate, if the contacting surfaces are clean the two pieces of metal will strongly adhere or *cold weld*. Now if the tip is retracted, the contact will first deform plastically forming neck-shaped wire between the electrodes. During retraction of the tip, the neck becomes thinner until it consists in its final stages of only a few bringing atoms. The simplest way of characterizing the electronic transport properties of atomic-sized contacts is performed by measuring the current flowing through the junction, when a low bias voltage, V_b, is fixed between the tip and the substrate. In the break-junction experiments the conductance of the junction $G=I/V_b$, is recorded as a function of the relative tip-substrate distance z, during successive cycles in which atomic-sized contacts are formed and then broken. Such a graph, representing the evolution of G as a function of z will be called *conductance trace* in the rest of this thesis.

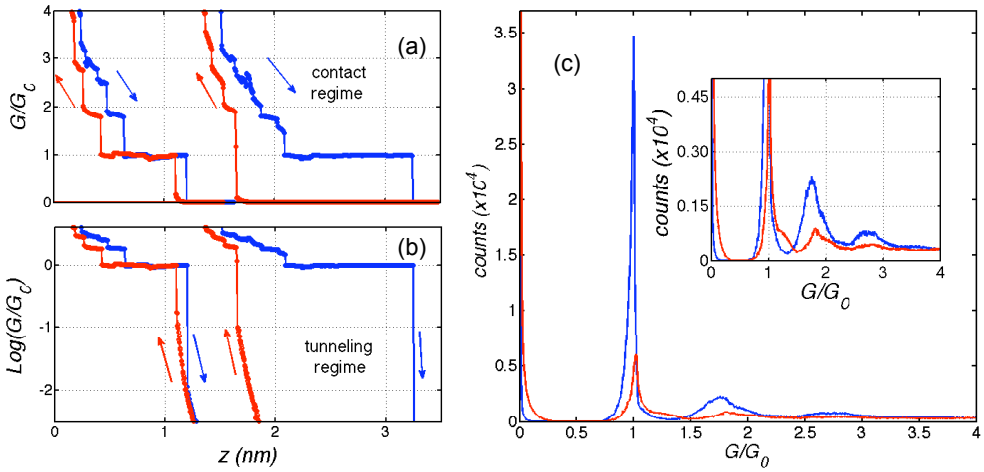

Figure 3.2: Conductance traces of gold at 4.2K in linear scale (a) and in logaritmic scale (b). Conductance histogram of gold contacts built form 5000 traces (c). In blue, it is represented the graphs corresponding to breaking contacts and in red forming contacts.

In Fig. 3.2 (a) and (b) we show two typical conductance traces obtained during the breaking (blue lines) and forming (red lines) process of atomic-sized gold contacts at 4.2 K. In these curves, two clearly different regimes can be observed: the contact regime and the tunneling regime. In the contact regime, the conductance is larger that G_0 and changes in a step-wise fashion. The reduction of the cross-sectional area of the contact produces intervals in which the conductance is relatively constant *plateaus* separated by sudden jumps. The last plateau, just before the contact rupture, is nearly flat and very close to 1 G_0. At this point, it is generally assumed that the narrowest part of the contact will consist of a single gold atom in diameter. After further retraction, the metallic contact finally breaks and the conductance enters the tunneling regime. In the tunneling regime, the conductance is orders of magnitude smaller than in contact regime and it depends exponentially on the relative tip-substrate distance. The cleanliness of the contacting surfaces can be checked from the conductance traces in the tunneling regime. From the theory of quantum tunneling, we know that

$$G \propto e^{-1.025\sqrt{\phi}z} \tag{1}$$

where z is the tip-substrate distance (given in angstroms) and ϕ is the apparent tunneling barrier (in electronvolts). From the slope of $Log(G/G_0)$ versus z, we

obtain an apparent tunneling barrier of ~5 eV. Such a high value of the apparent tunneling barrier is a signature of a clean contact, since the presence of adsorbates lowers the tunneling barrier dramatically.

When atomic-sized contacts are studied by means of the break-junction method, a great variety of behaviours can be observed in the individual conductance traces. The formation and rupture of a contact involves different and uncontrolled atomic rearrangements in the narrowest part of the junction, as a result, each conductance trace is unique and different to the others. A useful tool to determine the average conductance behaviour over a series of atomic-sized contacts, is the conductance histogram [2]. This histogram is obtained by dividing the conductance axes into finite intervals (bins) with size δG. The number of data points that are located at each bin is counted for a large set of conductance traces (typically of the order of thousands). The conductance histogram built from thousands of similarly prepared contacts represents the probability of finding a conductance value during the rupture or formation of contacts. The curves in Fig. 3.2 (c) represent the conductance histograms built from 5000 consecutive conductance traces during the breaking (in blue) and forming (in red) process of gold contacts at 4.2 K. The conductance of a one-atom contact of gold is very well defined and results in a sharp peak at 1 G_0 in the conductance histogram. Experimental [3] and theoretical studies [4, 5] have provided clear evidences that the conductance values close 1 G_0 is the result of a single conductance channel, having a transmission probability close to one. In the histograms we observe that the last plateaus frequently appear near to 3, 2 and 1 G_0. There has been substantial evidence that this is at least partially the result of the conductance quantization [6, 7].

3.2 Atomic gold wires

Electronic transport properties of atomic-sized contacts are exceptional compared to those observed in macroscopic metals. For instance, the last conductance plateau at 1 G_0 of a one-atom contact of gold remains stable to a bias up to 1 V. This voltage leads to enormous current densities of the order of 8×10^{14} A/m^2 flowing through a single atom.

Typically the length of the last plateau before the rupture of a gold contact is shorter than 0.5 nm, however, sometimes it is possible to observe much longer plateaus. Sometimes the conductance traces during the breaking process exhibit last plateaus up to 2.5 nm, note that this length is 9 times the nearest-neighbour spacing of gold atoms in the crystal (2.88 Å). Yanson *et al.* [8] showed that these

Simple model of an atomic wire

exceptionally long last plateaus were actually caused by the formation of stable wires of single gold atoms freely suspended between the electrodes. If a chain of single atoms is indeed formed during the observation of a long plateau, then its length at the breaking point should be close to an integer multiple of the distance between atoms. The distribution of lengths of the last plateau (from G=1.2 G_0 to 0.5 G_0) over a set of conductance traces (typically of the order of tens of thousands) during the breaking process is the so-called plateau length histogram (see the inset of Fig. 3.3). In the case of gold, the plateau length histogram shows a preference for lengths at multiples of 2.5±0.2 Å, suggesting that this distance corresponds to the interatomic spacing of the wire.

The return distance, which is the tip displacement required in order to reform a contact at 1 G_0, is always larger than the plateau length originated by breaking the contact. This effect is understood as the collapse of the atoms of the wire plus a contraction of the electrodes appexes in the rupture, due to the relaxation of the accumulated tensile stress. The number atoms forming the atomic wire can be estimated by dividing the plateau length or the return distance by the interatomic spacing of the wire.

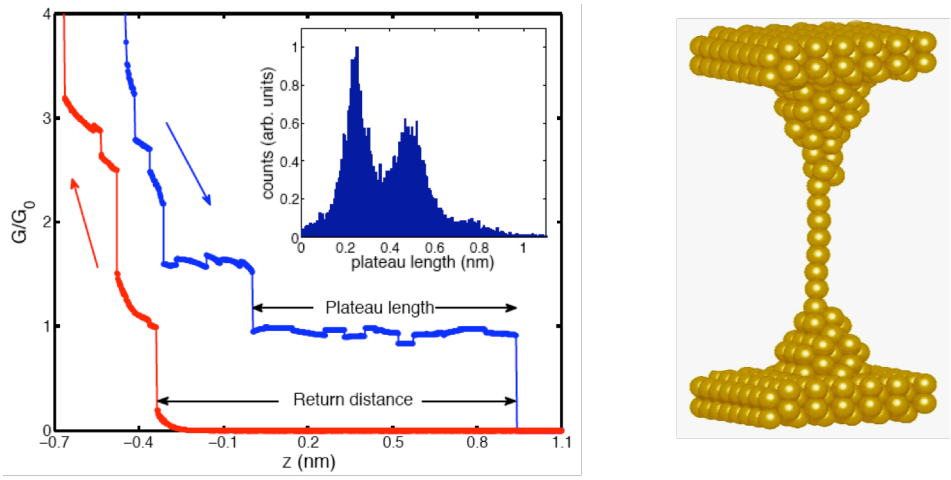

Figure 3.3: A long plateau length at a conductance of 1 G_0 indicates the formation of an atomic wire. (Inset) Plateau length histogram built from 60000 conductance traces breaking gold contacts at 4.2 K. Note, that the peaks appear at multiples of 0.25 nm, suggesting that this distance corresponds to the interatomic spacing of the wire. The atomic wire on the left has been taken from

A different approach to produce and study atomic gold wires is based on the transmission electron microscopy (TEM). In this technique atomic wires are fabricated by perforating holes in a gold thin film using a focused electron beam. Using an instrument that combines a STM with a high-resolution transmission electron microscope (HRTEM), Ohnishi *et al.* [9] were able to visualized the formation of atomic wires of gold atoms between gold electrodes. Such STM-HRTEM combined techniques have been used by several groups [9, 10], tipically the conditions for the experiments are ultra-high vacuum (UHV) and room temperature. Fig. 3.4 it is shown a HRTEM image of a linear chain of four gold atoms (coloured spots) forming a bridge between two gold electrodes (coloured areas). The spacing between gold atoms observed in this experiment ranges from 3.5 to 4.0 Å, which is much larger than the nearest-neighbour spacing in the crystal and the interatomic distance observed by Yanson *et al.* [8]. The large distances between neighboring gold atoms could be explained by the presence of undetected light atoms like S, C, H able to stabilize the atomic wire [11-13], which would be unstable at room temperature. In the Sect. 3.8, we will discuss another possible explanation in which gold wires exhibit an equilibrium zigzag structure.

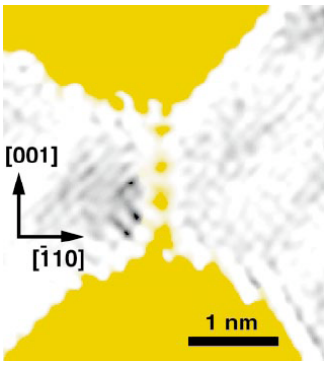

Figure 3.4: HRTEM image of a linear chain of gold atoms forming a bridge between two gold electrodes (coloured areas). The spacing of the four gold atoms ranges from 0.35 to 0.4 nm. Taken from Ref. [16]

An atomic chain of single metal atoms freely suspended between two electrodes is certainly the ultimate one-dimensional metallic wire that you could imagine. These atomic wires are formed during the final stage of the breaking of contacts of certain metals like Au, Pt and Ir [14]. Having a single channel that is almost

fully open, atomic wires of gold are ideal systems for testing predictions and basic concepts of the quantum transport theory.

3.3 Inelastic spectroscopy of atomic wires (PCS)

When a metallic contact shrinks down to dimensions of the same order or smaller than the Fermi wavelength (of the order of few angstroms), the conductance enters the so-called full quantum regime. In this regime, the wave functions of electrons are very sensitive to the local atomic arrangement. As a result, electronic and mechanical properties are strongly coupled in these systems. The electron transport of atomic-sized contacts can be described by the theory of ballistic transport, where the electrons travel through quantum channels across the contact without losing phase coherence or suffering inelastic scattering events. However, a small but significant amount of inelastic scattering processes occurs inside and near the contact. The electron-phonon interaction in atomic gold wires has been investigated experimentally by means of point contact spectroscopy (PCS) [15, 16]. This technique is based on the variations in the conductance caused by the excitation of vibration modes or phonons in the wire.

Fig. 3.5 (a) shows a short and a long plateaus at a conductance of 1 G_0, indicating the formation of atomic gold wires of ~0.4 and ~2.2 nm long, respectively. The probability of forming these atomic wires decreases rapidly with the length, being less than 10^{-4} for plateaus longer than 2 nm. Atomic-sized contacts are very stable at low temperatures and the conductance of a given contact remains stable as long as the tip position is not changed. The differential conductance of the wires $G=dI/dV$ as a function of the bias voltage is measured using a lock-in amplifier, with a small modulation of 1 mV. The derivative of the differential conductance $1/G_0\ dG/dV$, the so-called point-contact (PC) spectra, is calculated numerically. The differential conductance curves and the PC spectra of atomic wires of different lengths (from one to seven atoms) are shown in Fig. 3.5 (b)-(d). Fig. 3.5 (b) and (c) show two different situations during the elongation of a short wire (one or two atoms long), positions labeled *S* and *M* in Fig 5.3 (a) respectively. Fig. 3.5 (d) corresponds to a long wire (about seven atoms long). The differential conductance of atomic wires of gold is close to unity at low voltages and drops symmetrically above a certain threshold voltage in the range of 10-20 mV. The symmetric drops in the dI/dV are observed as antisymmetric peaks in the PC spectra. The change in the dI/dV, whose magnitude is about 1-2%, is originated by the onset of the excitation of a

longitudinal phonon mode of the wire, with neighbouring atoms moving in antiphase. As we will discuss in Sect. 3.4, such mode has the highest frequency and contributes to the inelastic current. For voltages bellow a certain threshold $V_{ph} = \hbar\omega / e$, the electrons cannot lose energy through inelastic interactions with atoms. Only for voltages above V_{ph}, the electrons can give part of their kinetic energy to the atoms, which start to vibrate. The onset of the inelastic processes change the transmission of the wire, as a result, a sudden drop is observed in the differential conductance at the energy in which phonons can be excited.

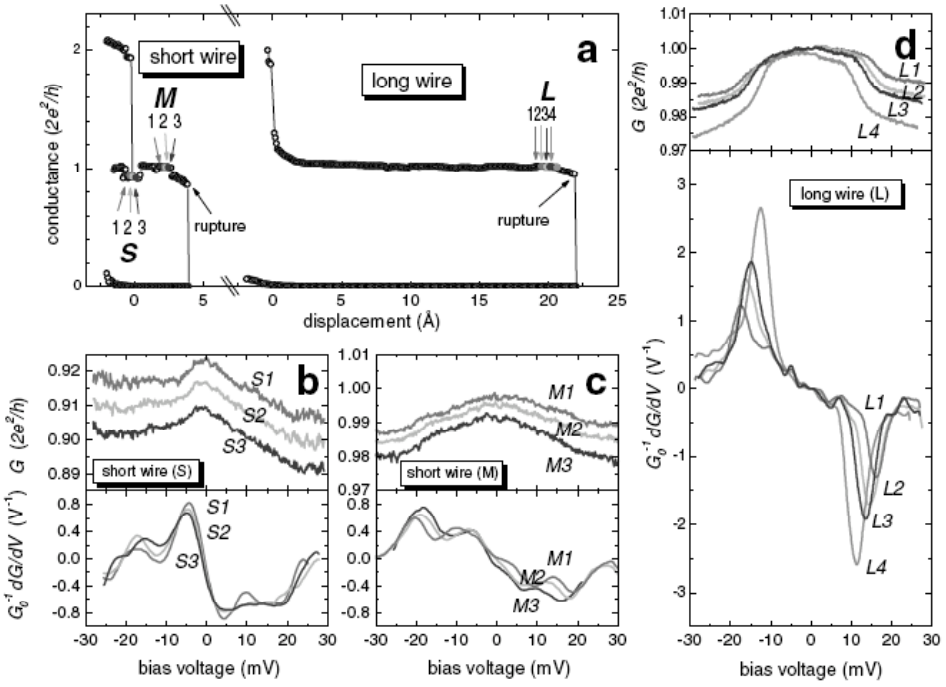

Figure 3.5: Point contact spectroscopy of atomic gold wires at 4.2 K. (a) Short and long plateaus corresponding to atomic wires of ~0.4 and ~2.2 nm long, respectively. Panels (b), (c) and (d) show the differential conductance and the PC spectra at points S, M and L, respectively, marked by arrows. The various curves in (b), (c) and (d) were acquired at different situations during the elongation of the wire. Taken from Ref. [18].

Experimentally, it is observed [15, 16] that the position and amplitude of the peak in the PC spectra of a given atomic wire are very sensitive to its state of strain. As shown in Fig. 3.5 (d), stretching the atomic wire results in a shift of the

peak position to lower voltages and an increase in the emission probability. The shift in the energy is expected for this longitudinal mode, since stretching of the wire reduces the bond strength and therewith the effective spring constant for the harmonic oscillators [15]. The increase in the emission probability indicates an enhancement of the electron-phonon interaction due to the larger corrugation of the atomic potential seen by the electrons. In Fig. 3.6 (a) and (b) we have plotted the position of the peak and its amplitude for many different atomic wires of different length.

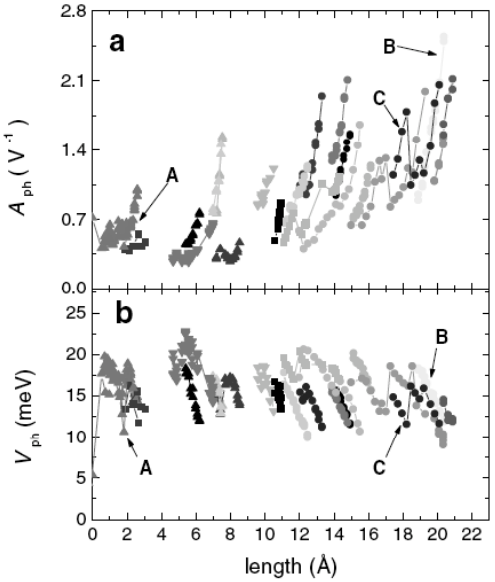

Figure 3.6: (a) Peak position V_p and (b) amplitude A_p in the IES spectra as a function of the length L for different atomic wires. Different color represents a different wire. Taken from Ref. [18].

3.4 Simple model of an atomic wire

It is remarkable that only one phonon mode have a non-zero coupling to the ballistic electrons in an atomic wire of gold. This can be understood in terms of simple 1-D models. Consider an infinite chain of single atoms, where the interaction between the nearest neighbour atoms is represented by a spring constant *K*. The equation of motion is given by,

$$M\ddot{x}_j = -K(x_j - x_{j-1}) + K(x_{j+1} - x_j) \qquad (2)$$

where *M* is the mass of an atom. We expect a solution in the form

$$x_j = Ae^{i(jqa+\omega t)} \quad \text{and} \quad x_{j\pm1} = Ae^{i(jqa+\omega t \pm qa)} \tag{3}$$

where a is the spacing between atoms and q is the wavevector.

By substituting (3) in (2), we easily obtain the dispersion relation,

$$\omega = 2\sqrt{\frac{K}{M}}\left|\sin(qa/2)\right| \tag{4}$$

The first Brillouin zone lies in the interval $-\pi/a<q<\pi/a$.

As we have discussed (Appx. A), an atomic wire with one electron per atom can be modelled by a tight-binding Hamiltonian and the band structure is given by (Eq. A.3)

$$E = \varepsilon_0 - 2t\cos(ka) \tag{5}$$

where ε_0, is energy per site and t, is the hopping between nearest neighbours.

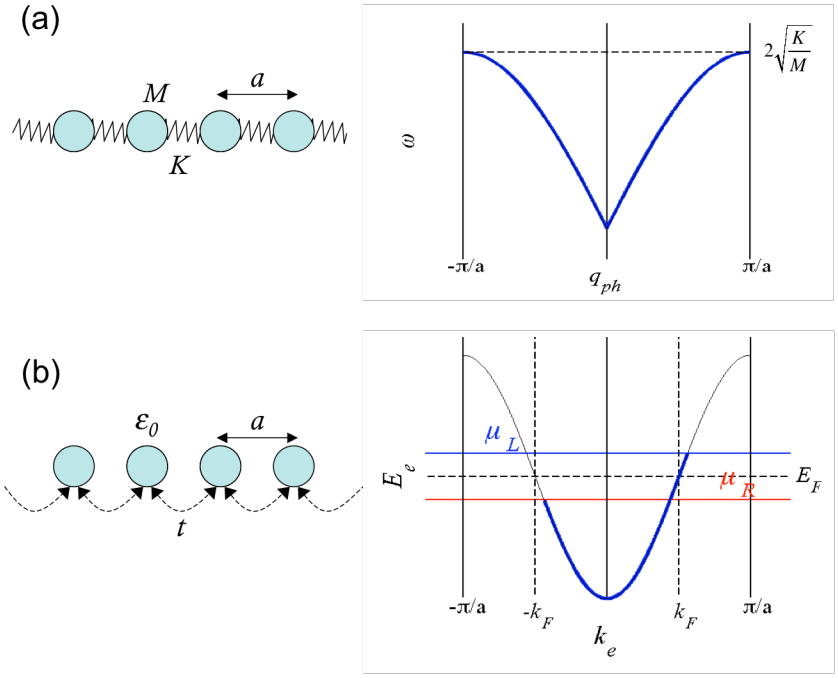

Figure 3.10: (a) Mechanical model of an atomic wire. M is the mass of the atoms and a is the interatomic distance. The interaction between first neighbor is modelled by a spring of stiffness K. (b) In the electrical model, ε_0 is the enegy per site and t is the hopping between nearest neighbours. The kinetic energy of phonons is several orders of magnitude smaller than the energy of electrons at E_F.

Time-dependent potential in 1D

Since each electron has two spin states, for every k state in the band there will be two electrons. In the case of atomic wires with one conduction electron per atom (monovalent atoms), the band is half filled and the Fermi vector k_F lies at $\pm\pi/2a$.

In Fig. 3.10 (a) and (b) we show the dispersion relation, $\omega(q)$ and the band structure, $E(k)$ for an infinite monoatomic wire. It is important to remark that the kinetic energy of phonons is several orders of magnitude smaller than the energy of electrons at the Fermi level (E_e~1 eV and E_{ph}~10 meV). As we can observe in Fig. 3.10 (b), the right-moving states are occupied up to μ_L, when one of these electrons suffers an inelastic scattering event, due to the Pauli exclusion principle, the electron has to scatter to an unoccupied left-moving state, and the change in momentum is $2k_F$. This backscattering process, i.e. the transition from a right-moving state to a left-moving one or vice versa, causes a small decrease of the total conductance of the atomic chain. By other hand, the conservation of momentum implies that these electrons can only interact with a phonon of wave vector $q_{ph}=2k_F=\pi/a$. This vibrational mode with a wavelength $\lambda_{ph}=2a$, corresponds to a displacement of contiguous atoms in antiphase.

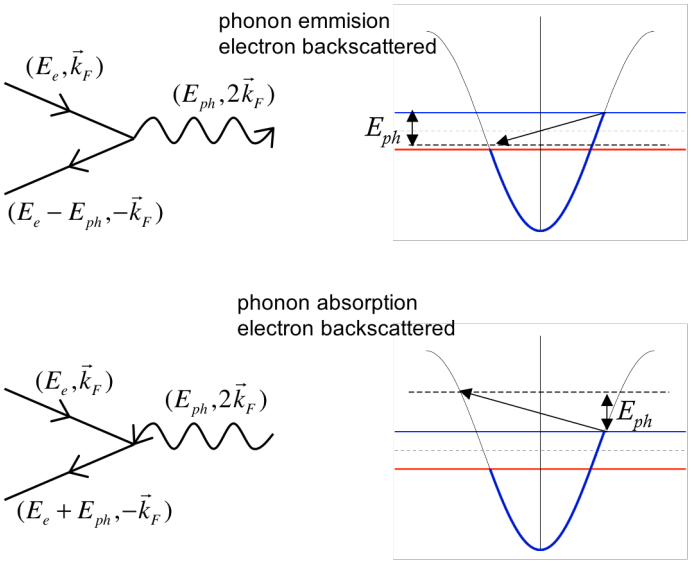

Figure 3.11: Diagram of the possible electron-phonon interactions (not to a scale) in a half-filled band. The absorption or emission of a phonon with $q_{ph}=2k_F$ implies a backscattering of the incident electrons.

Therefore, these inelastic scattering events cause a net reduction of the conductance, but only when the transmission of the channel is close to one. As we will see (Chap. 5) in molecular junctions $T \ll 1$ and the right-moving states are largely empty. This results in an increase of the probability of forwards scattering and a net increase of the conductance.

3.5 Mechanical properties of atomic wires

The mechanical properties of matter are qualitatively different at the nanoscale than at larger dimensions. Understanding how these properties change when the dimensions of a sample are reduced down to the atomic-scale, is an interesting question not only from a fundamental point of view, it also has many implications in technological problems related with adhesion, wear, friction and fracture at the nanoscale.

Forces and conductance, during the evolution of a atomic-sized gold contact, can be measured simultaneously [17, 18] by using two STM mounted in series as shown in Fig. 3.7. Here, the sample is a cantilever fixed by one end, which consists of a cylindrical gold wire (>99.99% purity) of 0.125 mm in diameter and 1.8-2.2 mm in length. The bottom STM is used in order to form and break contacts at the free end of the cantilever. The force applied during the fabrication and breaking of a junction is obtained by measuring the cantilever deflections using an auxiliary STM. The auxiliar STM works in constant current mode, following the force induced displacements of the cantilever free end with picometer resolution. In order to avoid mechanical instabilities related with the softness of the force sensor, the cantilever has a spring constant (100-200 N/m) two orders of magnitude higher than the effective elastic constant expected for atomic contacts. The stiffness of the force sensor should be calibrated[(3)] before to start these measurements.

(3) The calibration of the wire stiffness can be done by measuring its vibrational frequency and its deflection as a function of force for large forces.

Time-dependent potential in 1D

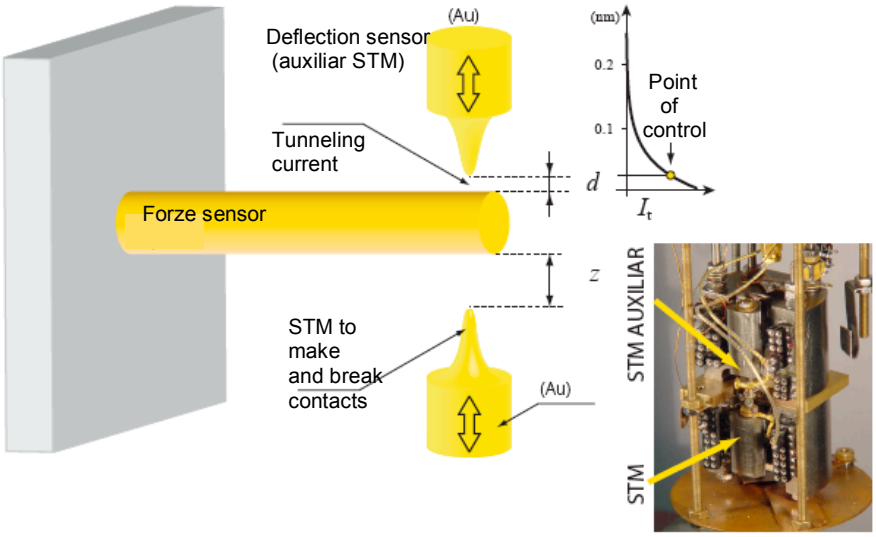

Figure 3.7: Experimental setup used for measuring simultaneously the conductance and forces in atomic-sized gold contacts. Adapted from PhD. thesis JJ. Riquelme.

Let us follow the conductance and force evolution of a gold contact as showed in Fig. 3.8. Consider the zero of the horizontal axis as the starting point. At this point the contact consists of several atoms in section. In order to elongate a metallic contact it is necessary to exert a tensile force, which will be considered negative in our graphs. In response to this force the contact deforms elastically accumulating stress. The effective stiffness, K_{eff}, of the contact produces a negative slope in the force versus the electrodes separation. The stress accumulated in the junction leads to spontaneous atomic rearrangements in which the force is relaxed and the contact adopts a longer stable configuration. Alternating elastic deformations and sudden force relaxations, the cross section of the contact is reduced down to one-atom contact.

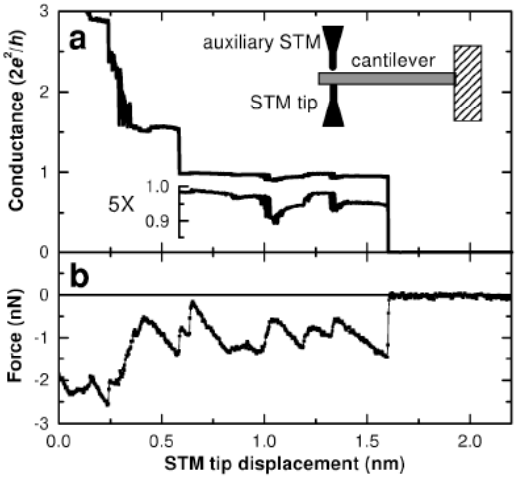

Figure 3.8: Simultaneous measurement of forces (b) and conductance (a) in an atomic chain of gold. Notice the correlation between the sawtooth behaviour of the force and the stepwise evolution of the conductance: the sudden force relaxations lead to the abrupt changes in conductance. Taken from Ref. [21].

When the conductance is close to 1 G_0, the neck of the contact will consist of a single gold atom. At this point, the conductance changes only a fraction G_0 while the force shows the same sawtooth behaviour observed for bigger contacts. If an atomic gold wire is formed, the atomic rearrangements during the stretching do not occur in the wire itself but in the bases of the wire. As long as the force required to incorporate atoms, from the electrodes to the wire, is smaller than the breaking force, the atomic chain will grow in length. Rubio *et al.* [18] showed that the average breaking force of atomic gold wires is 1.5±0.3 nN and does not dependent of the length of the wire. This force is considerably larger than the force required to break individual bonds in bulk gold, which is estimated at 0.8-0.9 nN. This is direct experimental evidence that bonds of low coordinated gold atoms are considerably stronger than bonds in macroscopic wires.

Time-dependent potential in 1D

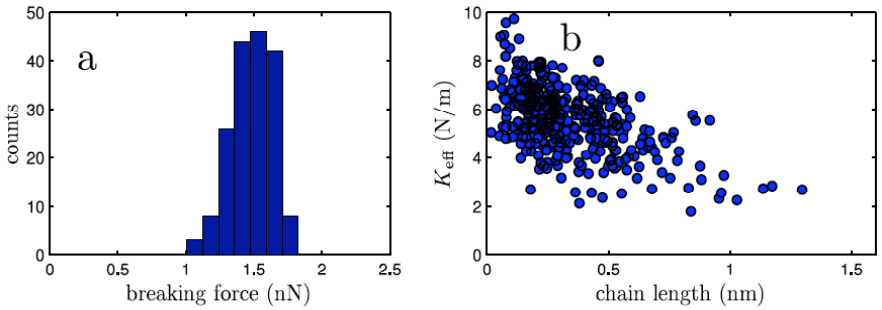

Figure 3.9: (a) Breaking force histogram from a set of 200 atomic gold wires (b) Effective stiffness, K_{eff}, measured in the last elastic deformation stage, just before chain rupture, as a function of the length of the chain. Adapted from Ref. [21].

3.6 Exploring the mechanical properties of atomic bonds

Our setup allows us to perform spectroscopic measurements with a high sensitivity to the local atomic arrangement. As we will show these measurements can be used to obtain information about the structure of atomic gold wires. In Fig. 3.12 we show the dI/dV curves as a function of bias voltage measured at different positions of a plateau near to 1 G_0. The length of this plateau indicates the formation of an atomic gold wire of 5 or 6 atoms. In particular, this plateau presents quite a lot structure (see Fig. 3.12 (a)), which probably is a result of elastic processes due to the disorder at the point where the atoms are being extracted. These measurements have been performed at 0.25 K using a lock-in amplifier with a modulation of 0.7 mV. The lower temperature and modulation produce sharper peaks at the PC spectra than those shown in Fig. 3.5.

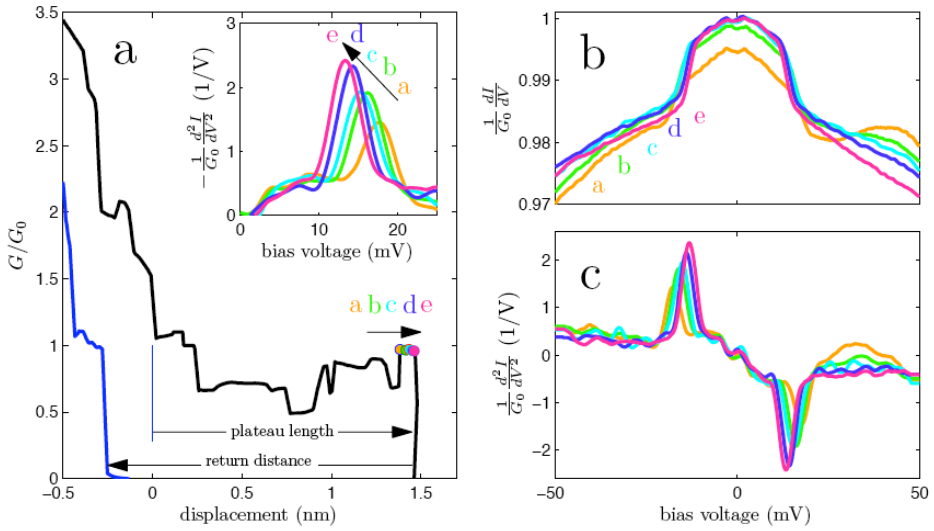

Figure 3.12: Inelastic Electron Scattering in an atomic gold wire at 250 mK. (a) Conductance plateau corresponding to an atomic wire. (b) The differential conductance dI/dV is measured at different points of the conductance plateau by using a lock-in amplifier. (c) Derivative of the differential conductance normalized by G_0 or PCS spectrum.

Theoretically, the stability and structure of atomic wires have been thoroughly studied. One of the main reasons was the abnormally large interatomic distances observed in some of the experiments at room temperature [9]. It has been predicted that an infinite atomic wire of Au would have a preferred zigzag structure, rather than linear.

In Fig. 3.11, we show schematically an atomic gold wire connected between gold electrodes. The atomic wire is represented as a line of balls connected from one to the next by springs of stiffness γ. The electrodes are represented by two springs with stiffnesses K_L and K_R. The total stiffness of the electrodes K_m is computed as the sum in parallel of the stiffness of each electrode.

Time-dependent potential in 1D

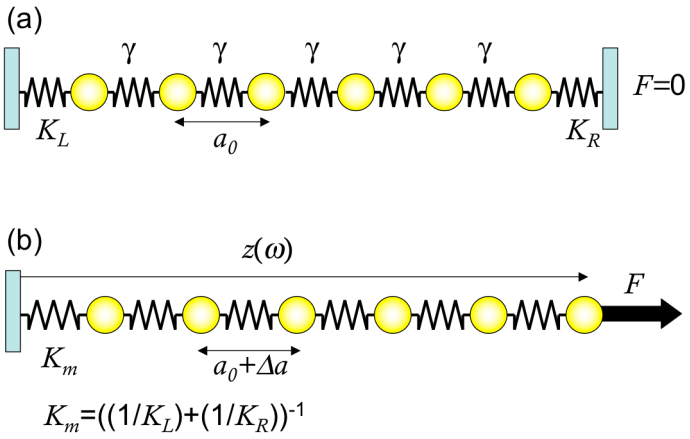

Figure 3.12: Chain of coupled oscillators used to model an atomic gold wire. The total stiffness of the electrodes is computed as the sum in parallel of the stiffness of each electrode.

Within this model the elastic deformation of the wire under tensile stress is given by the deformation of interatomic bonds plus the elastic deformation of the electrodes. Therefore, we can approximate the distance between the electrodes as,

$$z(\omega) = z_0 + n(a_0 + \Delta a) + \Delta z_{elas} \tag{6}$$

where n is the number of interatomic bonds in the wire, a_0 is the equlibrium distance between gold atoms in the wire, Δa is the elastic deformation of one interatomic bond and Δz_{elas} is the elastic deformation due to the electrodes. At a given force F, it is satisfied that

$$F = \gamma \cdot \Delta a = K_m \cdot \Delta z_{elas} \rightarrow \Delta z_{elas} = \frac{\gamma}{K_m} \Delta a \tag{7}$$

Due to the shape of the curves representing the peak position in the PC spectra as a function of z, we have simplified the expresion of Δa by using a second order polynomial function with one degree of freedom α.

$$\Delta a = \alpha \cdot f(\omega) \tag{8}$$

To determine the parameters of the function $f(\omega)$ we have used a set of PC spectra measured in the longest plateau found on the experiment. In the case of long wires, we expect that the elastic deformation of the wire came mainly from the deformation of individual bonds in the wire.
By using the Eq. (7) and (8), the Eq. (6) becomes to

$$z(\omega) = z_0 + n(a_0 + \alpha \cdot f(\omega)) + \frac{\gamma}{K_m}\alpha \cdot f(\omega) \qquad (9)$$

We have used the Eq. (9) in order to determine an expresion for $\Delta a(\omega)$. For that we have used a function for γ/K_m linear with z and, we have found the best values for n and α in order to fit the peak position in the PC spectra with the model.

References

[1] N. Agraït, A.L. Yeyati and J.M. van Ruitenbeek, *"Quantum properties of atomic-sized conductors"*, Phys. Rep. **377** (2003) 81–279.
[2] J.M. Krans, J.M. Van Ruitenbeek, V.V. Fisun, I.K. Yanson and L.J. De Jongh, *"The signature of conductance quantization in metallic point contacts"*, Nature. **375** (1995) 767-769.
[3] G. Rubio-Bollinger, C. de Las Heras, E. Bascones, N. Agrait, F. Guinea and S. Vieira, *"Single-channel transmission in gold one-atom contacts and chains"*, Phys. Rev. B. **67** (2003) 121407.
[4] J.C. Cuevas, A. Levy Yeyati, A. Martin-Rodero, G. Rubio Bollinger, C. Untiedt and N. Agraït, *"Evolution of conducting channels in metallic atomic contacts under elastic deformation"*, Phys. Rev. Lett. **81** (1998) 2990-2993.
[5] J.C. Cuevas, A.L. Yeyati and A. Martin-Rodero, *"Microscopic origin of conducting channels in metallic atomic-size contacts"*, Phys. Rev. Lett. **80** (1998) 1066-1069.
[6] B. Ludoph, M.H. Devoret, D. Esteve, C. Urbina and J.M. Van Ruitenbeek, *"Evidence for saturation of channel transmission from conductance fluctuations in atomic-size point contacts"*, Phys. Rev. Lett. **82** (1999) 1530-1533.
[7] H.E. Van den Brom and J.M. Van Ruitenbeek, *"Quantum suppression of shot noise in atom-size metallic contacts"*, Phys. Rev. Lett. **82** (1999) 1526-1529.
[8] A.I. Yanson, G.R. Bollinger, H.E. van den Brom, N. Agraït and J.M. van Ruitenbeek, *"Formation and manipulation of a metallic wire of single gold atoms"*, Nature. **395** (1998) 783-785.
[9] H. Ohnishi, Y. Kondo and K. Takayanagi, *"Quantized conductance through individual rows of suspended gold atoms"*, Nature. **395** (1998) 780-783.
[10] V. Rodrigues, T. Fuhrer and D. Ugarte, *"Signature of atomic structure in the quantum conductance of gold nanowires"*, Phys. Rev. Lett. **85** (2000) 4124-4127.

[11] H. Hakkinen, R.N. Barnett and U. Landman, *"Gold nanowires and their chemical modifications"*, J. Phys. Chem. B. **103** (1999) 8814-8816.
[12] S.R. Bahn, N. Lopez, J.K. Nørskov and K.W. Jacobsen, *"Adsorption-induced restructuring of gold nanochains"*, Phys. Rev. B. **66** (2002) 81405.
[13] F.D. Novaes, A.J.R. da Silva, E.Z. da Silva and A. Fazzio, *"Effect of impurities in the large Au-Au distances in gold nanowires"*, Phys. Rev. Lett. **90** (2003) 36101.
[14] R.H.M. Smit, C. Untiedt, A.I. Yanson and J.M. Van Ruitenbeek, *"Common origin for surface reconstruction and the formation of chains of metal atoms"*, Phys. Rev. Lett. **87** (2001) 266102.
[15] N. Agraït, C. Untiedt, G. Rubio-Bollinger and S. Vieira, *"Onset of energy dissipation in ballistic atomic wires"*, Phys. Rev. Lett. **88** (2002) 216803.
[16] N. Agraït, C. Untiedt, G. Rubio-Bollinger and S. Vieira, *"Electron transport and phonons in atomic wires"*, Chemical Physics. **281** (2002) 231-234.
[17] G. Rubio, N. Agrait and S. Vieira, *"Atomic-sized metallic contacts: mechanical properties and electronic transport"*, Phys. Rev. Lett. **76** (1996) 2302-2305.
[18] G. Rubio-Bollinger, S.R. Bahn, N. Agrait, K.W. Jacobsen and S. Vieira, *"Mechanical properties and formation mechanisms of a wire of single gold atoms"*, Phys. Rev. Lett. **87** (2001) 26101.

IV

The influence of anchoring groups in the conductance of alkane-based junctions

By means of the scanning tunneling microscope-based break-junction (STM-BJ) technique, we have measured the conductance for a series of alkane chains attached between gold electrodes via thiol (-SH) or amine ($-NH_2$) anchoring groups. We have performed a statistical analysis for determining the most prevalent conductance and plateau length values during the formation of molecular junctions. In particular, we have observed that the conductance plateaus of alkanedithiol junctions, in contrast to alkanediamines, can be larger than the length of the molecule. It can be explained taking into consideration the differences on the bond strength between anchoring groups and gold atoms. The thiol is stronger than amine group and, causes atomic-scale rearrangements in the apexes of the electrodes.

In this chapter, we report experimental results about the processes that occur during the formation of alkane-based molecular junctions[(1)].

4.1 Towards molecular electronics

The semiconductor-based electronics has seen a remarkable miniaturization trend, driven by many scientific and technological innovations. The miniaturization of electronic devices has inherent advantages such as higher speed, lower cost and greater density. But if this trend is to continue, the size of electronic components will soon need to reach the scale of atoms or molecules.

Molecular electronics is a branch of nanotechnology dealing with the study and application of molecular building blocks for the fabrication of electronic components. This includes both passive (like resistors, capacitors, etc.) and active (transistors, switches, etc.) electronic components. The promising technological applications have attracted increasing attention from many researchers in different fields. Currently, molecular electronics is an interdisciplinary domain that spans physics, chemistry, materials science and

(1) Part of the work described here will be published in the paper: "Influence of anchoring on the mechanical behaviour of alkane molecular break junctions". C.R. Arroyo, M.T. González, E. Leary, A. Castellanos-Gómez, G. Rubio-Bollinger and N. Agrait. In preparation.

sometimes biology. Due to the broad use of the term, molecular electronics can be split into two related but separated subdisciplines: *molecular materials for electronics* utilizes the properties of the molecules to affect the bulk properties of a material, while *molecular scale electronics* focuses on single molecule applications.

It is considered that molecular scale electronics was born in 1974 as a consequence of the pioneering work of Aviram and Ratner [1]. Based on theoretical considerations they proposed a molecular structure that can operate as a nanometer-scale rectifier (diode). This seminal paper suggested that single molecules could perform some functions of electronic devices. The concept of molecular scale electronics presents a possibility for dramatic size reduction in electronics, since individual molecules are hundreds of times smaller than the smallest features conceivably attainable by semiconductor technology. Moreover, individual molecules are made perfectly identical in incomprehensibly huge numbers ~10^{23} in the chemist's laboratory. The reduction in size and the enormity of numbers in manufacture are the fundamental potentials of molecular electronics. Because single molecules constitute the smallest stable structures imaginable, this miniaturization is the ultimate goal for shrinking electrical circuits.

4.2 Experiments on molecular junctions

In recent years a great deal of progress has been made in the development of reliable conductance-measuring techniques. These techniques can be divided into two categories: *molecular film* experiments, which measure groups of several molecules (down to tens of molecules), and *single-molecule* experiments focus on individual molecules.

Molecular film experiments generally consist of the sandwiching of a thin layer of molecules between two electrodes, which are used to measure the conductance through the layer. Two of the most successful implementations of this concept have been the bulk electrode approach and in the use of nanoelectrodes. In the bulk electrode approach, a molecular film is typically immobilized onto one electrode and an upper electrode is brought into contact with it, allowing for a measure of the current flow as a function of the applied bias voltage [2, 3]. The nanoelectrode class of experiments utilizing equipment such as atomic force microscope (AFM) tips [4, 5], nanogaps [6] or small-radius wires [7], are able to perform current versus voltage measurements but on a much smaller number of molecules. Among the problems encountered in these

measurements is the lack of reproducibility from one molecular junction to another and, the difficulty to know the active area of a given molecular junction.

Single molecule junctions are of interest both for improving our fundamental understanding of electrical transport at the nanoscale and, for the development of novel electronic devices. To make reliably metal-molecule-metal junctions, the molecules are functionalized with anchoring groups at both ends, such as thiols (-SH), which bind the molecules to the metal electrodes. Thus, in 1997 Reed *et al.* [8] using the mechanical controlled break junction (MCBJ) technique, reported the first experiment directly-measuring the conductance of a single molecule connected between two gold electrodes through sulfur atoms. The main experimental difficulty of measuring the transport properties of single molecules is to establish the situation where one for sure has only one molecule between the electrodes in a two-terminal configuration.

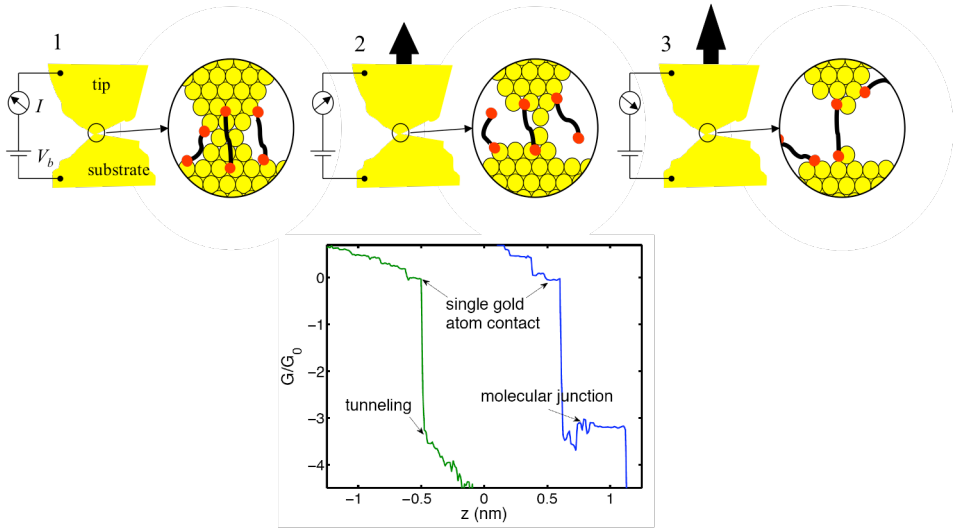

Figure 4.1: Cartoon showin the formation of single molecule junctions.(1) A metallic contact was form with some molecules adsorbed. (2) During the rupture a molecule can be connected to both electrodes. (3) Formation of a single molecule junction. Graph: Conductance traces measured during the breaking process of a gold contact in absence (in green) and in presence (in blue) of molecules terminated with anchoring groups.

The break junction method, using either the STM-BJ or MCBJ (Chap. 2) has been intensively used to study the electrical properties of atomic-sized metal contacts [9]. This methodology was applied in 2003 by Xu and Tao [10] to

measure the conductance of a single molecule connected between to two gold electrodes. To form molecular junctions, atomic-sized gold contacts are broken in a solution containing molecules terminated with anchoring groups. By recording conductance as a function of the relative tip-substrate displacement, some of the conductance traces recorded during the breaking process show new plateaus in the tunneling regime (see graph of Fig. 4.1). These plateaus are due to the formation of stable molecular junctions between the tip and the substrate after the rupture of the metallic contact. The atomic-level geometry of the junction has an effect on the conductance and a statistical approach, such as conductance histograms, is required. The main advantage of this technique is the possibility of adjusting the separation of the metallic electrodes at a precision of fractions of an angstrom. This allows one to stretch the molecular junction up to the breaking point in a very controlled way and, to measure the conductance simultaneously. Forming a junction in which the precise contact geometry is known has been one of the main difficulties with this approach.

In the last years, several experimental groups have begun the study of single molecule junctions connected between two gold electrodes. Due to the simplicity of the experimental setup, some groups have used the approach proposed by Xu and Tao [10]. Statistical studies are based on series of conductance traces measured during the breaking process in the presence of the molecule to be studied. This statistical scheme has been primarily used to determine mean molecular conductance values. More recently, it has also applied to study other features such as the stability time of the molecular junctions [11], the effect of different anchoring groups [12, 13] or the maximum length that the junction can be stretched before the rupture [12].

In the case of simple molecules, in the sense of molecules without specific functionality, such as alkane chains studied here, different studies have shown the variability and complexity of the molecular junction formation [10, 12, 14, 15]. Important factors that have been put forward in order to understand the experimental results refer both, to intrinsic properties of the molecule core, such as flexibility [14] and conformational changes [16] and, to details of the metal-molecule interactions, such as the nature of the bond [17] and different possible binding sites [14].

Although alkane chains have been extensively studied, different aspects of these molecular junctions remain open. Because of the difficulty to obtain a direct visualization of molecular junctions, fundamental questions concerning the junction evolution under stress remain to be answered. A detailed understanding of the anchoring group role during the formation of single molecule junctions has not yet been achieved and it is a current subject of study [13, 17-20].

Characterization of the gold electrodes

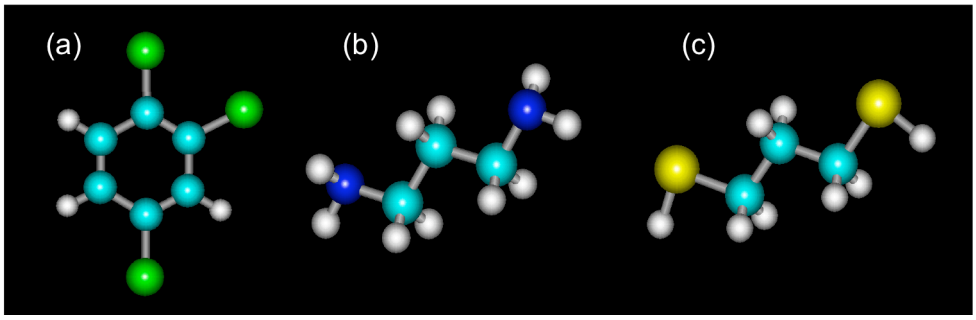

Figure 4.2: Chemical structure of 1,2,4-trichlorobenzene (a)*, organic solvent used in the measurements. Chemical structure of 1,3-propanediamine* (b) *and 1,3-propanedithiol* (c)*, two of the molecules studied in this chapter. The balls represent atoms of hydrogen in white, carbon in cyan, chlorine in green, nitrogen in blue and sulfur in yellow.*

In order to adress these issues, we present a systematic study of the conductance evolution during the breaking process of atomic-sized gold contacts in a solution containing alkanedithiols (HS-$(CH_2)_n$-SH) or alkanediamines (H_2N-$(CH_2)_n$-NH_2) with different lengths of the alkane chain (n=2, 3, 4, 5, 6 and 8). For simplicity, we have denoted the different molecules by using their number of carbon atoms in the alkane chain (for example C5 for pentano). We have studied the conductance of structures that consist of a few molecules, or even a single molecule, wired between two gold electrodes.

4.3 Characterization of the gold electrodes

A detailed investigation of the electron transport processes through molecules requires a realible method to connect metal electrodes to a molecule of interest. As we have commented before, one approach to this problem is based on the use of molecules functionalized with anchoring groups at both ends. These anchoring groups bind to the surface of the metal electrodes. However the establishment of well-defined molecular junctions demands both atomically-sharp and contamination-free electrodes. As we have discussed in Chap. 3, at low temperatures, atomic-sized metal contacts can be easily fabricated without impurities. However, at ambient conditions, the inevitable presence of absorbates and the oxidation of the metal make it difficult to obtain clean metal contacts.

Gold is a special case, because it does not form oxides naturally and, like noble metal does not react with the impurities present in air.

The measurements shown in this chapter were carried out by using a home-build STM (described in Chap. 2) working at ambient conditions. Commercially available gold substrates thermally evaporated on quartz (Arrandee 11×11 mm) were used to prepare the sample. For cleaning the surface of gold, the substrate was immersed for 1-2 minutes in a freshly prepared piranha solution (1:3 H_2O_2 (33%) in H_2SO_4 (98%)). After the piranha treatment, the substrate was rinsed several times with Milli-Q water and dryed in a stream of N_2 gas. Then, the gold surface was flame annealed with a butane burner for 2-3 minutes. This cleaning procedure produces atomically flat Au(111) terraces without organic residues and ready to use. The tip consisted of a freshly cut gold wire (99.99% purity) of approximately 1-1.5 mm in length and 0.250 mm in diameter.

The bias voltage between the tip and the substrate was fixed at low values, 25 mV for all the molecules except for octanodiamine where it was 60 mV. As we have explained before, conductance traces are obtained by measuring the junction conductance $G=I/V$, as a function of the relative tip-substrate displacement z. As usual the conductance will be expressed in units of the conductance quantum $G_0=2e^2/h$, where e is the electron charge and h is the Planck's constant. Gold nanocontacts up to ~10 G_0 in conductance are formed and subsequently broken by moving the STM-tip towards and away from a spot of the surface substrate at approximately 16 nm/s. The indentation and retraction of the tip into the substrate is automatically repeated therefore, the formation and rupture of contacts can be reproduced with great reability. We have observed that the speed of the tip displacements and the indentation depth of the tip into the substrate are important factors in order to remove a substantially higher number of absorbates. For measuring continuously several orders of magnitude in conductance, we have built a linear current-to-voltage converter with two amplifier stages (Sect. 2.6).

Conductance histograms

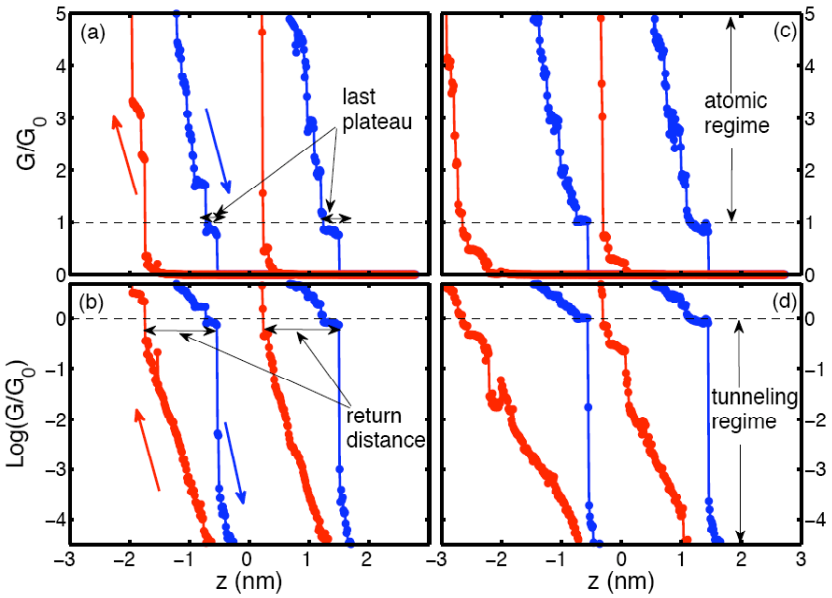

Figure 4.3: Conductance traces measured during the breaking (blue curves) and reforming (red curves) process of atomic-sized gold contacts in ambient conditions, in linear (a) and logarithmic scale (b) and in presence of 1,2,4-Trichlorobenzene, in linear (c) and logarithmic scale (d).

Fig. 4.3 shows two typical conductance traces measured during the formation (red curves) and rupture (blue curves) of atomic-sized gold contacts in ambient conditions Fig. 4.3 (a), and in presence of 1,2,4-Trichlorobenzene (Sigma-Aldrich) Fig. 4.3 (c). We also show the conductance traces in logarithmic scale along the conductance axis Fig. 4.3 (b) and (d) respectively. The atomic diffusion, thermally activated at room temperature, produces conductance plateaus not as well defined as at low temperatures. In most of the conductance traces during the breaking process, a flat plateau corresponding to a one-atom contact of gold [9] appears at 1 G_0. Below 1 G_0 the metallic contact is broken that is manifested as an abrupt jump in the conductance. Typically, this jump is much larger than the observed at low temperatures (see Fig. 3.2), indicating atomic rearrangements in the inmediate proximity of the junctions at the breaking point. At lower values the conductance decreases exponentially as a function of the electrodes separation. The conductance traces during the breaking process show an apparent tunneling barrier typically of ~1 eV, much lower than at low

temperatures ~5 eV. Moreover, in ambient conditions, it is not uncommon to see some conductance traces with small plateaus at low conductances due to the presence of adsorbates in the junctions.

A notable difference respect to low temperatures is that the conductance traces breaking and forming contacts are quite different from each other. The conductance traces forming contacts present much more structure in the tunneling region. This structure indicates the presence of molecules, probably water and some others dissolved in water, which hinder the tip movement approaching to the surface substrate. Another important difference is the length of the last plateau located around 1 G_0, at ambient conditions this plateau is not longer than 0.5 nm. It indicates that with our speed of tip displacements the formation of atomic chains is unstable.

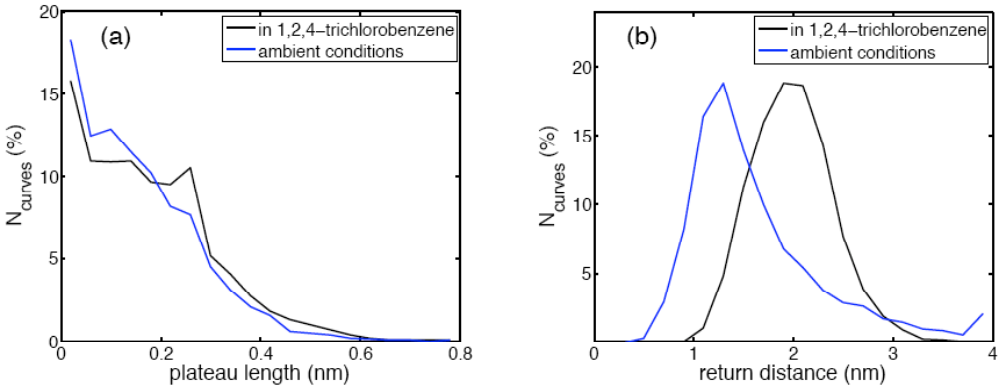

Figure 4.4: (a) Plateau length histogram (from Log(G/G₀)=0.08 to -0.5) built form 5000 conductance traces breaking gold contacts in presence of 1,2,4-trichlorobenzene and in ambient conditions. (b) Distribution return distance (from Log(G/G₀)=0.08 to -0.5) built from 5000 conductance traces breaking and forming gold contacts in presence of 1,2,4-trichlorobenzene and in ambient conditions.

Fig. 4.4 (a) shows the plateau length histogram, built from 5000 conductance traces breaking gold contacts in pure 1,2,4-Trichlorobenzene and in ambient conditions. These histograms have been computed taken the lengths of the conductance traces from $Log(G/G_0)$=0.08 to -0.5 (1.2 to 0.3 G_0). In contrast to the plateau length histogram at low temperatures (inset of Fig. 3.3), we observe that not all the conductance traces show a plateau at 1 G_0. Some break the metallic contact from higher conductance values. Most of the plateaus have a length of 0.25 nm, a distance corresponding to the interatomic spacing in gold wires (Sect.

3.2). The plateau length histogram has a similar profile in presence of 1,2,4-Trichlorobenzene than in ambient conditions. In Fig. 4.4 (b) we show the distribution of return distances, from $Log(G/G_0)$=-0.5 at the rupture to $Log(G/G_0)$=0.08 at the formation of the contact. We can observe that the return distance in average is larger in presence of 1,2,4-Trichlorobenzene than in ambient conditions. This difference can be attributed to the presence of 1,2,4-Trichlorobenzene molecules between the electrodes during the closing of the junction.

4.4 Conductance histograms

The conductance histograms have been widely used to investigate atomic-sized metal contacts as well as molecular junctions. The peaks at the histograms indicate the most probable conductance values during the formation or rupture of contacts (Sect. 3.1).

In general, the conductance of molecular junctions depends not only on the chemical nature of the molecule used, but also on its conformation. The plateaus due to molecular junctions formation observed in presence of alkanedithiol or alkanediamine solutions show variations in conductance, typically of one order of magnitude. In order to investigate these molecular junctions, conductance histograms similar to those proposed by Gonzalez *et al.* [21] are used. The histograms have been computed from conductance traces in logarithmic scale along the conductance axis and, by using a constant bin width Γ equal to 0.035. Hereafter *Log* denotes the common logarithm whereas *Ln* denotes the natural logarithm. We have normalized the number of counts per bin multiplying it by $\delta z Ln(10)/\Gamma N$. Where, δz denotes the minimum vertical displacement of the STM-tip in which the conductance is measured (1.3×10^{-11} m for our setup) and N is the number of conductance traces which are used to build the histogram. For monotonically decreasing conductance traces, it is easy to see that the contribution of each trace to the bin centered at $Log(G_i/G_0)$ is given by,

$$N_i = -\frac{\Gamma}{\delta z \cdot Ln(10)}\left(\frac{dz}{dLog(G/G_0)}\right)_{G=G_i} \quad (1)$$

Therefore, by using the normalization proposed, the conductance histogram provides an average of $-dz/dLog(G/G_0)$ with units of length, N_{norm}(nm).

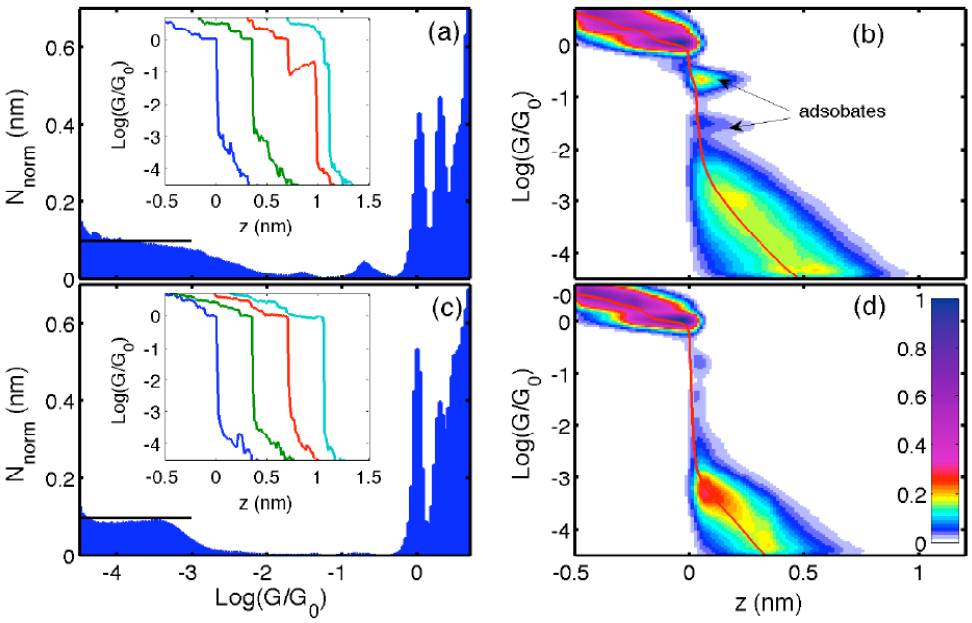

Figure 4.5: Conductance histogram normalized built from 5000 conductance traces during the breaking process of gold contacts (a) in ambient conditions and (c) in presence of 1,2,4-Trichlorobenzene. Trace histogram built from 5000 traces breaking gold contacts (b) in ambient conditions and (d) in presence of 1,2,4-Trichlorobenzene.

In Fig. 4.5 we show the normalized conductance histograms built from 5000 conductance traces measured at ambient conditions (a) and in pure 1,2,4-Trichlorobenzene (c). As it can be observed in the insets of Fig. 4.5 (a) and (c), the plateau lengths at integer multiples G_0 as well as the jump in the conductance at the breaking point vary from junction to junction, probably due to differences in the atomic arrangement. The conductance histograms with this normalization are particulary useful to observe changes in the tunneling regime. The average tunneling barrier height can be calculated from the histograms by

$$\phi = \left(\frac{1}{10.25 \cdot N_{norm}(nm)} \right)^2 \qquad (2)$$

From the histograms obtained under ambient conditions and in presence of 1,2,4-Trichlorobenzene we obtain (black lines) an apparent barrier height typically of ~1 eV. The peaks in the histograms at $Log(G/G_0)$~0.7 and ~1.5 are

observed more frequently at ambient conditions than in presence of 1,2,4-Trichlorobenzene. These peaks can be due to the presence of junctions with absorbates or water molecules. Except the higher presence of absorbates and the variations due to different atomic arrangements, the profiles of the two histograms showed in Fig. 4.5 are quite similar. It indicates that the solvent does not have a great influence during the breaking process. By using the same set of conductance traces, we have computed the 2-D trace histograms [22] at ambient conditions Fig. 4.5 (b) and in pure 1,2,4-Trichlorobenzene Fig. 4.5 (d). The trace histogram has been built by fixing the origin of z coordinates of individual traces at $Log(G/G_0)$=-0.5. We have used a bin with equal to 0.041 in the conductance axis (or 24 bins per decade) and 0.013 in the displacements axis (or 75 bins per nm). The solid line in the trace histogram represents the average of $Log(G/G_0)$ as a function of z, obtained by numerical integration of the normalized histograms,

$$-\int\left(\frac{dz}{dLog(G/G_0)}\right)dLog(G/G_0) = z(Log(G/G_0)) \quad (3)$$

Before introducing the molecules, we have first checked the shape of the histograms computed from thousands of conductance traces measured at ambient conditions. If the histograms have the usual profile we deposit with a pipette 2 μl of 1,2,4-Trichlorobenzene on the surface substrate. The low volatility of 1,2,4-Trichlorobenzene under ambient conditions allows us to perform measurements for a long time by using a small liquid volume. To exclude additional sources of contamination, we have not used a liquid cell but the small volumes used prevent the overflow of the solution out of the surface substrate. If the histograms in the solvent also have the typical profile we add a new droplet of 2 μl with molecules dissolved in 1,2,4-Trichlorobenzene. In these measurements the concentration of molecules in 1,2,4-Trichlorobenzene was 1 mM.

Fig. 4.6 shows the change observed on the conductance traces after addition of a 1 mM solution of pentanodithiol. Each curve in the vertical axis represents the conductance histogram (not normalized) of a single trace using a bin width equal to 0.035. The graph has been obtained from 1500 conductance traces measured continuously. As we can observe few seconds after the introduction of the pentanedithiol solution new structure appears at low conductances.

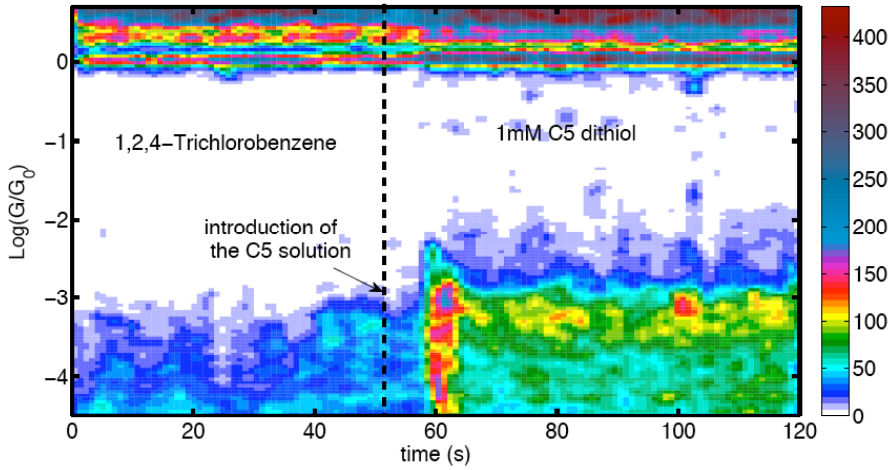

Figure 4.6: Evolution of individual conductance traces during the introduction of a 1 mM solution of pentanedithiol in 1,2,4-Trichlorobenzene.

The conductance histograms built from 5000 unselected conductance traces measured during the breaking of atomic-sized gold contacts in solutions containing alkanedithiols or alkanediamines of different lengths are shown in Fig. 4.7. The profile of conductance histograms depends on how the molecular junction is formed and varies with the nature of the studied molecule. As we observe the histograms in presence of molecules terminated with anchoring groups show a characteristic peak. This peaks is shifted to lower conductance values as the length of the alkane chain is increased. Fitting the most characteristic peak to a gaussian or a lorentzian, one can extract the most probable conductance value for each molecule, as well as the dispersion of the distribution. These are reliable values that can be used to characterized and compare a large number of molecular junctions (see Fig. 4.15). Already the peak of C2-dithiol in these measurements cannot be resolved due to the background that appears in the histograms corresponding to alkanedithiols.

Conductance histograms

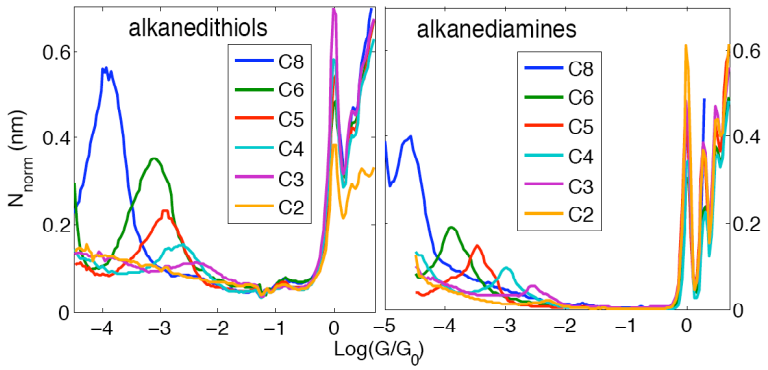

Figure 4.7: Conductance histograms built from 5000 conductance traces during the breaking process in presence of alkanedithiols (a) and alkanediamines (b) solutions. The concentration of molecules was 1 mM and the applied bias voltage was 25 mV, except than octanodiamines where it was 60 mV.

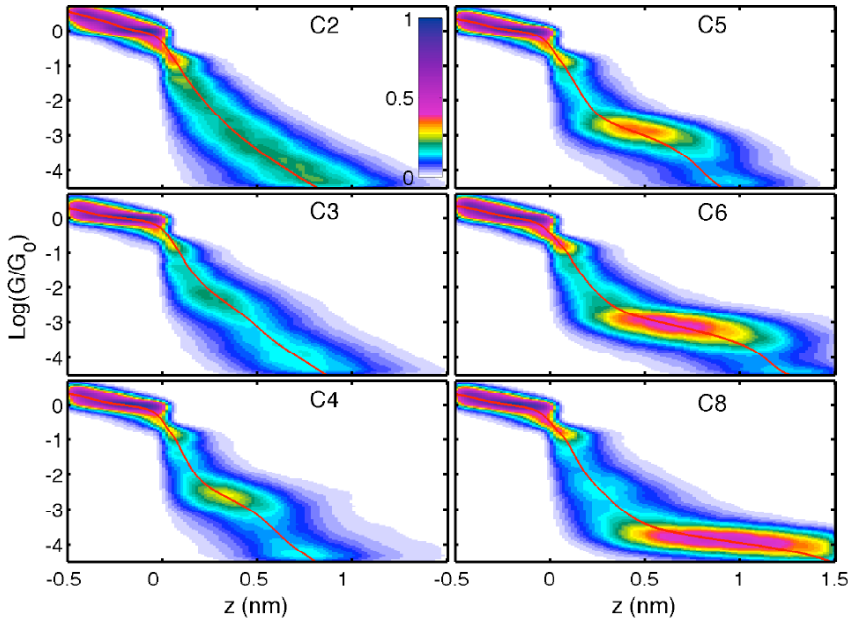

Figure 4.8: Trace histograms built from 5000 unselected conductance traces measured during breaking process of gold contacts in presence of alkanedithiols of different lengths. The concentration of molecules was 1 mM and the applied bias voltage 25 mV.

In Fig. 4.8 and Fig. 4.9, we show the trace histograms corresponding to the same sets of conductance traces used to compute the histograms showed in Fig. 4.7. In this representation, we can observe that longest molecules produce longest plateaus and a larger percentage of traces with plateaus. During the stretching of a molecular junction, longest molecules have more possibilities to keep connected between the electrodes, changing its conformation or binding site, while shorter molecules break more easily the junction.

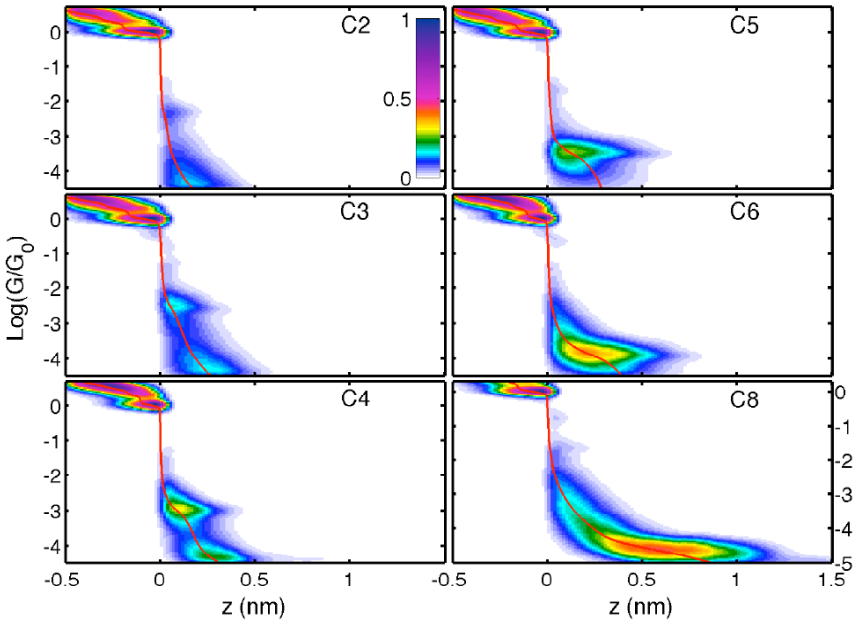

Figure 4.9: Trace histograms built from 5000 unselected conductance traces measured during the breaking process of gold contacts in presence of alkanediamines of different lengths. The concentration of molecules was 1 mM and the applied bias voltage 25 mV, except than octanodiamines where the bias was 60 mV.

A simple inspection of the histograms (Fig. 4.7) and the trace histograms (Fig. 4.8 and 4.9) shows important differences between alkanedithiols and alkanediamines:

- The conductance is higher for dithiols than diamines with the same number of methylene groups.
- The lengths of the conductance plateaus are longer for dithiols than diamines.

- The jump in the conductance after the rupture of one-atom gold contact is more abrupt for diamines than dithiols. The dithiols show much more structure with small conductance plateaus between 1 G_0 and the plateaus due to the molecular junctions formation.

4.5 Trace selection

The plateaus at low conductances correspond to mechanically stable configurations formed during the breaking process and, represent the fingerprints of the formation of molecular junctions. In general, plateaus due to molecular junctions present fluctuations and breakages, which vary from curve to curve. In addition, it is frequent to observe a single conductance trace with several plateaus at different conductance values. Moreover, the percentage of molecular junction realizations can be very different depending on the concentration of molecules and the chemical structure of the molecule under study. In previous sections we have used sets of conductance traces measured continuously, but it is convenient to separate those traces in which it is very likely that a single molecule has broken the last contact. Different selection criteria have been reported in the literature to separate those traces that present plateaus [14, 23]. However, due to the large variety of profiles that a single conductance trace can show, they usually rely on a strong data processing, and the choice of some subjective criteria.

To separate conductance traces with plateaus, firstly we have computed the conductance histogram (not normalized) of each conductance trace between $Log(G/G_0)$=-0.5 to -4.5, using a bin width equal to 0.020. Then, we have calculated the convolution of the histogram of each conductance trace with a rectangular function of height 1 and width $\Delta Log(G/G_0)$. The result of the convolution, $N/\Delta Log(G/G_0)$, is a continuous function that represents the density of data points in a box of width $\Delta Log(G/G_0)$. We have assigned to each conductance trace a value, N_m, given by the maximum value of $N/\Delta Log(G/G_0)$. In Fig. 4.10 we show the procedure for two conductance traces, one of them shows just tunneling while the other shows several plateaus. In right side of Fig. 4.10 (b) are represented the $N/\Delta Log(G/G_0)$ functions computed by using two different values of $\Delta Log(G/G_0)$. We can observe that larger values of $\Delta Log(G/G_0)$ produce a smothest $N/\Delta Log(G/G_0)$ functions. It is important to note that the value of N_m is increasing when the conductance trace shows many data points accumulated at any conductance interval.

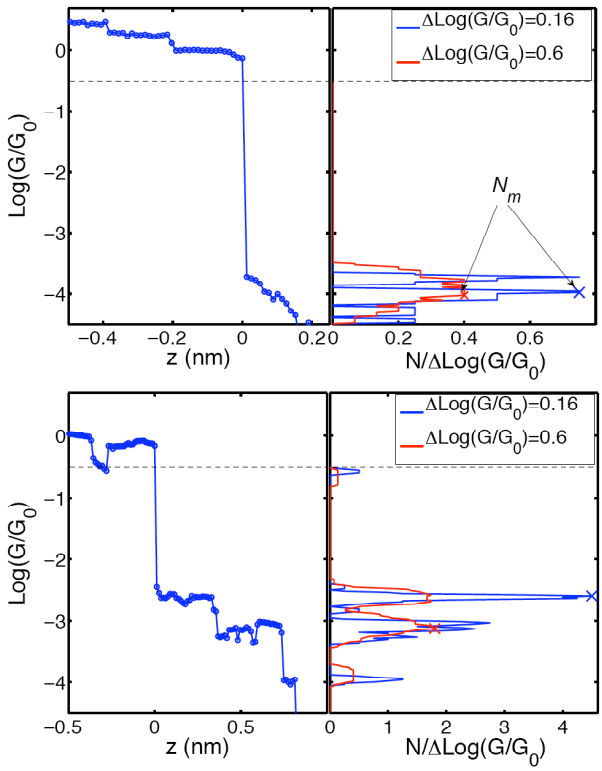

Figure 4.10: Procedure to separate conductance traces with plateaus. Left: Two condutance traces, the first conductance trace corresponds just to tunneling, and the other shows several plateaus. Right: We have computed the convolution function $N/\Delta Log(G/G_0)$ of the histogram of each conductance trace with a unitary step function with two different widths, $\Delta Log(G/G_0)$=0.16 (blue lines) and $\Delta Log(G/G_0)$=0.6 (red lines). We have assigned to each conductance trace a value N_m given for the maximum of $N/\Delta Log(G/G_0)$.

By using this procedure, we have separated our sets of 5000 conductance traces for each molecule, taken into account the density of data points at any conductance interval. Due to the shape of individual conductance traces, the separation has been done by using $\Delta Log(G/G_0)$=0.16. In Fig. 4.11 and 4.12 we have represented the trace histograms for alkanedithiols and alkanediamines built from the 10% of conductance traces highest N_m values.

Trace selection

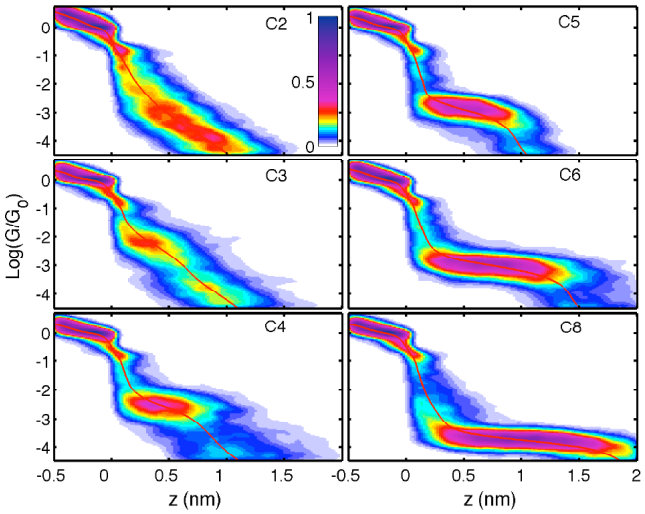

Figure 4.11: Trace histograms for alkanedithiols of different lengths, built from the 10% of conductance traces with highest N_m.

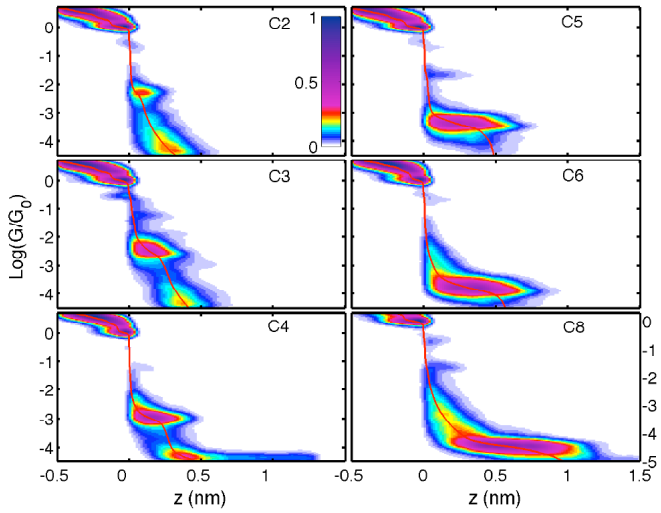

Figure 4.12: Trace histograms for alkanediamines of different lengths, built from the 10% of conductance traces with highest N_m.

In Fig. 4.13 and 4.14 we show the trace histogram for alkanedithiols and alkanediamines of different lengths built from the 10% of conductance traces with smallest N_m.

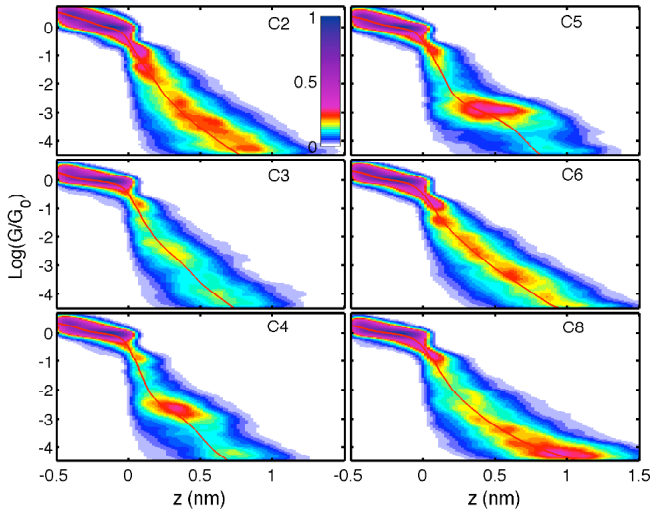

Figure 4.13: Trace histograms for alkanedithiols of different lengths, built from the 10% of conductance traces with smallest N_m.

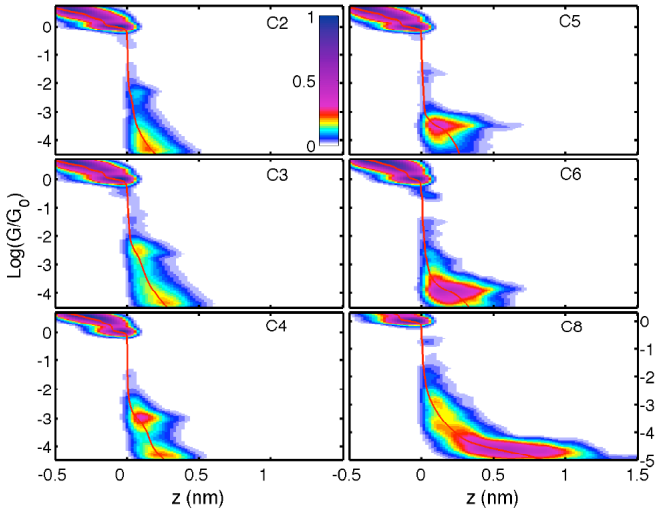

Figure 4.14: Trace histograms for alkanediamines of different lengths, built from the 10% of conductance traces with smallest N_m.

In Fig. 4.15 and 4.16 we compare the $Log(G/G_0)$ as a function of z for alkanedithiols and alkanediamines respectively. These curves has been obtained (Eq. (3)) by integration of the normalized histograms N_{norm}(nm) built from all the

Trace selection

conductance traces (blue lines), the 10% of conductance traces with highest N_m values (red lines) and the 10% of conductance traces with smallest N_m values (black dotted lines). As a reference we have ploted the length of the molecule between anchoring groups (black dahed vertical lines).

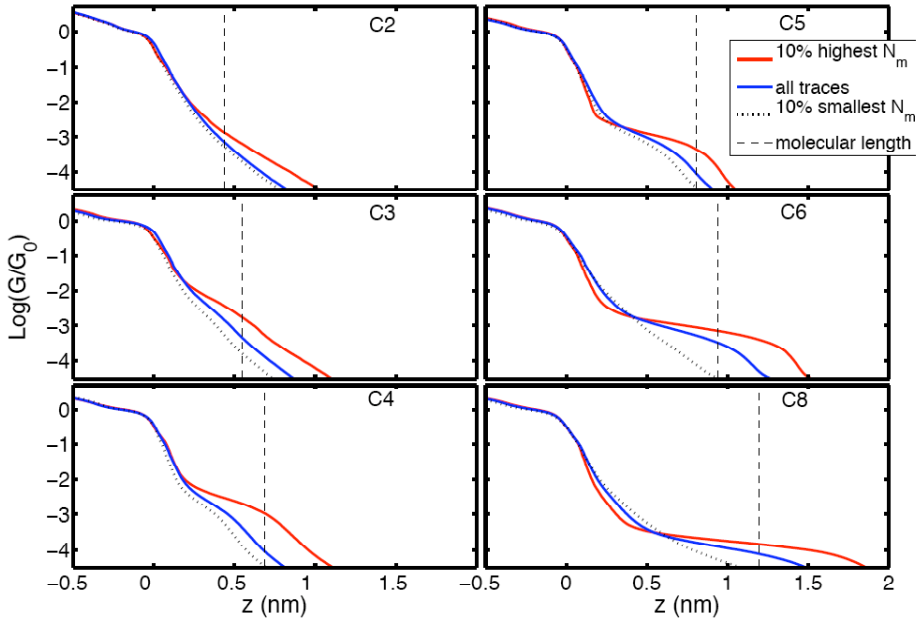

Figure 4.15: Average of Log(G/G_0) as a function of z computed by integration of the normalized conductance histograms built from conductance traces measured in presence of alkanedithiols. The 10% of the conductane traces with longest plateaus (red lines), all the condutance traces (blue lines) and the 10% of the conductane traces with shortest plateaus (dotted lines). The vertical dashed lines represent the length of the molecule between anchoring groups.

As we can observe in Fig. 4.15 and 4.16, the conductance for the longest plateaus (highest values of N_m) is slightly higher than the conductance for all the conductance traces. This suggests that the longest plateaus are indeed formed by molecules well connected between the electrodes. The plateau lengths for alkanedithiols, in contrast to alkanediamines can be larger than the length of the molecule. Moreover, the conductance traces without plateaus (smallest values of N_m) present much more structure in the case of alkanedithiols than for alkanediamines (see Fig. 4.13 and 4.14). These indications strongly suggest atomic-scale deformations and reconstructions of the electrodes appexes while alkanedithiol molecular junctions are being stretched.

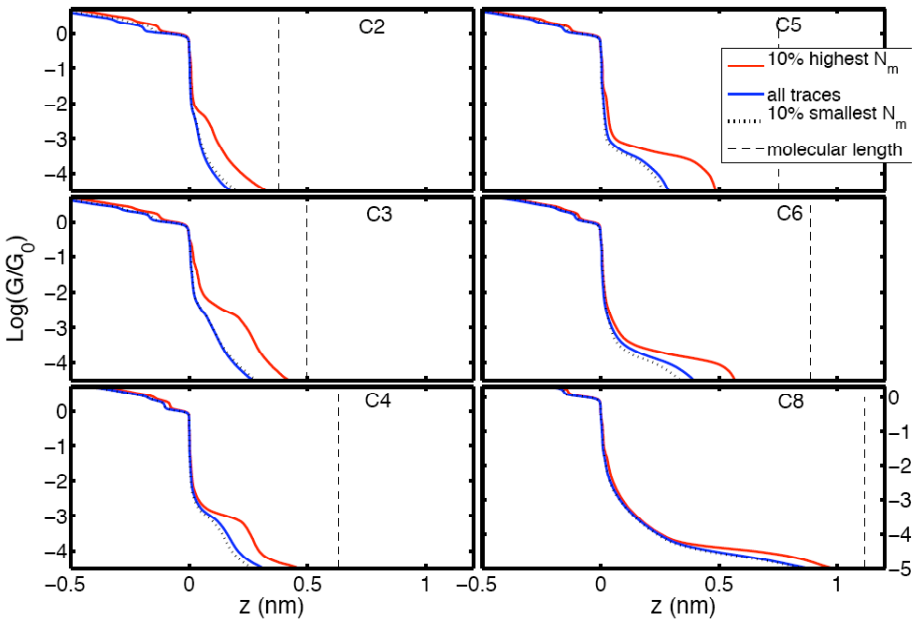

Figure 4.16: Average of Log(G/G_0) as a function of z computed by integration of the normalized conductance histograms built from conductance traces measured in presence of alkanediamines. The 10% of the conductane traces with longest plateaus (red lines), all the condutance traces (blue lines) and the 10% of the conductane traces with shortest plateaus (dotted lines). The vertical dashed lines represent the length of the molecule between anchoring groups.

Fitting to a gaussian function (see Fig. 4.17) the most characteristic peak in the conductance histograms, we have obtained the most prevalent conductance values. In Fig. 4.13 we compare the most prevalent conductanc value for all the conductance traces and for the 10% of conductance traces with longest plateaus. The error bars in these graphs correspond to the width of the gaussian function at $1/e$ of the maximum.

As we have discussed in Chap. 1 the transmission through these molecular junctions can be approximated as electron tunneling through a rectangular potential barrier. By computing the linear fit of the molecular junction conductance as a function of the number of methylene groups N_{CH2}, we obtain values for the decay factor β equal to 0.66 N_{CH2}^{-1} for alkanedithiols and 0.92 N_{CH2}^{-1} for alkanediamines. These values are in good agrement with previous works.

Trace selection

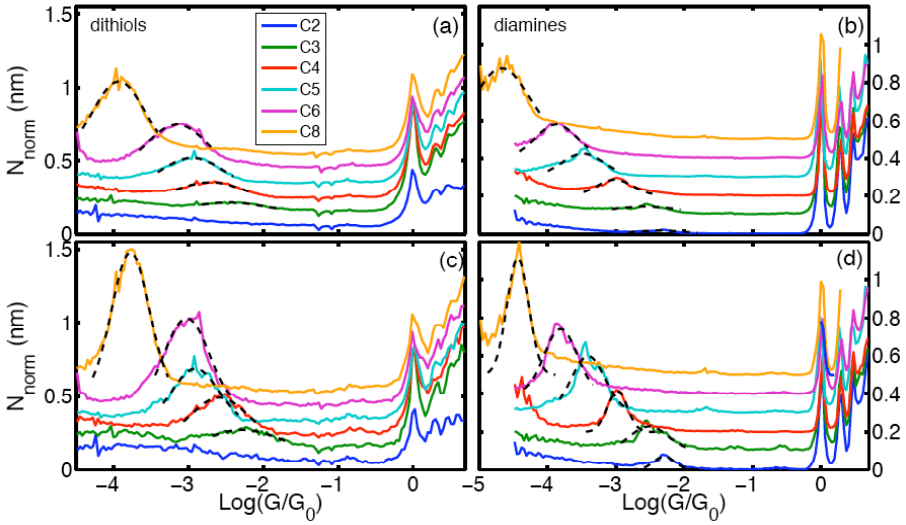

Figure 4.17: Normalized conductance histograms built from: (a) All the conductance traces for alkanedithiols, (b) all the conductance traces for alkanediamines (c) the 10% of conductance traces with longest plateaus for alkanedithiols and (d) the 10% of conductance traces with longest plateaus for alkanediamines. The dashed black lines indicate the Gaussian fit to determine the most prevalent conductance values.

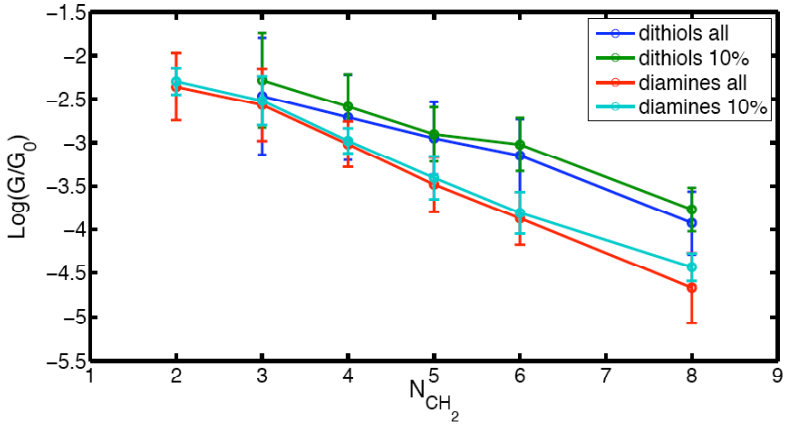

Figure 4.18: Most prevalent conductance values from conductance histograms built from: all the conductance traces for dithiols and diamines and for the 10% of conductance traces with longest plateaus for dithiols and diamines.

4.6 Summary and conclusions

In summary, we have characterized statistically the conductance evolution when atomic-sized gold contacts are broken in a solution containing alkanedithiols or alkanediamines with different lengths. A simple method to separate conductance traces, based in conductance histograms, provide useful information about the role of different anchoring groups during the formation of molecular junctions. We have analyzed the main differences observed between two different anchoring groups, thiols (-SH) and amines ($-NH_2$). The specific characteristics of the conductance traces during the formation of molecular junctions can be explained taking into consideration the differences on the bond strength between anchoring groups and gold atoms. The thiol is stronger than amine group and, causes atomic-scale rearrangements in the apexes of the electrodes.

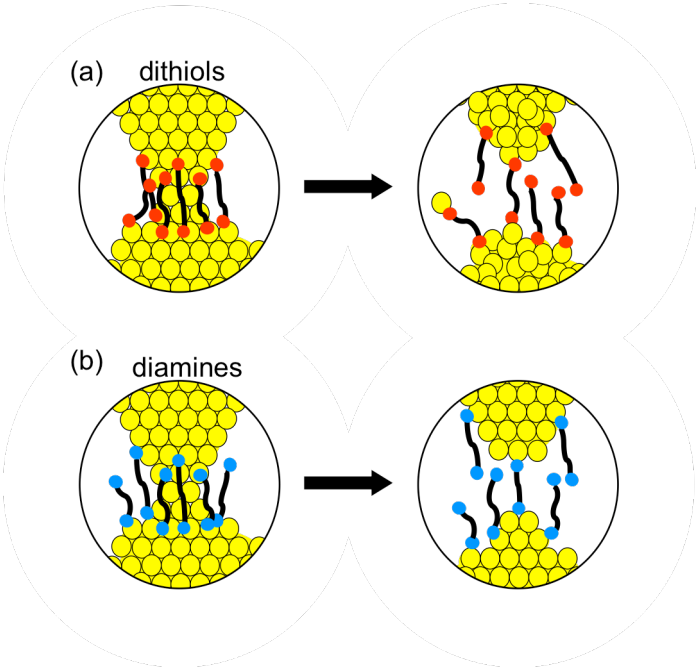

Figure 4.19: Cartoon showing the main differences during the formation of molecular junctions with thiols and amines as anchoring groups. (a) The stronger S-Au bond leads to plastic deformation of the electrodes during the junction formation. (b) In contrast, amines do not deform the electrodes.

Summary and conclusions

An important task that we have not solved yet is the presence of an adsorbate that forms clear plateaus around $Log(G/G_0)$=0.7. These plateaus have been observed in ambient conditions as well as in molecular solutions and can be due to water molecules or an adsorbate present at ambient conditions.

For next chapter is important to note that we have also realized experiments with molecules adsorbed to the substrate but without the organic solvent. The signature of the molecule is still present in the conductance histograms but usually appears more quantity of conductance traces with adsorbates.

References

[1] A. Aviram and M.A. Ratner, *"Molecular rectifiers"*, Chemical Physics Letters. **29** (1974).

[2] N.J. Geddes, J.R. Sambles, D.J. Jarvis, W.G. Parker and D.J. Sandman, *"Fabrication and investigation of asymmetric current voltage characteristics of a metal/Langmuir–Blodgett monolayer/metal structure"*, Applied Physics Letters. **56** (1990) 1916.

[3] M.L. Chabinyc, X. Chen, R.E. Holmlin, H. Jacobs, H. Skulason, C.D. Frisbie, V. Mujica, M.A. Ratner, M.A. Rampi and G.M. Whitesides, *"Molecular Rectification in a Metal- Insulator- Metal Junction Based on Self-Assembled Monolayers"*, J. Am. Chem. Soc. **124** (2002) 11730-11736.

[4] X.D. Cui, A. Primak, X. Zarate, J. Tomfohr, O.F. Sankey, A.L. Moore, T.A. Moore, D. Gust, G. Harris and S.M. Lindsay, Reproducible measurement of single-molecule conductivity, Vol. 294, 2001, pp. 571-574.

[5] C. Munuera, E. Barrena and C. Ocal, *"Scanning force microscopy three-dimensional modes applied to conductivity measurements through linear-chain organic SAMs"*, Nanotechnology. **18** (2007) 125505.

[6] Y.V. Kervennic, D. Vanmaekelbergh, L.P. Kouwenhoven and H.S.J. Van der Zant, *"Planar nanocontacts with atomically controlled separation"*, Applied Physics Letters. **83** (2003) 3782.

[7] J.G. Kushmerick, D.B. Holt, J.C. Yang, J. Naciri, M.H. Moore and R. Shashidhar, *"Metal-molecule contacts and charge transport across monomolecular layers: Measurement and theory"*, Phys. Rev. Lett. **89** (2002) 86802.

[8] M.A. Reed, C. Zhou, C.J. Muller, T.P. Burgin and J.M. Tour, *"Conductance of a molecular junction"*, Science. **278** (1997) 252.

[9] N. Agraït, A.L. Yeyati and J.M. van Ruitenbeek, *"Quantum properties of atomic-sized conductors"*, Phys. Rep. **377** (2003) 81–279.
[10] B. Xu and N.J. Tao, *"Measurement of Single-Molecule Resistance by Repeated Formation of Molecular Junctions"*, Science. **301** (2003) 1221.
[11] Z. Huang, F. Chen, P.A. Bennett and N. Tao, *"Single Molecule Junctions Formed via Au- Thiol Contact: Stability and Breakdown Mechanism"*, J. Am. Chem. Soc. **129** (2007) 13225-13231.
[12] J. Ulrich, D. Esrail, W. Pontius, L. Venkataraman, D. Millar and L.H. Doerrers, *"Variability of conductance in molecular junctions"*, J. Phys. Chem. B. **110** (2006) 2462-2466.
[13] F.L.X. Chen, J.H.Z. Hihath and N. Tao, *"Effect of anchoring groups on single-molecule conductance: comparative study of thiol-, amine-, and carboxylic-acid-terminated molecules"*, JACS. **128** (2006) 15874-15881.
[14] C. Li, I. Pobelov, T. Wandlowski, A. Bagrets, A. Arnold and F. Evers, *"Charge Transport in Single Au | Alkanedithiol | Au Junctions: Coordination Geometries and Conformational Degrees of Freedom"*, JACS. **130** (2008) 318-326.
[15] W. Haiss, R.J. Nichols, H. Zalinge, S.J. Higgins, D. Bethell and D.J. Schiffrin, *"Measurement of single molecule conductivity using the spontaneous formation of molecular wires"*, Physical Chemistry Chemical Physics. **6** (2004) 4330-4337.
[16] L. Venkataraman, J.E. Klare, C. Nuckolls, M.S. Hybertsen and M.L. Steigerwald, *"Dependence of single-molecule junction conductance on molecular conformation"*, Nature. **442** (2006) 904-907.
[17] M. Kamenetska, M. Koentopp, A.C. Whalley, Y.S. Park, M.L. Steigerwald, C. Nuckolls, M.S. Hybertsen and L. Venkataraman, *"Formation and Evolution of Single-Molecule Junctions"*, Phys. Rev. Lett. **102** (2009) 126803.
[18] M. Kiguchi, S. Miura, K. Hara, M. Sawamura and K. Murakoshi, *"Conductance of a single molecule anchored by an isocyanide substituent to gold electrodes"*, Applied Physics Letters. **89** (2006) 213104.
[19] I.S. Kristensen, D.J. Mowbray, K.S. Thygesen and K.W. Jacobsen, *"Comparative study of anchoring groups for molecular electronics: structure and conductance of Au–S–Au and Au–NH2–Au junctions"*, Journal of Physics: Condensed Matter. **20** (2008) 374101.
[20] L.A. Zotti, T. Kirchner, J.C. Cuevas, F. Pauly, T. Huhn, E. Scheer and A. Erbe, *"Revealing the Role of Anchoring Groups in the Electrical Conduction Through Single Molecule Junctions"*, small. **6** 1529-1535.

[21] M.T. Gonzalez, S. Wu, R. Huber, S.J. van der Molen, C. Schönenberger and M. Calame, *"Electrical conductance of molecular junctions by a robust statistical analysis"*, Nano Letters. **6** (2006) 2238.
[22] C.A. Martin, D. Ding, J.K. Sørensen, T. Bjørnholm, J.M. van Ruitenbeek and H.S.J. van der Zant, *"Fullerene-based anchoring groups for molecular electronics"*, J. Am. Chem. Soc. **130** (2008) 13198-13199.
[23] S.Y. Quek, L. Venkataraman, H.J. Choi, S.G. Louie, M.S. Hybertsen and J.B. Neaton, *"Amine-Gold Linked Single-Molecule Circuits: Experiment and Theory"*, Nano Letters. **7** (2007) 3477-3482.

V

Inelastic electron tunneling spectroscopy on single molecule junctions

One of the most challenging aspects to reach the ultimate miniaturization of electronic devices is the characterization of charge transport through a single molecule connected to two conducting electrodes. From an experimental point of view, it is a challenge to create and identify a junction with exactly one molecule between the electrodes.

In this chapter, I will present inelastic electron tunneling spectroscopy (IETS) measurements on molecular junctions of alkanedithiols covalently bound between gold electrodes. The molecular junctions are formed by means of the STM-based break-junction technique at low temperatures (4.2 K). The IET spectra permit a unique identification of the main vibrational modes, as well as their variation with strain. The good agreement between experiment and first-principles calculations strongly suggests the presence of a single molecule in different configurations between the electrodes(1).

5.1 The importance of IETS in molecular electronics

The ultimate goal of molecular electronics is to understand fundamentally the transport properties of single molecules, and therefore, to rationally design electrical devices based on this knowledge. A primary challenge towards the realization of such devices is to develop reliable methods to wire a single molecule between two electrodes. One approach to this problem has been discussed in Chap. 4. The STM-BJ and related techniques like MCBJ, have been used to investigate junctions consisting of a few or even a single molecule connected between metal electrodes. In Chap. 4, we have studied molecular junctions formed while atomic-sized gold contacts are broken in presence of molecules terminated with anchoring groups [1], like thiols (-SH) or amines (-

(1) Part of the work described here has been published in two papers: "Study of electron-phonon interactions in a single molecule covalently connected to two electrodes", J. Hihath, C.R. Arroyo, G. Rubio-Bollinger, N.J. Tao and N. Agrait, Nanolett. 8 (6), 1673-1678 (2008), and "Tunning vibrations in single-molecule junctions: inelastic electron tunneling spectroscopy of an alkanedithiol" C.R. Arroyo, T. Frederiksen, G. Rubio-Bollinger, M. Velez, A. Arnau, D. Sanchez-Portal and N. Agrait, Phys. Rev. B **81**, 075405 (2010).

NH_2). The conductance histograms at room temperature exhibit a prominent and broad peak, which indicate the formation of molecular junctions. The maximum of this peak indicates most probable molecular junction conductance, while the width reflects the microscopic variations from junction to junction. The main difficulty of this approach is to relate the specific atomic structure (i.e. molecular conformation or contact geometry) of a given molecular junction to its conductance. In this sense, an experimental technique that allows more advanced characterization of molecular junctions at atomic scale is desirable.

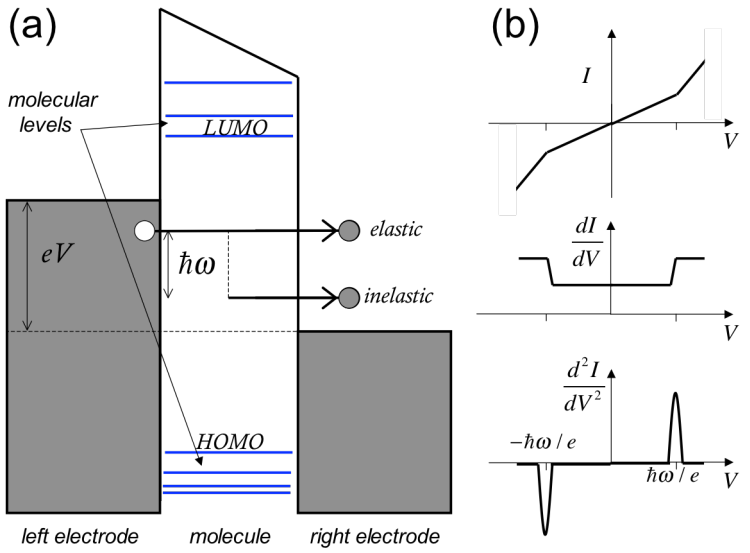

Figure 5.1: Scheme of a molecular junction: (a) At low voltages the electrons cross the molecular junction by simple tunneling. (b) The inelastic scattering of electrons by phonons opens up a new current path. These processes are observed as symmetric increases in the dI/dV above the threshold voltage $V=\pm\hbar\omega/e$, or antisymmetric peaks in d^2I/dV^2.

Inelastic electron tunneling spectroscopy (IETS) due to localized molecular vibrational modes was discovered in 1966 by Jaklevic and Lambe [2]. As we have discussed in Sect. 2.8, the excitation of a vibrational mode opens up a new current path, which gives an additional contribution to the tunneling current. Recently the use of IETS has regained popularity since it has been successfully applied to smaller junctions, using techniques like crossed wires [3], nanopores [4], silicon-molecule-metal devices [5] or microspheres [6].

Differences with previous works

At low temperatures, the vibrational modes of a junction where a single molecule is connected to two gold electrodes have zero occupation and may be excited by the electrons traversing the junction. At low voltages, in the linear response regime and, in the case that the molecular levels are far from the Fermi level of the electrodes (see Fig. 5.1), the electrons cross the molecular junction by simple tunneling. Due to the short length of the molecular junctions studied here, we remain in the limit of ballistic transport, in which most of the electrons flow through the molecule without any energy loss. Only a small fraction of these electrons undergoes inelastic scattering processes in which they exchange energy with vibrational modes or *phonons* of the molecular junction. The IET spectrum of a molecular junction establishes the presence of the molecule, i.e. its chemical integrity, but also one can interpret the maxima in the spectrum in terms of the specific paths that the electrons follow as they traverse the molecular junction [7, 8]. Moreover, the information extracted from IETS measurements could reveal the relationship between molecular configuration, contact geometry, and molecular conductance.

The inelastic effects in electron transport through molecules is a subject of study in a wide range of disciplines such as polymer solar cells, organic crystals, molecular LEDs, polymer batteries, thermoelectrics, gas sensing, odor recognition, chemical identification, current-induced chemical reactions, neurons and neural networks, etc.

In addition, the IETS technique has also provided information on a variety of elementary excitations, including for example plasmons, magnons or electron spin-flips. These phenomena are very interesting but are also far from the objectives of this thesis, we refer the interested reader to specialized books, such as [9] .

5.2 Novelty of present work

In the last years, several groups have performed IETS measurements on molecular junctions to obtain a chemical signature from the vibrational modes. It has been also possible to measure the IET spectra for an isolated molecule in a STM configuration [10]. In these measurements, molecules are adsorbed to a metal surface and the electrons flow by tunneling through a vacuum gap between the STM-tip and the molecule. Fig. 5.3 shows the IET spectra for an isolated acetylente (C_2H_2) molecule adsorbed on the copper (100) surface. The d^2I/dV^2 shows a peak at 358 mV, resulting from excitation of the C-H stretch mode. An isotopic shift (see Eq. 1) to 266 mV was observed for an isolated deuterated

acetylene (C_2D_2) molecule. Lee and Ho [11] showed that is possible to control the individual synthesis of single molecules with the STM-tip. They created molecules of Fe(CO) and $Fe(CO)_2$ on a silver (110) surface. The applied electric field between the STM-tip and the substrate was used to pick up, carry and deposit individual CO molecules. The structure of individual products was probed by analizing their IET spectra.

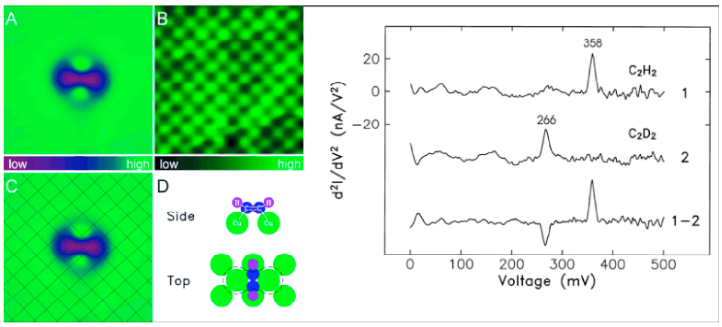

Figure 5.2: (A) STM image of a C_2H_2 molecule adsorbed on Cu (100). (B) The molecule in (A) was transferred and the same area was scanned. (C) The atoms in (B) were fitted to a lattice. (D) Schematic top and side view of the molecule's orientation. Graph: Inelastic electron tunneling spectra for an isolated acetylene (C_2H_2) and deuterated acetylene (C_2D_2) molecule adsorbed on Cu (100) surface. Figures taken from Ref. [10].

In the high-conducting regime, the inelastic spectra (in this case named PCS, see Sect. 2.8) have helped to understand some properties of atomic gold wires [12] and simple molecules [13-15]. The strain dependence of the inelastic signals has shed light into the microscopic structure of the junction. Smit *et al.* [13] characterized molecular junctions of a hydrogen molecule directly connected between platinum electrodes using the MCBJ technique. After introducing hydrogen gas into the system, the conductance histogram change qualitatively. Clean Pt contacts show the first peak at 1.5±0.2 G_0, in contrast after admitting hydrogen a pronounced peak appear near 1 G_0, see Fig. 5.3 (a). The differential conductance measured as a function of the applied voltage show a symmetric drop of 1 or 2 % at energies in the range of 50-60 meV, as expected for electron-phonon scattering, see Fig. 5.3 (b). The proof that the spectral features are indeed associated with hydrogen vibration modes comes from further experiments where H_2 is substituted by the heavier isotopes D_2 and HD. The fact that the energies of the onset of vibration modes were scaled by the expected isotope shifts,

Differences with previous works

$$\omega = \sqrt{\kappa / M} \tag{1}$$

where κ is the spring constant and M is the mass of the vibrating object, confirms that the junction is formed by a single hydrogen molecule.

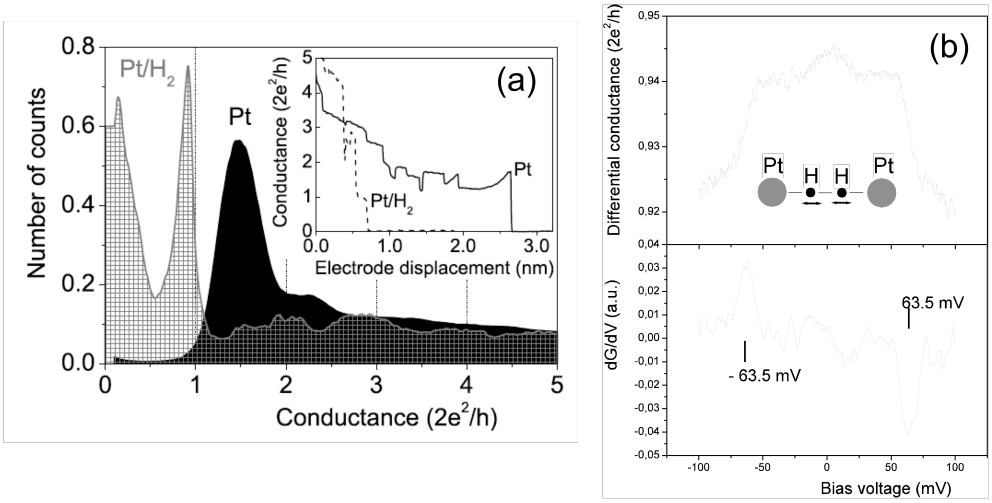

Figure 5.3: (a) Conductance histograms and two conductance traces of platinum contacts in absence (black) and in presence of hydrogen molecules. (b) Point contact spectroscopy spectra for a hydrogen molecular junction (H_2) connected between platinum electrodes. Figures taken from Ref. [13].

Recent publications [3, 4] show IET spectra of alkanedithiols and other thiolated molecules connected between gold electrodes (see Fig. 5.4). However, most of these studies have been done on junctions comprising a relatively large number of molecules in self-assembled monolayers (SAMs). In principle, the vibrational modes detected in the IET spectra, can be assigned by comparison with other spectroscopic technique such us, infrared (IR) or Raman. However, these techniques are based on different physical phenomena and, vibrations that are IR active can be IETS inactive or vice versa.

In this chapter we have focussed on a prototypical molecular wire consisting of individual alkanedithiol molecules covalently bound between two gold electrodes. By using a combination of conductance histograms and IETS measurements, we have characterized the molecular junctions at low temperatures. An exhaustive analysis of IET spectra, compared with state of the art first-principles calculations allow us to indentificate the main vibrational modes as well as their variations with the applied strain.

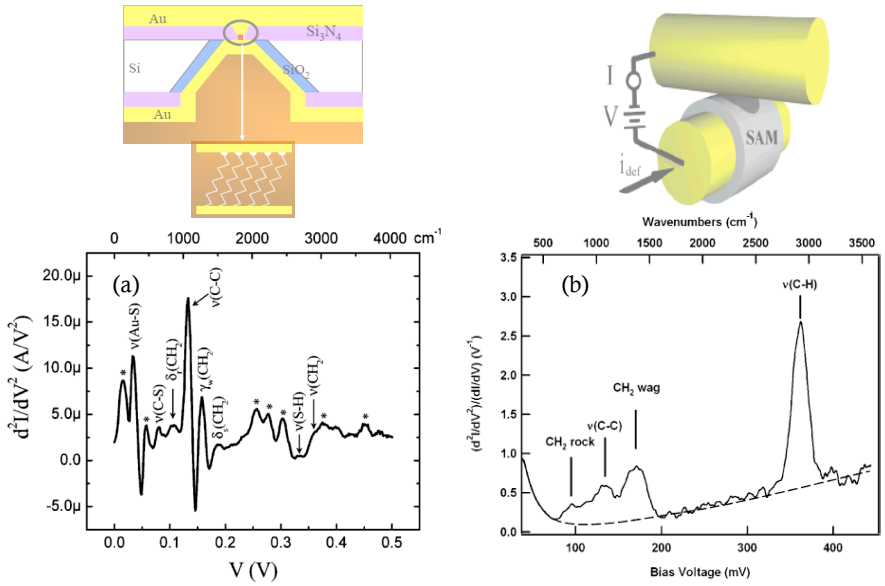

Figure 5.4: (a) IETS spectrum of octanedithiols in a SAM between gold electrodes using nanopores Ref. [4]. (b) IETS spectrum of C11 alkanethiol monolayer using crossed wires Ref. [3]. The spectra are obtained at 4.2 K using a lock-in amplifier.

5.3 IETS on molecular junctions: the experiment

We have studied two different alkanedithiols (Sigma-Aldrich): 1,3-propanedithiol (SH-$(CH_2)_3$-SH) and 1,5-pentanedithiol (SH-$(CH_2)_5$-SH). The chemical structure of these molecules is showed in Fig. 5.5.

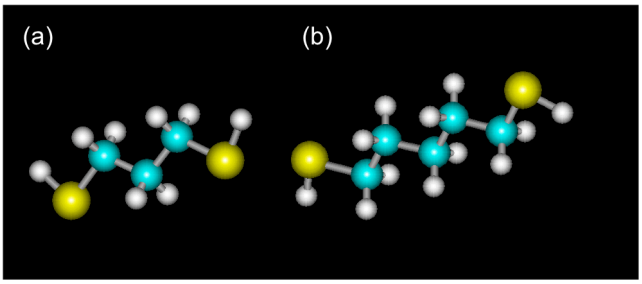

Figure 5.5: Chemical structure of the 1,3-propanedithiol (a) and the 1,5-pentanedithiol (b). The balls represent atoms of hydrogen in white, carbon in cyan and sulfur in yellow.

IETS in molecular junctions: the experiment

The experimental setup consists of a home build STM (described in Chap. 2) working at low temperatures (down to 250 mK). A commercially available gold substrate (Arandee 11×11 mm) was used for the sample preparation. The gold substrate was cleaned by inmersion in piranha solution (1:3 H_2O_2 (33%) in H_2SO_4 (98%)) for 1-2 minutes and rinsed several times with Milli-Q water. Then the gold surface was dried in a stream of He gas and flame annealed with a butane burner for 2-3 minutes. The clean substrate was inmersed in a 1mM solution of alkanedithiol[(2)] molecules in toluene for a period of 12 hours. To remove the molecules not adsorbed on gold, the substrate was sonicated in pure toluene, and dried in a stream of He gas. These deposition conditions are typical for the formation of self-assembled monolayers (SAMs), consequently we would expect a coverage close to a monolayer. The tip consisted of a freshly cut gold wire (99.99% purity), with 0.250 mm of diameter and approximately 1 mm in length. The tip and a freshly prepared substrate were fixed to the STM at ambient conditions. Inmediately after that, the STM was transferred to the cryostat and it was cooled to 4.2 K in an inert atmosphere of He gas (1 mbar of pressure at 300 K).

The procedure for the measurements shown here is similar to the one used for atomic gold wires (Sect. 3.3). Atomic-sized gold contacts are formed and broken repeatedly by moving the STM-tip towards and away from a spot of a gold surface covered with molecules. During the STM-tip movement, the evolution of the junctions was monitored by means of the conductance, $G=I/V$, when a bias voltage (typically 100 mV) was applied between the tip and substrate. In most of the junctions after the rupture of gold contacts, the conductance decreases exponentially with a high apparent tunneling barrier of 3-4 eV. In contrast, the presence of molecules in the junction is readily observed as a plateau in the conductance traces (see Fig. 5.6 (c)). In order to fabricate single molecule junctions, we have realized an automatic searching for plateaus around the conductance values obtained from molecular junctions experiments in solution at room temperature (Chap. 4). In Fig. 5.6 (a) we show a conductance plateau around 10^{-3} G_0, which is attributed to the conductance of pentanedithiol molecular junctions. When one of these plateaus was detected the tip movement was stopped and the differential conductance dI/dV, as a function of the applied bias voltage, was measured by using a lock-in amplifier (Sect. 2.4). In Fig 5.6 (b), we show a set of differential conductance curves acquired at different positions

(2) The experimental procedure was the same for propanodithiol and pentanodithiol molecules.

(marked with circles) of the conductance plateau. The corresponding IET spectra (see Fig. 5.6 (c)) are calculated by taking the numerical derivative of the dI/dV.

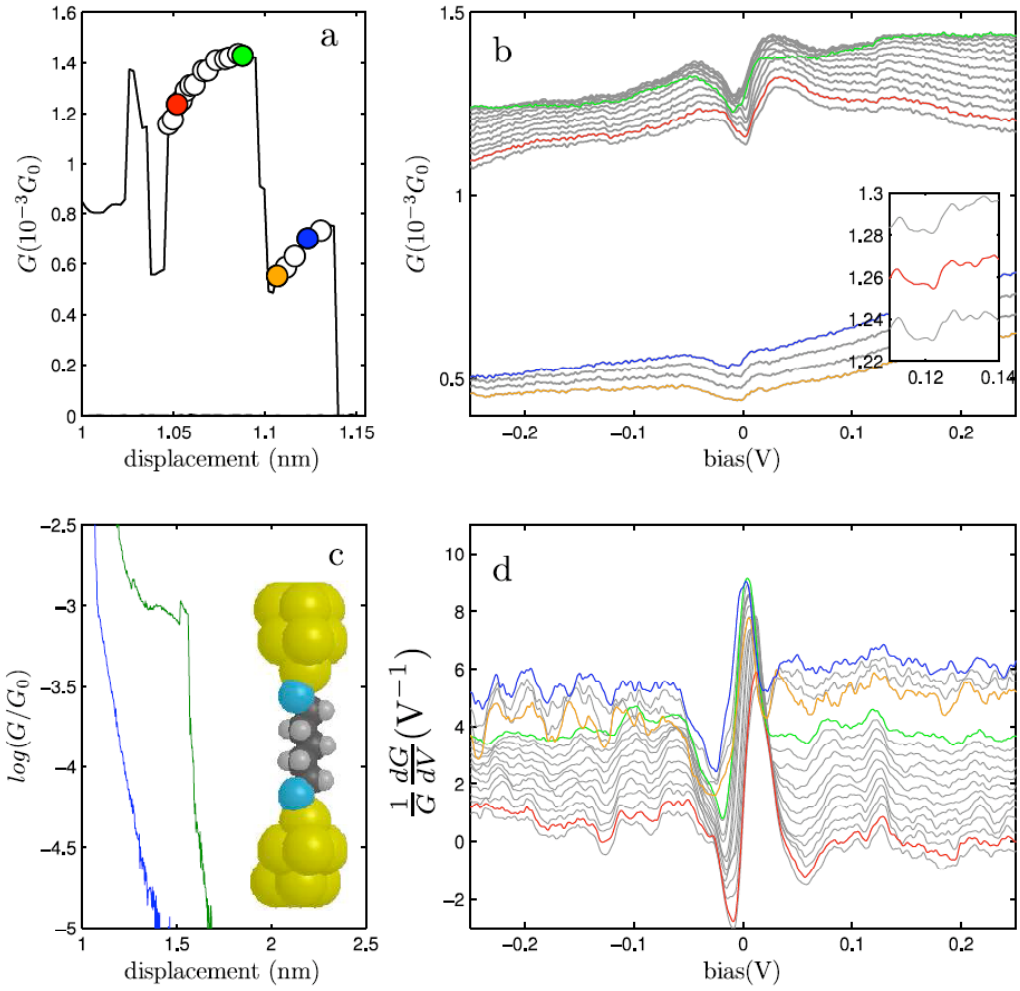

Figure 5.6: Conductance plateau (a) corresponding to a stable molecular junction. The circles indicate spots where it has measured the differential conductance as a function of the bias voltage (b). By numerical differentiation of (b) we obtain the IET spectra (c). Evolution of IET spectrum with the strain applied to the junction (c). (d) Represent the dependence of the frequency or peak position with the strain in the junction

IETS in molecular junctions: the experiment

Often the dI/dV curves show at low voltages (below 30 mV) a pronounced signal as a dip or a hump [3]. These effects, called zero bias anomalies (ZBA), are poorly understood and appear frequently in metallic junctions at low temperature [16, 17]. We will not give them further consideration in this chapter.

As in the case of atomic gold wires (Chap. 3), the large scale features observed in the differential conductance, are due to elastic scattering of electrons in the vicinity of the junction with defects or impurities [12]. Since these fluctuations have its origin mainly in the electrodes, the resulting features do not change much during elastic deformation of the junction. These features do not reflect the properties of the junction itself and vary markedly from junction to junction. In contrast, features due to the excitation of the molecular vibrations are symmetric in the dI/dV or antisymmetric in its derivative, the IET spectrum. The symmetry of the conductance jumps serves to distinguish the excitation of phonons from variations in the conductance due to elastic scattering processes that produce typically asymmetric signals.

As we have discussed before, the excitation of a vibrational mode of frequency ω in a junction requires passing electrons of energy $eV=\hbar\omega$ and, consequently an applied bias voltage larger than the threshold voltage, $V=\hbar\omega/e$. The excitation of a molecular vibration opens an additional conductance channel resulting in a sudden increase in the dI/dV at the threshold voltage. A careful inspection of the dI/dV curves (inset of Fig. 5.6 (c)) shows small conductance jumps at certain voltages. In the corresponding IET spectra (Fig. 5.6 (d)), the symmetric jumps in the differential conductance are observed as antisymmetric peaks. It should be noted that this is in contrast to what occurs in atomic gold wires where the excitation of a vibrational mode results in a decrease in the conductance. This is a consequence of the difference in the transmission between these two systems. As we have explained before (Chap. 3), an atomic gold wire has an almost completely open single quantum channel with a conductance very close to 1 G_0 and inelastic scattering can only result in back-scattering and a decrease in conductance (Sect. 3.5). However, in the case of molecules, the quantum channels are almost completely closed and inelastic scattering enhances the conductance. The crossover between enhance and decrease of the conductance is expected to occur for a transmission probability of 0.5, as was recently observed [18-20].

5.3.1 Experimental results: propanedithiol

In Fig. 5.7 (a) we show a conductance histogram built from 3000 conductance traces during the breaking process, one can observe a peak at 1 G_0 and an additional peak at 6×10^{-3} G_0, indicating the formation of stable propanedithiol molecular junctions. In the case of propanedithiol, we have found 155 stable junctions. In 13 of these junctions we have measured more than 10 IET spectrum before breaking. These 13 junctions provided a total of 448 spectra. One of these molecular plateaus during the stretching of the junction is observed in Fig. 5.7 (b). The four symbols represent four stretching distances where the dI/dV was measured as a function of the applied voltage. The corresponding IET spectra obtained numerically is shown in Fig. 5.7 (d). In these spectra, one can observe sharp symmetric peaks at ±43 mV and ±240 mV.

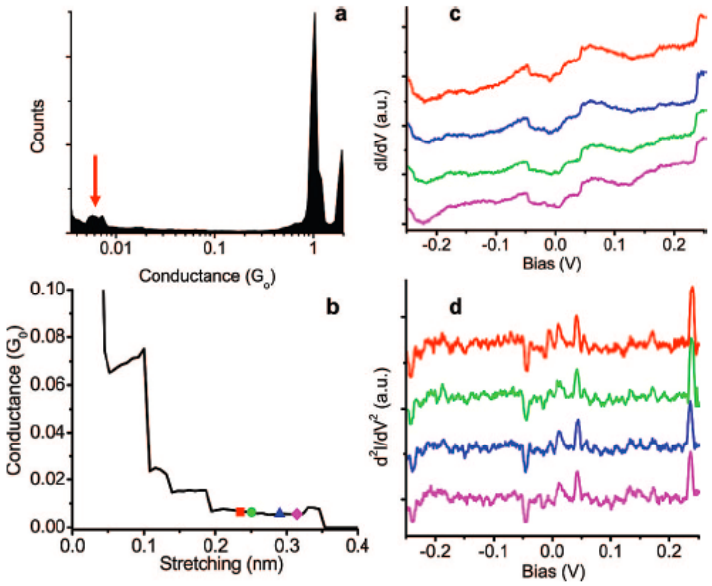

Figure 5.7: Single molecule IETS measurement. (a) Semilog conductance histogram shows a peak at G_0, and and additional peak at 6×10^{-3} G_0, which is attributed to the conductance of propanedithiol. (b) Conductance trace with a plateau close to 6×10^{-3} G_0 is found during the breaking process. The four symbols represent four stretching distances where the bias was swept and the differential conductance (c) was recorded, and (d) the corresponding IET spectra obtained numerically.

Experimental results: propanedithiol

In this experiment, the peaks observed in the individual spectra were difficult to reproduce. It can be due to the presence of propanedithiol molecules close to the molecular junction but not directly connected to both electrodes. These molecules have a negligible effect in the junction conductance however they could significantly change the inelastic spectrum.

To determine the peak positon in the IET spectra, we have used histograms taking into account the antisymmetry of these peaks. The process to make this determination entailed comparing all negative peaks found in the negative bias region with all positive peaks in the positive bias region for each spectrum. If a negative peak in the negative bias region was within 5% of a positive peak in the positive bias region, then both peaks were added to the phonon modes histogram. This process was completed for all spectra with a bias range greater than ±200 mV for the 13 junctions, and the resulting phonon histogram is shown in Fig. 5.8. There are several clear modes visible, since alkanedithiols have been widely studied, it is possible to assign several peaks from the literature [21-25].

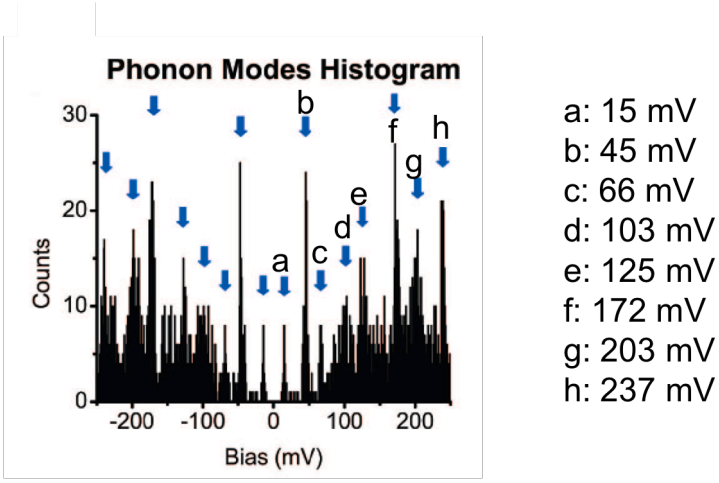

Figure 5.8: Phonon modes histogram built from all antisymmetric features from 448 spectra across 13 different junctions.

To illustrate the case where the molecule is anchored from both ends, we have used a simple one-dimensional model similar to that found repeatedly in the literature [26-29] for determining longitudinal accordion modes (LAM). In this model each atom in the chain is represented by a mass and the interatomic interaction is represented by a spring. In this case, a Au atom is anchored at each end, and a Au-S-CH_2-CH_2-CH_2-S-Au structure is placed between the two end

points. The masses for the atoms where 197 amu for Au, 32 amu for sulfur, and 14 amu for each CH_2 unit (1 amu=1.660×10^{-27} kg). Spring constants were obtained from the literature [27, 28, 30]. Au-S and C-S were 120 and 249 N/m, respectively, the C-C value was 520 N/m and the Au-Au spring constant used was 8 N/m. Finding the eigenvalues and eigenvectors from the resulting matrix produced vibration modes with energies of 4, 11, 26, 48, 73, 123 and 176 meV, in good agreement with many of the peaks observed in the phonon modes histogram Fig. 5.7. The values of the model that are not apparent in the histogram are at 4 and 26 meV, due largely to the Au-Au and Au-S stretch modes. These modes are likely hidden by the often dominant 15 mV mode. The other modes involve a combination of various vibrational modes of the molecular junction but are often dominated by a single mode. The additional peak at 103 mV is likely due to a CH_2 rock, which is a change in the angle between the C and the H atoms and therefore, it cannot be obtained with this model. Similarly, the modes at 203 and 237 mV are difficult to assign either with this model or by comparison with the literature since they do not appear to be active in IR or Raman spectra.

modes	methods	wavenumber (cm^{-1})	(meV)
ν(Au−S)	HREELS[14]	225	28
ν(C−S)	Raman[13]	641	79
	Raman[13]	706	88
	HREELS[14]	715	89
$\delta_r(CH_2)$	IR[15]	720	89
	IR[15]	766	95
	IR[15]	925	115
	HREELS[14]	1050	130
ν(C−C)	Raman[13]	1064	132
	Raman[13]	1120	139
	IR[15]	1230	152
$\gamma_{w,t}(CH_2)$	HREELS[14]	1265	157
	IR[15]	1283	159
	IR[15]	1330	165
$\delta_s(CH_2)$	HREELS[14]	1455	180
ν(S−H)	Raman[13]	2575	319
$\nu_s(CH_2)$	Raman[13]	2854	354
	HREELS[14]	2860	355
	Raman[13]	2880	357
$\nu_{as}(CH_2)$	Raman[13]	2907	360
	HREELS[14]	2925	363

Figure 5.9: Summary of the major vibrational modes of alkanethiols taken from Ref. [6].

5.3.2 Experimental results: pentanedithiol

In contrast to the propanedithiol experiment, the individual spectra of pentanedithiol molecular junctions show reproducible peaks at certain voltages. In this experiment, we have measured 33 stable molecular junctions characterized by a well-defined conductance plateau. The conductance histogram built from these conductance traces shows that most of the mechanically stable junctions have a conductance of approximately 10^{-3} G_0. This value is consistent with the results obtained at room temperature (Chap. 4) for pentanedithiol molecular junctions (see Fig. 5.10 (a) and (b)). It must be remarked that these histograms correspond to different situations and are not directly comparable. The room temperature histogram is built from all conductance traces while the low temperatures histogram corresponds to stable junctions.

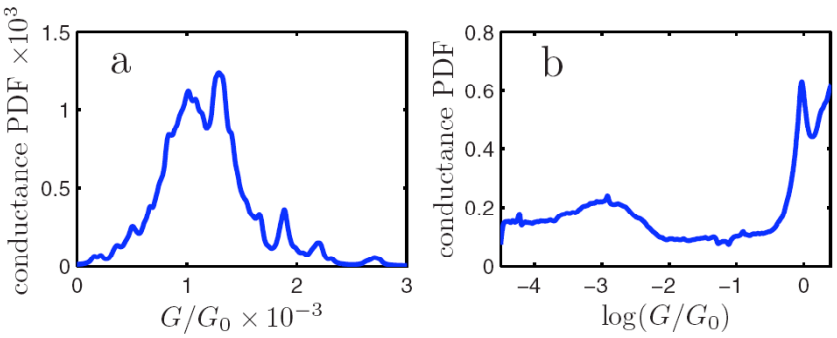

Figure 5.10: (a) Probability density function (PDF) of the low-bias conductance for 33 conductance traces corresponding to mechanically stable junctions. In the PDF we have used $\varepsilon = 3\times10^{-5}$. (b) PDF for the low-bias conductance built from 5000 conductance measured at room temperature in solution.

Taking from the IET spectra the voltage values where the differential conductance shows sudden changes, peaks at positive and dips at negative bias voltage polarity, we build the probability density function (PDF) of pentanedithiol molecular junctions as shown in Fig. 5.11 (c). All changes above the noise level are used to construct the PDF without further selection (see Appx. D). We have normalized the PDF to the number of spectra and consequently the integral of the PDF in a voltage interval represents the probability of finding a vibrational mode in this interval. There is a distribution for each peak, indicating that significant shifts in energy can occur for these modes. More precisely, the

probability is unity for finding a peak in the interval (125±10) mV (peak A), as well as for finding one in (85±13.5) mV (peak B). The signals of these vibrational modes can be observed directly in the individual spectra. The symmetry of some peaks in the PDF reveal the excitation of other vibrational modes (peaks C, D, E, F and G).

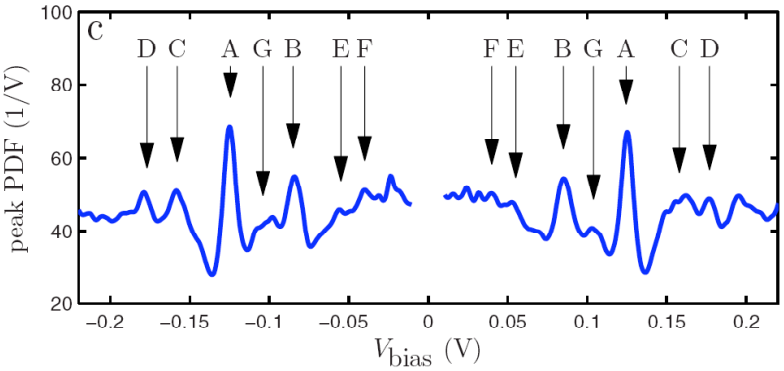

Figure 5.11: (c) Probability density function (PDF) of peaks at positive voltages and dips at negative voltages in the IET spectra for 33 conductance traces corresponding to mechanically stable junctions. Voltages around zero have been excluded due to the presence of zero-bias anomalies. In the PDF we have used ε= 3 mV.

5.4 Elastic response to the strain

In our measurements, as the one shown in Fig. 5.6, the molecular junction is deformed up to the breaking point by retracting the STM-tip gently. In some of the molecular junctions, the effect of the strain can be observed on the vibrational spectra as a shift in the position of peaks A and B (a maximum of 5-10 mV). It is not possible to follow the evolution of the other modes because their corresponding peaks are less well-defined. In Fig. 5.12 we show the position of the most prominent peaks (at 125 and 85 mV) as a function of the displacement of the tip, for the spectra shown in Fig. 5.6. These peaks shift to lower energy as the junction is stretched, similar to the behaviour observed for atomic gold wires. The conductance jump at a displacement of 1.095 nm in Fig 5.6 (a) results in a frequency jump in Fig. 5.12 demostrating that its origin is in a strain relaxation of the junction, probably due to an atomic rearrangement at the molecule-electrode interface [31].

Elastic response to the strain

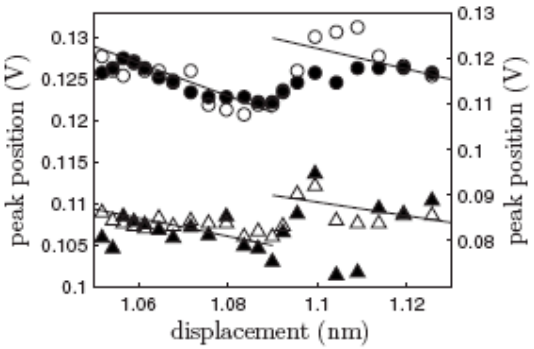

Figure 5.12: Peak position as a function of the tip retraction for the spectra shown in Fig. 5.6 (d). Circles correspond to peak A around 125 mV (left vertical axis) and triangles to peak B around 80 mV (right vertical axis). Filled and open symbols represent data obtained at positive and negative voltage polarity respectively.

To understand the features observed in the experiment, we have established a colaboration with the theoretical group composed by T. Frederiksen, A. Arnau and D. Sánchez-Portal (DIPC). They have performed First-principle transport calculations based on the Non-Equilibrium Green's Functions (NEGF) technique. The simulations attempt to mimic the experimental situation with a pentanedithiol molecule suspended between two gold electrodes, as shown in Fig. 5.13, assuming that the S atoms are bound to Au adatoms on Au(111) surfaces. The calculated zero-bias conductance for a single pentanedithiol is of the order of 0.005 G_0, i.e., about a factor 5 higher than the experimental value.

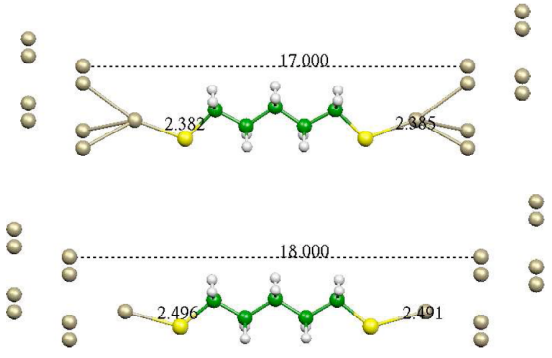

Figure 5.13: Two geometries at different state of strain used to calculate the IET spectra of a pentanedithiol molecular junction between gold electrodes.

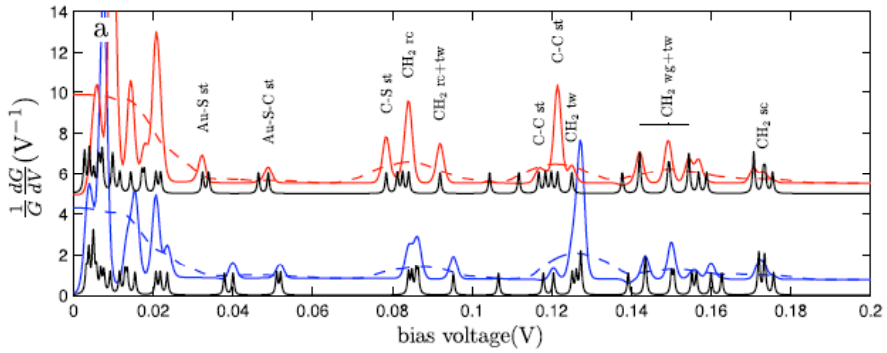

Figure 5.14: (a) Calculated IETS spectra of pentanedithiol for two different electrode separations (top-red more stretched than bottom-blue). The dashed curves are rounded using a T=4.2 K and V_{rms}=8 mV. The corresponding black curves (vertical axis scale arbitrary) represent the density of vibrational modes for these two configurations.

Fig. 5.14 (a) shows the calculated vibrational spectrum for a pentanedithiol between two Au electrodes for two different electrode separations. The different peaks are labeled according to the character of the mode (st=stretching, rc=rocking, wg=wagging, tw=twisting, sc=scissoring). We observe that there are active and inactive modes due to approximate selection rules, the so-called propensity rules [32]. For instance, we get a large signal from the C-C stretch mode ($\hbar\omega$=127 meV), while scattering is suppressed for the essentially transverse mode ($\hbar\omega$=106 meV).

For comparison with the experimental curves the rounding introduced by the ac modulation used to measure the differential conductance has also been included in the theory curves, shown with dashed lines in Fig. 5.14 (a). As a result of this rounding the some individual peaks cannot be resolved. All the peaks appearing in the PDF in Fig. 5.11 can be identified with some group of peaks in Fig. 5.14 (a).

A: C-C stretching with some contribution of CH_2 twisting.
B: C-S stretching with some contribution of CH_2 rocking.
C: CH_2 wagging and twisting
D: CH_2 scissoring
E: Au-S-C stretching
F: Au-S stretching
G: CH_2 rocking and twisting

Elastic response to the strain

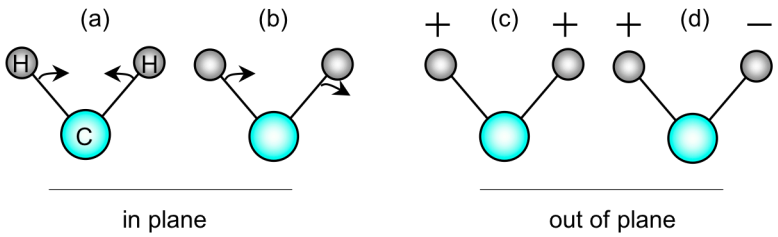

Figure 5.15: Bending vibrational modes of CH_2. (a) Scissoring: scissor-like motion of the two hydrogen atoms, (b) Rocking: motion of the two hydrogen atoms in the same direction, (c) Wagging: symmetrical motion of the two hydrogen atoms forwards and backwards respect to the plane of the CH_2 molecule (out of plane) (d) Twisting: antisymmetrical motion of the two hydrogen atoms out of plane.

A detailed comparison with the experiment also requires considering that the molecules are in different states of strain. We have calculated the spectra for two different elongations of the molecule to determine the strain dependence of modes. In this way we can characterize the C-C (C-S) mode, i.e., peak type A (B), by a shift of -5.0 (-2.9) meV/Angstrom, consistent with the experimental results. This result strongly suggests the presence of a single molecule between the electrodes. Indeed, if there were more molecules in the junction contributing to the transport, they would certainly be in different states of strain due to the irregularities of the electrodes and, thus, preclude the observation of clear frequency shifts. Fig. 5.11 (c) shows (thick black traces) the excellent agreement between experiment and theory, even the magnitude of the inelastic signals is quantitatively reproduced.

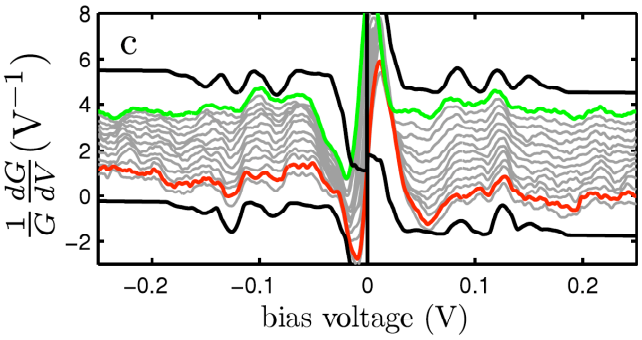

Figure 5.13: Comparation of IET spectra obtained experimentally while the junction is continously stretched (color lines) and IET spectra calculated for two different electrode separation (black lines).

5.5 Discussion and Conclusions

One of the main goals of molecular electronics is to explore and understand electron transport through a single molecule. This certainly requires a detailed comparison with quantum theory. However, the main problem with these experiments is the lack of characterization of the junction. It is generally assumed based on conductance histograms that the junction consists of just a single molecule. However, we cannot control the molecule lead coupling nor the environment on the atomic scale. In our work we clearly show that it is possible to characterize in situ the molecular junction, which allows for detailed comparison with theoretical calculations based on quantum mechanics.

In conclusion, our results show that it is possible to characterize single molecule junctions by using high-resolution low-temperatures IETS. The excellent agreement between the calculated spectra and those obtained experimentally, allows us to draw an important conclusion: the electrons are passing through the backbone of a pentanedithiol molecule that it is wired to the electrodes by the thiol groups.

References

[1] B. Xu and N.J. Tao, *"Measurement of Single-Molecule Resistance by Repeated Formation of Molecular Junctions"*, Science. **301** (2003) 1221.

[2] R.C. Jaklevic and J. Lambe, *"Molecular vibration spectra by electron tunneling"*, Phys. Rev. Lett. **17** (1966) 1139-1140.

[3] J.G. Kushmerick, J. Lazorcik, C.H. Patterson, R. Shashidhar, D.S. Seferos and G.C. Bazan, *"Vibronic contributions to charge transport across molecular junctions"*, Nano Lett. **4** (2004) 639-642.

[4] W. Wang, T. Lee, I. Kretzschmar and M.A. Reed, *"Inelastic electron tunneling spectroscopy of an alkanedithiol self-assembled monolayer"*, Nano Letters. **4** (2004) 643-646.

[5] W. Wang, A. Scott, N. Gergel-Hackett, C.A. Hacker, D.B. Janes and C.A. Richter, *"Probing Molecules in Integrated Silicon- Molecule- Metal Junctions by Inelastic Tunneling Spectroscopy"*, Nano Lett. **8** (2008) 478-484.

[6] D.P. Long, J.L. Lazorcik, B.A. Mantooth, M.H. Moore, M.A. Ratner, A. Troisi, Y. Yao, J.W. Ciszek, J.M. Tour and R. Shashidhar, *"Effects of hydration on molecular junction transport"*, Nature Materials. **5** (2006) 901-908.

[7] A. Troisi, J.M. Beebe, L.B. Picraux, R.D. van Zee, D.R. Stewart, M.A. Ratner and J.G. Kushmerick, *"Tracing electronic pathways in molecules by using inelastic tunneling spectroscopy"*, Proceedings of the National Academy of Sciences. **104** (2007) 14255.
[8] A. Troisi, *"Inelastic electron tunnelling in saturated molecules with different functional groups: correlations and symmetry considerations from a computational study"*, Journal of Physics: Condensed Matter. **20** (2008) 374111.
[9] E.L. Wolf, *Principles of electron tunneling spectroscopy*, Oxford University Press Oxford, 1985.
[10] B.C. Stipe, M.A. Rezaei and W. Ho, *"Single-molecule vibrational spectroscopy and microscopy"*, Science. **280** (1998) 1732.
[11] H.J. Lee and W. Ho, *"Single-bond formation and characterization with a scanning tunneling microscope"*, Science. **286** (1999) 1719.
[12] N. Agraït, C. Untiedt, G. Rubio-Bollinger and S. Vieira, *"Onset of energy dissipation in ballistic atomic wires"*, Phys. Rev. Lett. **88** (2002) 216803.
[13] R.H.M. Smit, Y. Noat, C. Untiedt, N.D. Lang, M.C. Van Hemert and J.M. Van Ruitenbeek, *"Measurement of the conductance of a hydrogen molecule"*, Nature. **419** (2002) 906-909.
[14] O. Tal, M. Kiguchi, W.H.A. Thijssen, D. Djukic, C. Untiedt, R.H.M. Smit and J.M. van Ruitenbeek, *"Molecular signature of highly conductive metal-molecule-metal junctions"*, Phys. Rev. B. **80** (2009) 85427.
[15] M. Kiguchi, O. Tal, S. Wohlthat, F. Pauly, M. Krieger, D. Djukic, J.C. Cuevas and J.M. van Ruitenbeek, *"Highly conductive molecular junctions based on direct binding of benzene to platinum electrodes"*, Phys. Rev. Lett. **101** (2008) 46801.
[16] S. Gregory, *"Inelastic tunneling spectroscopy and single-electron tunneling in an adjustable microscopic tunnel junction"*, Phys. Rev. Lett. **64** (1990) 689-692.
[17] H.B. Weber, R. Häussler, H. Loehneysen and J. Kroha, *"Nonequilibrium electronic transport and interaction in short metallic nanobridges"*, Phys. Rev. B. **63** (2001) 165426.
[18] L. de La Vega, A. Martin-Rodero, N. Agrait and A.L. Yeyati, *"Universal features of electron-phonon interactions in atomic wires"*, Phys. Rev. B. **73** (2006) 75428.
[19] O. Tal, M. Krieger, B. Leerink and J.M. van Ruitenbeek, *"Electron-Vibration Interaction in Single-Molecule Junctions: From Contact to Tunneling Regimes"*, Phys. Rev. Lett. **100** (2008) 196804.
[20] M. Paulsson, T. Frederiksen and M. Brandbyge, *"Modeling inelastic phonon scattering in atomic-and molecular-wire junctions"*, Phys. Rev. B. **72** (2005) 201101.

[21] S.K. Nandy, D.K. Mukherjee, S.B. Roy and G.S. Kastha, *"Vibrational spectra and rotational isomerism of 1, 2-propanedithiol"*, The Journal of Physical Chemistry. **77** (1973) 469-471.
[22] M.A. Bryant and J.E. Pemberton, *"Surface Raman scattering of self-assembled monolayers formed from 1-alkanethiols at silver [electrodes]"*, JACS. **113** (1991) 3629-3637.
[23] S.W. Joo, S.W. Han and K. Kim, *"Adsorption characteristics of 1, 3-propanedithiol on gold: Surface-enhanced Raman scattering and ellipsometry study"*, J. Phys. Chem. B. **104** (2000) 6218-6224.
[24] H.S. Kato, J. Noh, M. Hara and M. Kawai, *"An HREELS study of alkanethiol self-assembled monolayers on Au (111)"*, J. Phys. Chem. B. **106** (2002) 9655-9658.
[25] N.P.G. Roeges and J.M.A. Baas, *A guide to the complete interpretation of infrared spectra of organic structures*, Wiley hichester etc., 1994.
[26] R.F. Schaufele and T. Shimanouchi, *"Longitudinal acoustical vibrations of finite polymethylene chains"*, The Journal of chemical physics. **47** (1967) 3605.
[27] C.S. Levin, B.G. Janesko, R. Bardhan, G.E. Scuseria, J.D. Hartgerink and N.J. Halas, *"Chain-length-dependent vibrational resonances in alkanethiol self-assembled monolayers observed on plasmonic nanoparticle substrates"*, Nano Lett. **6** (2006) 2617-2621.
[28] G. Minoni and G. Zerbi, *"End effects on longitudinal accordion modes: fatty acids and layered systems"*, The Journal of Physical Chemistry. **86** (1982) 4791-4798.
[29] E.B. Wilson, Molecular vibrations: the theory of infrared and Raman vibrational spectra, McGraw-Hill, 1955.
[30] B. Xu, H. He, S. Boussaad and N.J. Tao, *"Electrochemical properties of atomic-scale metal wires"*, Electrochimica Acta. **48** (2003) 3085-3091.
[31] G. Rubio, N. Agrait and S. Vieira, *"Atomic-sized metallic contacts: mechanical properties and electronic transport"*, Phys. Rev. Lett. **76** (1996) 2302-2305.
[32] M. Paulsson, T. Frederiksen, H. Ueba, N. Lorente and M. Brandbyge, *"Unified description of inelastic propensity rules for electron transport through nanoscale junctions"*, Phys. Rev. Lett. **100** (2008) 226604.

Appendices

A. Tight-binding model for an atomic wire

In order to ilustrate the use of the Green function formalism, we may consider a Tight-Binding model. The Hamiltonian in second quantization, for an atomic wire of identical atoms with interaction to first-neighbors and one orbital per site can be expressed as:

$$H_C = \varepsilon_0 \sum_i |i\rangle\langle i| - t\sum_i |i+1\rangle\langle i| + |i\rangle\langle i+1| \tag{A.1}$$

where ε_0 correspond to the site energy and t denote the hopping between first-neighbors. In matricial notation this Hamiltonian is given by,

$$H_C = \begin{pmatrix} \varepsilon_0 & -t & 0 & \cdots & 0 \\ -t & \varepsilon_0 & -t & \cdots & 0 \\ 0 & -t & \varepsilon_0 & -t & \vdots \\ \vdots & \vdots & \vdots & \ddots & -t \\ 0 & \cdots & 0 & -t & \varepsilon_0 \end{pmatrix} \tag{A.2}$$

By using Bloch functions[1] as

$$|i+n\rangle = e^{inka}|i\rangle \tag{A.3}$$

where a is the spacing between nearest neighbor atoms. We can calculate the electronic band structure for this system

$$E = \langle i|H_C|i\rangle = \varepsilon_0 - 2t\cos(ka) \tag{A.4}$$

where, the wavevector k extends from π/a to $-\pi/a$. If we assume that each electronic state is occupied by two electrons of opposite spin, then the Femi energy is located at ε_0, and the Fermi wave vector at $k_F=\pi/2a$.

As electrodes we will use semi-infinite one-dimensional wires with the same hopping as in the central wire t. In order to determine the transmission and the local density of states (*LDOS*) of the wire connected between the electrodes, we need to obtain the Green's function for the uncoupled electrodes, which in the

(1) The Bloch's theorem states that the eigenfunctions of a system in a periodic potential may be written as the product of a plane wave and a periodic function with the same period as the potential.

Appendix

case of semi-infinite 1D-wires can be found analytically [1], taken for simplicity ε_0=0,

$$g^{+}_{L,R} = \frac{E + s\sqrt{E^2 - 4t^2}}{2t^2} \quad \text{and} \quad g^{-}_{L,R} = \frac{E - \sqrt{E^2 - 4t^2}}{2t^2} \tag{A.5}$$

where, by the definition of the Green's functions (Eq. (20), Chap. 1), the imaginary part of $g^{+}_{L,R}$ must be positive so, s=-1 if $E^2 > 4t^2$ and s=1 when $E^2 < 4t^2$.

In this model the coupling terms are given simply by

$$V_{LC} = (-t_L, 0, 0, 0) \quad V_{CL} = V'_{LC} \quad V_{RC} = (0, 0, 0, -t_R) \quad V_{CR} = V'_{RC} \tag{A.6}$$

where V' denotes the transpose of V.

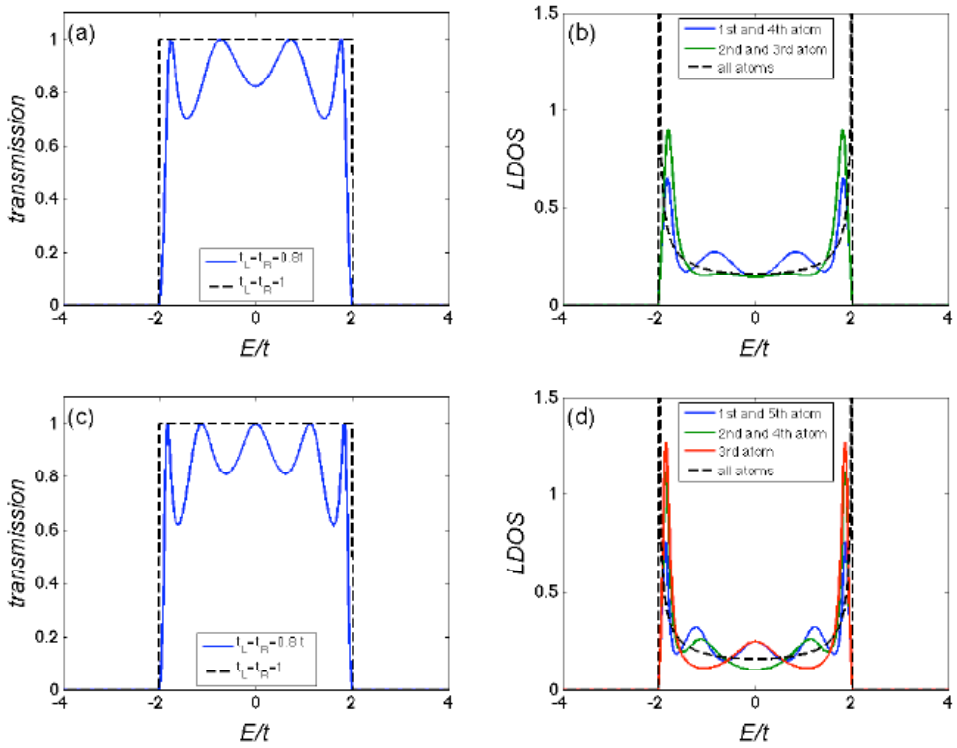

Figure A.1: Atomic wires of 4 and 5 atoms connected between two semi-infinite atomic wires with the same coupling as in the central wire. (a) Transmission and (b) Local density of states (LDOS) of an atomic wire of 4 atoms. The coupling with the electrodes $t_L$and t_R have been taken equal to 0.8 t (colour lines) and equal to t (black dashed lines). (c) and (d) represent the transmission and LDOS of an atomic wire of 5 atoms. Note that when the coupling is not perfect (t_L= t_R=0.8 t) the transmission at the Fermi level (E/t=0) is higher for a wire with odd number of atoms.

Appendix

The transmission of the wire connected to the electrodes is given by,

$$T = Tr\left[\hat{t}^{\dagger}(E)\hat{t}(E)\right] \tag{A.7}$$

where $\hat{t}$ has been defined in Eq. (29), Chap.1.
And, the *LDOS* is given by Eq. (21),

$$LDOS = \pm\frac{1}{\pi}\mathrm{Im}\left[G_C^{\pm}\right] \tag{A.8}$$

where the retarded G_C^{+} and, advanced G_C^{-} Green's functions have been defined in Eq. (26) of Chap. 1.

The dependence of the the transmission and the *LDOS*, as a function of the energy (E/t), for the case of symmetric coupling with the electrodes is illustrated in Fig. A.1. We show the transmission, Fig. A.1 (a) and (c), and the *LDOS*, Fig. A.1 (b) and (d), for two atomic wires of 4 and 5 atoms respectively. To determine the effect of the coupling of the wires with the electrodes, we have used two different values, $t_L = t_R = t$ (dashed black lines) and $t_L = t_R = 0.8\,t$ (color lines). In the case of perfect coupling with the electrodes, $t_L = t_R = t$, the transmission is equal to one in all the band, there is no difference between the atoms of the wire and the electrodes and, therefore the *LDOS* is that corresponding to an infinite wire. When we vary the coupling with the electrodes $t_L = t_R = 0.8\,t$, the transmission and the *LDOS* change significatly. The *LDOS* shows peaks due to localizated electronic states while the transmission oscilates.

In Fig. A.2 (a), we have calculated the transmission at the Fermi energy (E/t=0) as a function of the number of atoms in the wire, for different values of symmetric coupling $t_L = t_R = 0.8,\ 0.6$ and $0.4\,t$. It is important to realize that in the case of imperfect coupling with the electrodes, the transmission depends of the number of atoms in the wire. For an odd number of atoms, the transmission will be one even for imperfect coupling, while for an even number of atoms the conductance will decrease with decreasing the coupling. The oscillatory behaviour of conductance as a function of the length of the wire, so-called even-odd effect, was experimentally observed by Smit et al. in Au, Pt and Ir wires (see Fig A.3). This effect has been attributed to the interferece of the incident wave with the wave reflected as a result of the elastic scattering of electrons at the electrodes. In Fig. A.2 (b) we summarize the differences in the transmission of wires of 4 and 5 atoms, by using different couplings between the wire and the electrodes.

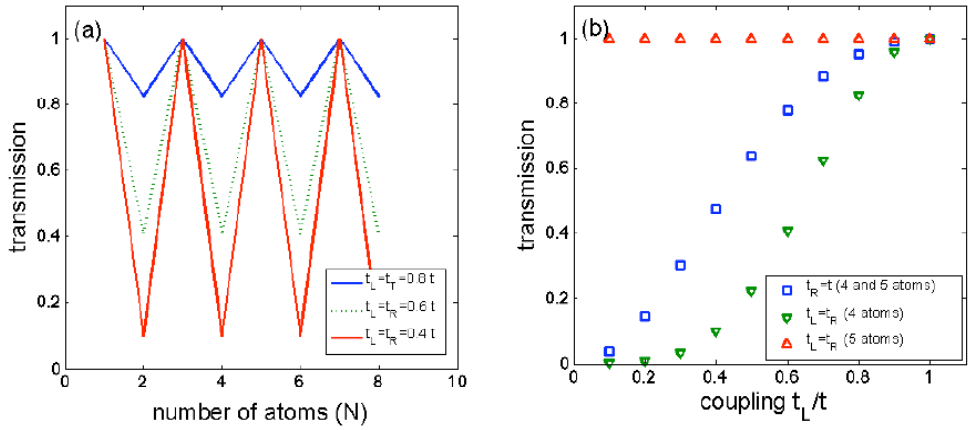

Figure A.2: (a) Transmission as a function of the number of atoms for different couplings with the electrodes. (b) Transmission for desigual coupling in the left and right electrode.

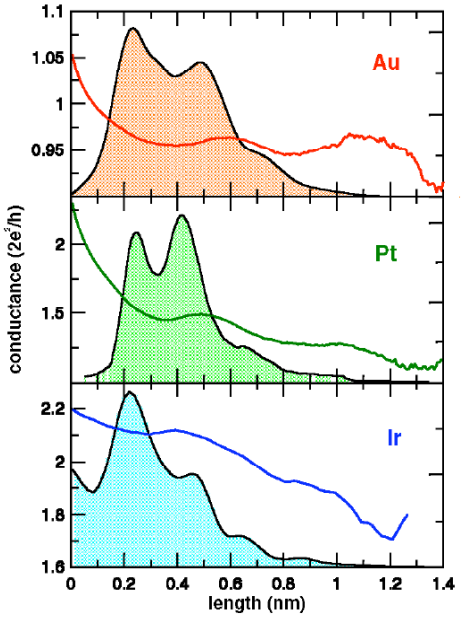

Figure A.3: Average plateaus of conductance traces for wires of: Au, Pt, and Ir. Each of the curves represents the average of conductance plateaus of individual conductance traces during the breaking process. Plateau length histograms for the three metals are shown as filled curves. Figure taken from Ref.

B. Calibration of fine tip positioning

Most of the scanning probe techniques make use of piezoelectric transducers to scan a tip over a surface with subatomic resolution. An accurate calibration of the displacements of these transducers as a function of the applied voltage is necessary to obtain quantitative information about the topography of the surface under study.

We present a method[(2)] to calibrate the displacement of piezo electric actuators by means of a reference voltage-to-displacement transducer based on a quartz tuning fork. This method relies on the comparison between the displacement of the uncalibrated actuator and the one of a calibrated reference quartz tuning fork. We find quartz tuning fork very adequate to be used as reference actuators because they meet most of the desirable properties of an ideal voltage-to-distance reference: low aging, hysteresis and creep, and by other hand, high linearity and thermal stability. Moreover the tuning fork geometry guarantees displacements in an appropriate range to calibrate the actuators used in scanning probe microscopy (SPM).

Mass production of quartz single-crystal actuators by the electronic and watch industries makes them very reliable, affordable and easy to obtain. The movement of the tuning fork prongs can be modeled as a damped, driven harmonic oscillator,

$$m\ddot{x} + b\dot{x} + kx = F_0 \cos(\omega t) \tag{B.1}$$

The solution of the equation (B.1) is a sum of a transient solution that depends on the initial conditions and, a steady-state solution that is independent of the initial conditions and depends on the driving frequency, driving force and damping force.

The transient solution is

$$x_t(t) = A_0 e^{-(\omega_0/2Q)t} \cos(\omega' t + \phi) \tag{B.2}$$

where A_0 and ϕ depends on the initial conditions, $\omega_0 = \sqrt{\frac{k}{m}}$ is the frequency in resonance, $Q = \frac{m\omega_0}{b}$ is the Q factor and $\omega' = \omega_0 \sqrt{1 - \frac{1}{4Q^2}}$

The steady-state solution is

$$x_s(t) = A \sin(\omega t - \delta) \tag{B.3}$$

(2) Part of the work described here will be published in the paper: "Calibration of piezoelectric positioning actuators using a reference voltage-to-displacement transducer based on quartz tuning forks". A. Castellanos-Gomez, C. R. Arroyo, N. Agrait and G. Rubio-Bollinger. (In preparation)

where $A = \dfrac{F_0}{\sqrt{m^2(\omega_0^2 - \omega^2)^2 + b^2\omega^2}}$ and $\delta = \arctan\left(\dfrac{b\omega}{m(\omega_0^2 - \omega^2)}\right)$

In resonance ($\omega = \omega_0$), the amplitude of movement of the tuning fork's prongs is quite large and we can use an optical microscope[3] to measure the displacements.

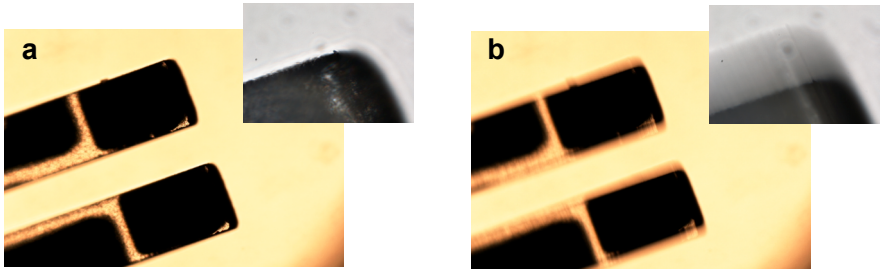

Figure B.1: Optical pictures of the tuning fork's legs. (a) stopped, (b) in resonance. In the inset can be obserbed the end of one leg.

In Fig. B.2 it can be observed the amplitude of the tuning fork's prongs oscillation as a function of the driving frequency. The fitting of these data to a Lorentzian function gives us the resonance frequency of the tuning fork.

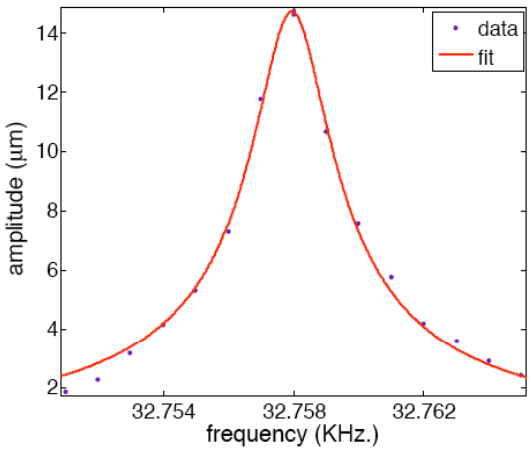

Figure B.2: Amplitude of oscilation of the tuning fork's legs as a function of the driving frequency.

(1) We have used a Canon EOS 550D camera attached to a Nikon Eclipse LV-100 optical microscope. The distances in the optical microscope can be calibrated by using the distance between tracks on a CD as a pattern.

Appendix

In resonance (f=32,760.3±0.1 Hz) we have measured the amplitude of oscillation of a tuning fork prong as a function of the applied voltage. We have found that the accuracy of the measurement of the oscillation amplitude improves using stroboscopic illumination [2]. To do so, the tuning fork is illuminated with a light emitting diode modulated twice the resonance frequency. Some of the pictures used are shown in Fig. B.3.

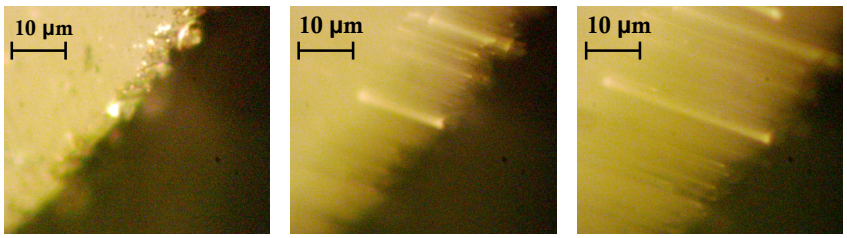

Figure B.3: Optical microscope pictures of the tuning fork prong used for the calibraion of the movement in resonance.

In Fig. B.4 (a) it can be observed the amplitud of oscilation (peak to peak) versus the applied voltage (peak to peak). The slope in this graph gives us the calibration in resonance for the tuning fork prong movement. The calibration for the tuning fork used was 3.9±0.1 µm/V.

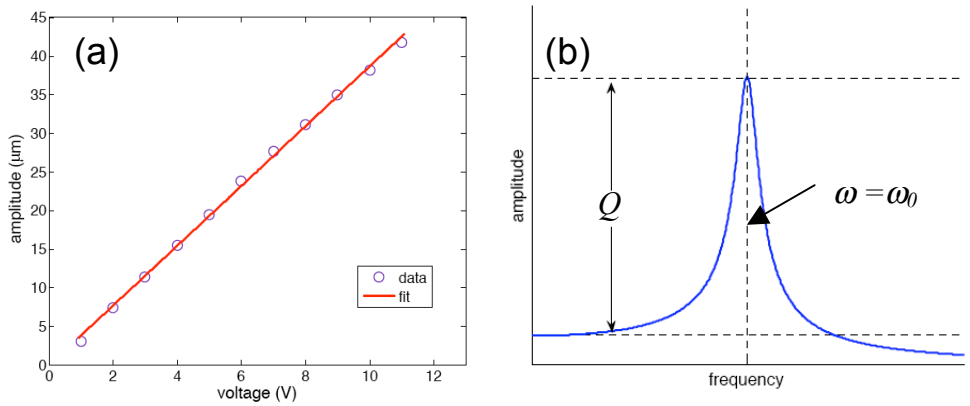

Figure B.4: (a) Amplitude (peak to peak) of the tuning fork prongs in resonance (f=32.760,3 KHz) as a function of the applied voltage (peak to peak). (b) Amplitud of the steady-state solution as a function of the driving frequency. Note that, in resonance the amplitud is Q times bigger that in DC (ω=0).

From the steady-state solution (Eq. B3), it can observed that at $\omega=0$ the amplitude is Q times smaller than in resonance $\omega=\omega_0$ (see Fig. B.4 (b)).

To determine the Q factor we use the ring down method. In this method, we excite the tuning fork and measure how the piezo electric current decays when the excitation is switched off. The piezo electric current is proportional to the amplitude of oscilation. From Eq. (B.2) we known that the envelop of the transient solution is related with the Q factor and the frequency in resonance.

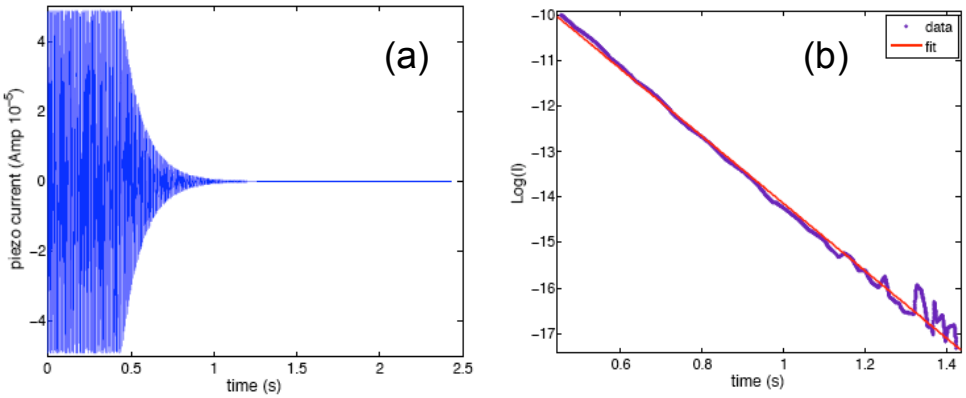

Fig. B.5. (a) Transient behabiour of the tuning fork in terms of the piezoelectric current. The envelop of the transient solution and linear fit used for determining the Q factor.

The Q factor measured at ambient conditions was Q=13980±20. By using the Q factor and the response of the tuning fork in resonance we can calibrate the movement of the tuning fork prongs out of the resonance, it is the DC calibration.

$$\frac{\Delta z}{V_{DC}} = \frac{1}{Q}\frac{A}{V_{exc}} \tag{B.4}$$

where, A is the amplitude for an excitation voltage V_{exc} (in resonance) and Δz is the displacement for an excitation V_{DC}. The DC calibration of the tuning fork was 2.79±0.07 Å/V.

Finally, by adding a tip of gold to a prong of the tuning fork and assembled it on the STM, we can calibrate the displacements of the tip due to the piezoelectric ceramics by comparation with the displacements of tuning fork. For that, we apply a sinusoidal wave to the tuning fork and we measure the adjustments in the tip position performed by the feedback in order to keep constant the tunneling current. In this way we have calibrated the movement of

the slider at ambient conditions. The calibration of the movements in *z* direction was 1.22±0.02 nm/V. Therefore, the displacement at the maximum voltage (140 V) is of the order of 100 nm.

C. Time-dependent potential in 1D

By a simple 1D model, it can be showed how a time-dependent perturbation induces an inelastic electron scattering. Our model shows the change in the energy of electrons due to vibrations in the potential. In a more realistic model, one must take into account the occupation of electronic states near the Fermi level, see for example [3].

Firstly, it is considered a Dirac delta potential situated in the origin of coordinates. The Schrödinger equation for this system is

$$\left(-\frac{\hbar^2}{2m^*}\partial_{x,x}+\lambda_0\delta(x)\right)\psi(x,t)=i\hbar\partial_t\psi(x,t) \tag{C.1}$$

As solution we propose,

$$\psi(x,t)=\begin{cases}(e^{ikx}+A_0e^{-ikx})e^{-i\omega t} & -\infty<x<0\\ B_0e^{ikx}e^{-i\omega t} & 0<x<\infty\end{cases} \tag{C.2}$$

where $\omega=\frac{\hbar k^2}{2m^*}+\frac{\lambda_0}{\hbar}\delta(x)$.

By imposing $\psi(x,t)$ continuous in $x=0$ we obtain

$$1+A_0=B_0 \tag{C.3}$$

Integrating the Schrödinger equation from $-\varepsilon$ to ε with $\varepsilon\to 0$,

$$-\frac{\hbar^2}{2m^*}\left(\partial_x\psi(x,t)\big|_{x=\varepsilon}-\partial_x\psi(x,t)\big|_{x=-\varepsilon}\right)+\lambda_0\psi(0,t)=0 \tag{C.4}$$

$$-\frac{\hbar^2 ik}{2m^*}(B_0-1+A_0)+\lambda_0B_0=0 \tag{C.5}$$

Using (C.3) and (C.5) we obtain the coefficients of the solution (C.2)

$$A_0=\frac{-\lambda_0^2-i\frac{\lambda_0\hbar^2k}{m^*}}{\left(\frac{\hbar^2k}{m^*}\right)^2+\lambda_0^2}\qquad B_0=\frac{\left(\frac{\hbar^2k}{m^*}\right)^2-i\frac{\lambda_0\hbar^2k}{m^*}}{\left(\frac{\hbar^2k}{m^*}\right)^2+\lambda_0^2} \tag{C.6}$$

With these coefficients we can calculate the transmission and reflexion probabilities as follows,

$$T = B_0^* B_0 = \frac{\left(\frac{\hbar^2 k}{m^*}\right)^4 + \left(\frac{\lambda_0 \hbar^2 k}{m^*}\right)^2}{\left(\left(\frac{\hbar^2 k}{m^*}\right)^2 + \lambda_0^2\right)^2} \qquad R = A_0^* A_0 = \frac{\lambda_0^4 + \left(\frac{\lambda_0 \hbar^2 k}{m^*}\right)^2}{\left(\left(\frac{\hbar^2 k}{m^*}\right)^2 + \lambda_0^2\right)^2} \tag{C.7}$$

It is easy to check that $T + R = 1$.

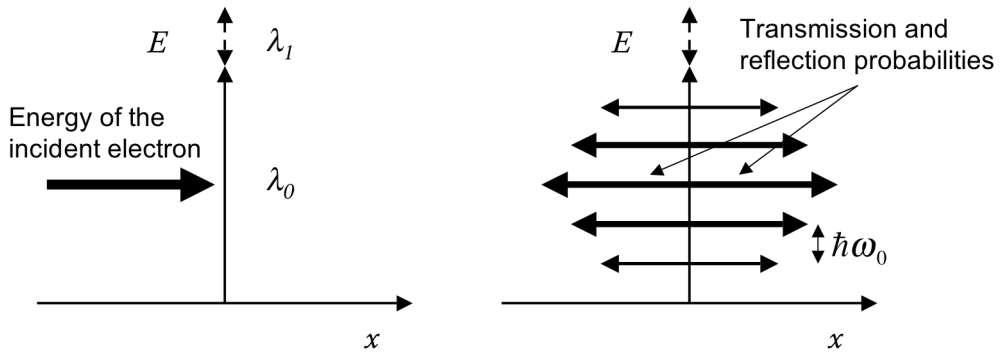

Figure C.1: An incident electron in a stationary Dirac delta potential with a small time-dependent perturbation will be transmitted and reflected. The transmitted and reflected energies differ from the incident one in a multiple of $\hbar\omega_0$.

It is considered now, that we introduce a small time-dependent perturbation. In this case, we have to solve the Schrödinger equation,

$$\left(-\frac{\hbar^2}{2m^*}\partial_{x,x} + \delta(x)(\lambda_0 + \lambda_1(e^{i\omega_0 t} + e^{-i\omega_0 t}))\right)\psi(x,t) = i\hbar\partial_t\psi(x,t) \tag{C.8}$$

where $\lambda_1 << \lambda_0$.

In order to solve this equation, we propose a solution in series:

Appendix

$$\psi(x,t)=\begin{cases}(e^{ikx}+\sum_{n=-\infty}^{\infty}A_n e^{-ikx}e^{-in\omega_0 t})e^{-i\omega t} & -\infty<x<0\\ \sum_{n=-\infty}^{\infty}B_n e^{ikx}e^{-in\omega_0 t}e^{-i\omega t} & 0<x<\infty\end{cases} \tag{C.9}$$

By imposing the continuity of $\psi(x,t)$ in $x=0$,

$$1+\sum_{n=-\infty}^{\infty}A_n e^{-in\omega_0 t}=\sum_{n=-\infty}^{\infty}B_n e^{-in\omega_0 t} \tag{C.10}$$

By integrating the Shrödinger equation from $-\varepsilon$ to ε with $\varepsilon\to 0$,

$$-\frac{\hbar^2}{2m^*}\left(\partial_x\psi(x,t)\big|_{x=\varepsilon}-\partial_x\psi(x,t)\big|_{x=-\varepsilon}\right)+\left(\lambda_0+\lambda_1(e^{i\omega_0 t}+e^{-i\omega_0 t})\right)\psi(0,t)=0 \tag{C.11}$$

$$-\frac{\hbar^2 ik}{2m^*}\left(\sum_{n=-\infty}^{\infty}B_n e^{-in\omega_0 t}-1+\sum_{n=-\infty}^{\infty}A_n e^{-in\omega_0 t}\right)+\lambda_0\sum_{n=-\infty}^{\infty}B_n e^{-in\omega_0 t}+$$

$$+\lambda_1\sum_{n=-\infty}^{\infty}B_n\left(e^{-i(n-1)\omega_0 t}+e^{-i(n+1)\omega_0 t}\right)=0 \tag{C.12}$$

In order to solve the equation (C.12) we have to take different orders of approximation in powers of λ_1. The solution at zero order in powers of λ_1 is the same as in the stationary problem (C.5),

$$-\frac{\hbar^2 ik}{2m^*}(B_0-1+A_0)+\lambda_0 B_0=0 \tag{C.13}$$

From the solution to first order in λ_1 we obtain,

$$-\frac{\hbar^2 ik}{2m^*}(B_{\pm1}+A_{\pm1})+\lambda_0 B_{\pm1}+\lambda_1 B_0=0 \tag{C.14}$$

$$B_{\pm1}=\frac{-\lambda_1 B_0\left(\lambda_0+i\frac{\hbar^2 k}{m^*}\right)}{\lambda_0^2+\left(\frac{\hbar^2 k}{m^*}\right)^2}=A_{\pm1} \tag{C.15}$$

It is not difficult to find the recurrence formula for higher orders,

$$B_{n+1}=\frac{-\lambda_1 B_n\left(\lambda_0+i\frac{\hbar^2 k}{m^*}\right)}{\lambda_0^2+\left(\frac{\hbar^2 k}{m^*}\right)^2}=A_{n+1} \tag{C.16}$$

From (C.16) it can be observed that if $\lambda_1 << \lambda_0$, then $A_0 >> A_{\pm 1} >> A_{\pm 2} >> \ldots$ and $B_0 >> B_{\pm 1} >> B_{\pm 2} >> \ldots$ as we have supposed solving (C.12).

We have obtained a solution in powers of λ_1, whose wavefunctions and eigenenergies are

$$\psi(x,t) = \begin{cases} e^{ikx}e^{-i\omega t} + A_0 e^{-ikx}e^{-i\omega t} + A_{+1}e^{-ikx}e^{-i(\omega+\omega_0)t} + A_{-1}e^{-ikx}e^{-i(\omega-\omega_0)t} + \ldots \\ B_0 e^{ikx}e^{-i\omega t} + B_{+1}e^{ikx}e^{-i(\omega+\omega_0)t} + B_{-1}e^{ikx}e^{-i(\omega-\omega_0)t} + \ldots \end{cases} \quad \text{(C.17)}$$

$$E = \hbar(\omega \pm \omega_0) + \ldots \quad \text{(C.18)}$$

The transmission and reflexion probabilities are given by,

$$T = B_0^* B_0 + 2B_1^* B_1 + \ldots \qquad R = A_0^* A_0 + 2B_1^* B_1 + \ldots \quad \text{(C.19)}$$

A time-dependent perturbation in the potential produces that an incident electron is transmitted and reflected with some probability that depends of the perturbation magnitude. The energy of transmitted or reflected electrons differs to the incident ones in a multiple of $\hbar\omega_0$, which is the energy of a phonon.

D. Probability Density Function (PDF)

A histogram is one of the most common graphical tools used to describe the frequencies of each value (or range of values) in a set of data, x_i, shown as adjacent rectangles. The height of a rectangle is equal to the frequency density of the interval, i.e. the frequency divided by the width of the interval. The total area of the histogram is equal to the number of data.

We have chosen the probability density function (*PDF*) instead of the conventional histogram. To obtain the *PDF* from a set of experimental data, x_i, we use the standard definition of the *PDF*,

$$PDF(x) = \frac{1}{N}\sum_{i=1}^{N}\delta(x - x_i) \quad \text{(D.1)}$$

where N is the number of data utilized.

We have approximated the Dirac delta function to a Lorentzian function as,

$$\delta(x - x_i) \approx -\frac{1}{\pi}\mathrm{Im}\left[\frac{1}{x - x_i + i\varepsilon}\right] = \frac{\varepsilon/\pi}{(x - x_i)^2 + \varepsilon^2} \quad \text{(D.2)}$$

where we have to chose a small ε.

Appendix

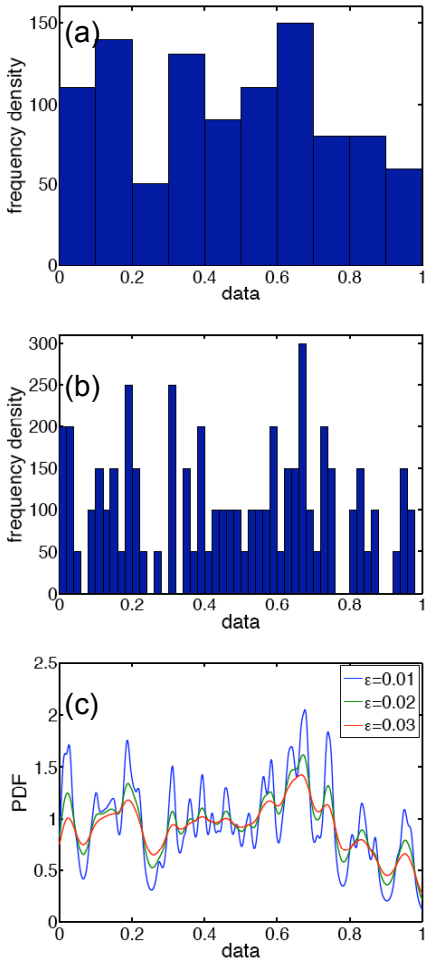

Figure D.1: Differences between the histogram and the PDF for a set of data x_i (100 random points) (a) histogram normalized by the bin width, 0.1 in this case. (b) histogram using a bin width equal to 0.02. (c) PDF using Δx=0.001 and different values of ε=0.01, 0.02 and 0.03.

In Fig. D.1 we show two histograms built by using two different bin width 0.1 and 0.02 and three *PDF* using different values of ε=0.01, 0.02 and 0.03. To build the PDF we have used a separation between x values of Δx=0.001. The main difference is that the *PDF* is a continous function, which can be compared at the

same scale for different values of ε. The advantage is that from the *PDF*, we can obtain the probability of finding a value in a certain range by the integration of the *PDF* in that range.

References

[1] T.N. Todorov, G.A.D. Briggs and A.P. Sutton, *"Elastic quantum transport through small structures"*, JOURNAL OF PHYSICS CONDENSED MATTER. 5 (1993) 2389-2389.
[2] A. Castellanos-Gomez, N. Agraït and G. Rubio-Bollinger, *"Carbon fibre tips for scanning probe microscopy based on quartz tuning fork force sensors"*, Nanotechnology. 21 145702.
[3] E.G. Emberly and G. Kirczenow, *"Electron standing-wave formation in atomic wires"*, Phys. Rev. B. 60 (1999) 6028-6033.

Summary

The on-going research focuses on the ultimate limits of miniaturization, when atoms and molecules are used as electronic components. The expectation of the research in nanophysics is that the miniaturization will lead to novel electronic devices based on quantum mechanics.

By using simple experimental techniques such us STM-BJ and MCBJ it is possible to gently break a metallic contact and thus investigate the electron transport properties of atomic-sized contacts. If such contacts are broken in a solution containing molecules terminated with anchoring groups, there is some probability that one molecule makes a bridge between the two electrodes forming a configuration called single molecule junction.

By means of the STM-BJ technique, we have investigated esentially to two systems: atomic gold wires and alkane-based molecular junctions wired to two gold electrodes. Due to the short length of these structures, the conductance is in the so-called full quantum regime, in which the wave functions of electrons are very sensitive to the local atomic arrangement.

In molecular solution at ambient conditions, we have investigated the differences in the conductance of alkane-based molecular junction by using two different anchoring groups thiols (-SH) and amines ($-NH_2$). Based on conductance histograms, we show results suggesting important differences during the junction formation. The alkanethiols produce higher conductance values than diamines and, they deform the appex of the electrodes while the junction is being stretched.

There is no realible method as of yet to connect a single molecule between two conducting electrodes, we cannot control the molecule lead coupling or the environment on the atomic scale. The extreme sensitivity of the conductance to the local atomic environment can be used to characterize the junctions. At low temperatures, the vibrational modes of an atomic-sized contact have zero occupation and may be excited by the electrons traversing the junction. In the limit of ballistic transport, the electrons travel through quantum channels across the junction without losing phase coherence or suffering inelastic scattering events. However, in our case a small fraction of electrons are able to exchange energy with vibrational modes or phonons localized in the narrowest part of the junction. The differences in transmission between atomic gold wires $T\sim1$ and molecular junctions $T\ll1$ produce a decrease or an increase respectively in the differential conductance at the phonon energy. Our results show that it is possible to characterize the atomic configuration of the junction by the inelastic

electron spectroscopy.

Resumen

La investigación en curso se centra en el límite último de la miniaturización, cuando átomos y moléculas son utilizados como componentes electrónicos. La expectación puesta en la investigación en nano física radica en que la miniaturización produzca nuevos dispositivos electrónicos basados en la mecánica cuántica.

Utilizando técnicas experimentales sencillas como el STM-BJ o MCBJ es posible romper lentamente un contacto metálico y así investigar las propiedades de transporte electrónico. Si dichos contactos son rotos en una disolución que contiene moléculas terminadas con grupos de anclaje, hay una cierta probabilidad de que una molécula forme un puente entre los dos electrodos formnando una configuración llamada unión de una sola molécula.

Por medio de la técnica STM-BJ, hemos investigado esencialmente dos sistemas: cadenas atómicas de oro y contactos moleculares de alcanos conectados entre dos electrodos de oro. Debido al la corta longitud de éstas estructuras, la conductance se encuentra en el llamado régimen cuántico, en el cual las funciones de onda de los electrones son muy sensibles a la configuración atómica.

En disolución molecular en condiciones ambiente, hemos investigado el efecto en la conductancia que producen dos grupos de anclaje tioles (-SH) y aminas ($-NH_2$). Por medio de histogramas de conductancia, mostramos resultados que sugieren importantes diferencias durante la formación de la unión molecular. Los alcanoditioles tienen una mayor conductancia que las alcanodiaminas y deforman los extremos de los electrodos mientras que la unión está siendo estirada.

No existe aún un método fiable para conectar dos electrodos conductores a una molécula, no podemos controlar el enlace ni tampoco el entorno a nivel atómico. La extrema sensibilidad de la conductancia al entorno atómico puede ser utilizada para caracterizar las uniones. A bajas temperaturas, los modos vibracionales de un contacto de tamaño atómico tienen ocupación cero y pueden ser excitados por medio de electrones atravesando la unión. En el límite de transporte balístico, los electrones viajan por la unión a través de canales cuánticos sin perder la coherencia de fase o sufrir ningún evento de dispersión inelástica. Sin embargo, en nuestro caso una pequeña fracción de electrones son capaces de intercambiar energía con modos vibrationales o fonones localizados

en la parte más estrecha del contacto. Las diferencias en transmisión entre cadenas atómicas de oro $T \sim 1$ y uniones moleculares $T \ll 1$ producen una reducción o aumento respectivamente en la conductancia diferencial a la energía del fonón. Nuestros resultados muestran que es posible caracterizar la configuración atomica de un contacto por medio de la espectrocopía de electrones inelásticos.

List of publications

1. *"Tetrathiafulvalene-based molecular nanowire"*
Francesco Giacalone, Mª Ángeles Herranz, Lucia Grüter, Mª Teresa González, Michel Calame, Christian Schönenberger, Carlos R. Arroyo, Gabino Rubio-Bollinger, Marisela Vélez, Nicolás Agraït and Nazario Martín.
Chem. Commun. (2007), 4854

2. *"Study of electron-phonon interactions in a single molecule covalently connected to two electrodes"*
Joshua Hihath, Carlos R. Arroyo, Gabino Rubio-Bollinger, Nongjian Tao and Nicolás Agraït.
NanoLett. 2008 8(6); 1673-1678

3. *"Tunning vibrations in single-molecule junctions: inelastic electron tunneling spectroscopy of an alkanedithiol"*
Carlos R. Arroyo, Thomas Frederiksen, Gabino Rubio-Bollinger, Marisela Vélez, Andrés Arnau, Daniel Sánchez-Portal and Nicolás Agraït.
Phys. Rev. B **81**, 075405 (2010)

4. *"Statistical study of alkane-bridged junctions in molecular solution"*
Carlos R. Arroyo, Marisela Vélez, Gabino Rubio-Bollinger and Nicolás Agraït.
(In preparation).

5. *"Mechanical properties and dynamics of atomic chains: measuring the interatomic interactions"*
Carlos R. Arroyo, Juan José Riquelme, José Gabriel Rodrigo, Gabino Rubio-Bollinger and Nicolás Agraït.
(In preparation).

6. *"Piezo electric positioning standard based on quartz tuning forks"*
Andres Castellanos-Gomez, Carlos R. Arroyo, Nicolás Agraït, and Gabino Rubio-Bollinger.
(In preparation).